Structure and dynamics of model lipid membranes

The influence of amyloid-β peptide fragments on model membranes

D I S S E R T A T I O N

zur Erlangung des akademischen Grades

Dr. rer. nat.
im Fach Physik

eingereicht an der
Mathematisch-Naturwissenschaftlichen Fakultät
Humboldt-Universität zu Berlin

von
Herr Matthew Barrett B.Sc., M.Sc.

Präsident der Humboldt-Universität zu Berlin:
Prof. Dr. Jan-Hendrik Olbertz

Dekan der Mathematisch-Naturwissenschaftlichen Fakultät:
Prof. Dr. Elmar Kulke

Gutachter:
1. Prof. Dr. Matthias Ballauff
2. Prof. Dr. Judith Peters
3. Prof. Dr. Rheinhard Lipowsky

eingereicht am: 19. November 2015
Tag der mündlichen Prüfung: 18. April 2016

Abstract

Proper brain function involves many processes carried out in or at membranes. The many cells and organelles in the brain are responsible for processes such as adenosine triphosphate (ATP) production, protein cleavage, transfer of electric signals along neurons (brain cells) and membrane vesicle formation, which are all either facilitated by lipid membranes or involve lipid membranes directly. In diseases affecting the brain such as Alzheimer's disease, symptoms may arise from perturbations in the normal functioning of some of these processes. The peptide amyloid-β has long been associated with the disease, however the link between the peptide and the origin of symptoms is poorly understood. An emerging hypothesis is that monomeric and oligomeric forms of the peptide interact with neuronal membranes, resulting in perturbations in the bilayer structure and in the dynamic processes which take place in the bilayer.

Using X-ray and neutron scattering techniques, the structure and dynamics of model lipid membranes and the changes which arise in the presence of amyloid-β peptide fragments have been studied. Monomers of the peptide fragment amyloid-β_{22-40} were found to intercalate into an anionic lipid bilayer. Through quasi-elastic neutron scattering, dynamics of bilayer lipids were observed. The presence of 1.5 mol% of the peptide results in a decrease in the diffusion coefficients for lipid centre of mass motion on the nanosecond time-scale, as well as lipid tail dynamics on the picosecond scale at 30°C. On the other hand, in the gel-phase of the lipid, at 15°C, an increase in the diffusion coefficients for both of these processes was observed.

A series of samples with various cholesterol content and either the amyloid-β_{22-40} peptide fragment or the amyloid-β_{1-42} full length peptide was characterized using X-ray diffraction. Structural details, including the peptide position, were modelled and compared to electron density plots obtained from the diffraction experiments. The amyloid-β_{22-40} peptide was found to populate two positions, on the surface and embedded in the bilayer. The amyloid-β_{1-42} peptide embeds itself into the membrane, is modelled by a single population for high cholesterol levels (40 mol% cholesterol).

The design and commissioning of the BerILL humidity chamber, a sample environment with precise temperature and humidity control compatible with neutron scattering experiments is presented. The project goal of achieving high and stable humidity was achieved, the presented humidity chamber allows for precise control of temperature and humidity up to 99.9% relative humidity. Temperature and humidity control are essential for experiments with biological samples, and can be easily and reliably controlled with the chamber. The BerILL humidity chamber allows for increased efficiency during neutron experiments and can replicate physiological conditions experimentally.

Zusammenfassung

Die Funktion des Gehirns hängt von vielen Prozessen ab, die an Membranen ausgeführt werden. Dabei sind diverse Zellen und Organellen für verschiedene Prozesse verantwortlich, wie z. B. die Herstellung von Adenosintriphosphat, Proteinspaltung, Signaltransfer an Neuronen und Vesikelbildung. Die Lipidmembrane ermöglichen und beeinflussen diese Prozesse über ihre Struktur. Krankheitssymptome, wie z. B. die der Alzheimer'schen Demenz, können durch eine Störung der normalen Prozesse hervorgerufen werden. Das Peptid Amyloid-β wird seit vielen Jahren mit der Alzheimer'schen Demenz in Verbindung gebracht, aber die Verbindung zwischen dem Peptid und der Herkunft der Symptome bleibt unklar. Eine neue Hypothese besagt, dass Wechselwirkungen von Mono- oder Oligomeren des Amyloid-β mit neuronalen Zellmembranen zu Veränderungen der Membran-Doppelschichtsruktur führen und Störungen dynamischer Prozesse in den Membranen verursachen können.

Mit Methoden der Röntgen- und Neutronenstreuung wurden die Struktur und Dynamik von Modellmembranen und Änderungen durch den Einfluss des Peptids Amyloid-β auf die Modellmembranen untersucht. Es konnte gezeigt werden, dass Monomere des Peptidfragments Amyloid-β_{22-40} in anionische Lipidmembranen eingebaut werden. Mittels quasielastischer-inkohärenter Neutronenstreuung wurde die Dynamik von Lipidmembran untersucht. Ein Anteil von 1,5 mol% Amyloid-β_{22-40} in einer Lipidmembran bei 30°C verursacht eine Verringerung der Diffusionskoeffizienten sowohl der Schwerpunktbewegung der Lipide im ns-Bereich als auch der Dynamik der Fettsäurereste im ps-Bereich. Andererseits wird in der Gelphase der Lipidmembran bei 15°C ein Anstieg der Diffusionskoeffizienten beider Prozesse beobachtet.

Eine Serie von Lipidproben mit unterschiedlichem Cholesteringehalt und eingelagerten Peptiden Amyloid-β_{1-42} und Amyloid-β_{22-40} wurde Mittels Röntgendiffraktion charakterisiert. Strukturdetails einschließlich der Lage der Peptide wurden modelliert und mit den experimentellen Elektronendichteprofilen verglichen. Für das Peptid Amyloid-β_{22-40} wurden zwei Positionen gefunden, eine auf der Oberfläche der Membran, eine zweite in der Membran eingelagert. Das Peptid Amyloid-β_{1-42} ist teilweise in die Membran eingelagert und ist in einer 40 mol% Cholesteringehaltige Membrane durch eine einzelne Position modelliert.

Der Entwurf und die Inbetriebnahme der BerILL Feuchtekammer wird beschrieben. Unser Entwicklungsziel, stabile und hohe relative Feuchte zu produzieren, wurde erreicht. Die vorgestellte Feuchtekammer erlaubt die präzise Kontrolle von Temperatur und Luftfeuchtigkeit bis zu 99.9 % relativer Feuchte. Die Parameter Temperatur und Feuchte sind essentiell für Experimente mit biologischen Proben und durch die BerILL Feuchtekammer wird die Effektivität von Neutronenstreuexperimenten erhöht und Experimente unter physiologischen Bedingungen ermöglicht.

Contents

1 Introduction

1.1 Motivation

The lipid membrane is one of the most important structures in biology. The membrane structure facilitates the compartmentalization of cells and organelles, creating barriers between aqueous compartments and their surroundings. Without these barriers, complex life would not be possible. Early models of the lipid membrane describe it as a passive medium which acts as a host to the more important biological entities such as protein complexes [1], but more recently the focus has shifted towards understanding the membrane to reveal biological function [2]. The composition of a membrane is closely linked to the membrane's properties and its functionality [3]. Changes in membrane composition, and the interactions of peptides or proteins with membrane lipids are known to modify these properties, and may lead to detrimental side-effects [4].

The proper functioning of a complex organ like the brain involves many processes carried out at membranes. Processes such as adenosine triphosphate (ATP) production, protein cleavage, transfer of electric signals along neurons (brain cells) and membrane vesicle formation, which are all either facilitated by lipid membranes or involve lipid membranes directly [5]. In particular, in diseases affecting the brain such as Alzheimer's disease, symptoms may arise from perturbations in the normal functioning of some of these processes [6, 7, 8, 9, 10, 11, 12, 13].

Alzheimer's disease has been studied for over 100 years, with the first reported link between the symptoms of dementia and brain physiology in 1907 [14]. The initial hypothesis was that symptoms of the disease were related to overproduction of certain proteins, leading to proteinous plaques in the extracellular regions of the brain [15]. Although this hypothesis has been studied for many years, no clear explanation of the origin of the symptoms exists. A new hypothesis has been proposed, connecting the symptoms to perturbations in the lipid membrane caused by membrane intercalated monomers of the amyloid-β peptide [16, 17, 18, 19, 20].

Changes in the interactions of peptides or proteins with a membrane are often associated with diseases. Although the exact mechanism of action of Aβ toxicity remains obscure [21], there is strong evidence that Aβ peptides can penetrate membranes [22, 23], leading to permeabilization [24] and to pore formation [25]. Changes in the complex bilayer structure or dynamics may affect the rate and feasibility of essential processes carried out in the cell membrane [6].

In particular, membrane dynamics are of special importance when considering the efficiency of the secretases responsible for cleavage of the amyloid-β precursor APP

(amyloid precursor protein). A perturbation of the lipid diffusion rate can lead to a change in the behaviour of the β and γ secretases, causing an autocatalytic increase in the formation of neurotoxic amyloid-β species, further stimulating toxic peptide production [7, 18, 8]. Neuronal cells, especially their synapses, are rich in mitochondria which produce ATP for the energy demanding synthesis and release of transmitter molecules involved in cognitive functions. Thus, amyloid-β induced changes in lipid dynamics of mitochondria can lead to decreased ATP production and eventually cell death [9, 10]. Furthermore, at the synapses, essential fusion and vesicle formation processes will be affected by changes in lipid dynamics, leading to complications in signal transduction [11, 12, 13, 26]. Therefore, a clear picture of the membrane dynamics and the changes which occur in the presence of the neurotoxic peptides is essential to understand this complex disease.

Model lipid membranes can be used to create a system which is simple enough to describe quantitatively and yet realistic enough to extract meaningful parameters and gain insight. The goal is to produce quantitative data which will then shed light onto complex biological structure or processes. The model systems used are typically studied in controlled temperature and humidity environments which can replicate physiological conditions.

The dynamics of membrane lipids over various length and time-scales can be explored with a variety of techniques. Molecular dynamics (MD) simulations shed light on the motions of lipids in the fs to ns time-range. MD simulations predict long-range diffusion with relaxation times slower than a nanosecond, sub-diffusive (restricted) dynamics in the picosecond range, and ballistic dynamics occurring in the sub-picosecond range [27, 28]. The observation of lipid dynamics over a large time-range is experimentally accessible through the use of quasi-elastic neutron scattering. By tuning the experimental parameters (instrumental resolution) of a QENS spectrometer, a specific time-range can be observed, allowing one to isolate and analyze motions of interest [29]. In particular, nanosecond dynamics can be measured by high energy resolution backscattering spectrometers [30, 31, 32, 33], while faster picosecond dynamics can be observed with low energy resolution time-of-flight spectrometers [34, 35, 36, 37]. The nanosecond dynamics can be compared to other techniques such as fluorescence [38, 39, 40] or NMR (nuclear magnetic resonance) [41, 42]. Recent quasi-elastic neutron scattering experiments from Busch *et al.* and Sharma *et al.* have shown that small molar amounts of membrane present molecules such as cholesterol [43] or melittin [33] can have a considerable effect on membrane lipid dynamics, which sets the stage for dynamic measurements with amyloid-β peptides.

In a recent review by Yang *et al.* [18], the effect of Aβ peptide fragments and other molecules (such as cholesterol) on the diffusion rate of lipids in the membrane is presented. Amyloid-β peptide fragments perturb the structure of the bilayer [23] and can change the picosecond lipid dynamics, as recently demonstrated by our group [44, 45]. In particular, the first measurements by Buchsteiner *et al.* showed the effect of the short, primarily hydrophobic, $A\beta_{25-35}$ peptide on the picosecond dynamics of a lipid bilayer, indicating decreased translational lipid dynamics with peptide presence in

the gel and fluid phases [44]. Further investigations compared the effect of $A\beta_{25-35}$ and $A\beta_{22-40}$, the latter being a peptide fragment with a length and hydrophobicity similar to that of a DMPC (1,2- dimyristoyl- *sn*- glycero- 3-phosphocholine) lipid molecule, at 47°C. A slowing of local lipid dynamics was observed in the presence of both peptides well into the fluid phase [45].

To better understand the effect of peptides in the lipid bilayer, experiments on different peptide fragments in increasingly complex systems are necessary. In this thesis, the structural and dynamic changes to a lipid bilayer exposed to the $A\beta_{22-40}$ and $A\beta_{1-42}$ peptides were explored in an anionic lipid bilayer, as well as a cholesterol rich lipid bilayer. These experiments shed light on the complex interaction between lipids and proteins, as well as push forward the understanding of the molecular processes behind Alzheimer's disease. The development and commissioning of a new humidity chamber which can be used for future biophysics experiments is also presented.

1.2 Biological membranes

Many different cell types are present in complex organisms. Each cell has specific set of physiological characteristics which allow it to perform the essential tasks vital to the survival of the organism. The compartmentalization, not only of individual cells, but also the organelles which the cells contain, is achieved using membranes. These membranes consist of a variety of biological molecules including lipids, proteins, sterols and sugars. The composition of a biological membrane varies drastically depending on the particular cell or organelle and the function it must perform. Membranes are permeable to certain ions and molecules, allowing passive diffusion through osmosis to control the cell's contents. Other ions and molecules must be actively transported through membranes using protein complexes, building gradients across the membrane [3, 4, 5].

1.2.1 Lipids

For the majority of cells, the membrane is composed of primarily lipids. Eukaryotes in particular spend enormous amounts of resources synthesizing thousands of different types of lipids. In fact, approximately 5% of the genetic information in eukaryotes is used for creating and maintaining lipids [46]. Generally, lipids are small hydrophobic or amphiphilic (containing hydrophobic and hydrophilic parts) molecules which self-assemble into a variety of conformations depending on the solvent in which they exist. With water as the main solvent in the vast majority of biological systems, lipids tend to group into structures to shield the hydrophobic parts from the surrounding water, as is seen in Figure 1.1. Depending on the type of lipid, and the concentration of this lipid in the solvent, structures such as micelles, liposomes or bilayers can form. In most biological systems a two molecule thick bilayer with a hydrophobic core is common, with the hydrophobic tails of the lipid together in the centre. The human body is composed of approximately 10^{13} cells [47], typically compartmentalized by a

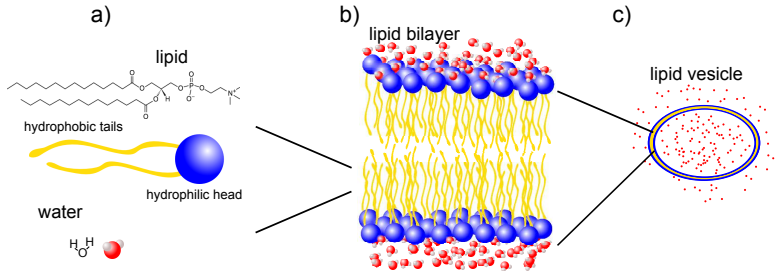

Figure 1.1: a) A DMPC lipid molecule chemical structure and simplification to a generic phospholipid with its hydrophilic head-group (blue) and two hydrophobic tails (yellow) and a water molecule chemical structure and cartoon (red). b) When exposed to water, many phosopholipids self-assemble into a bilayer formation, to decrease contact between the hydrophobic and hydrophilic components. c) Depending on the properties of a single lipid, higher structures such as vesicles (shown as a slice-through) may form. DMPC chemical structures from Avanti Polar Lipids [48].

two molecule thick bilayer. These thin features extend to cover a vast surface area, approximately 100 km^2 for humans [2].

In 1972, the fluid mosaic model presented by Singer and Nicholson first described the bilayer as a two-dimensional liquid with proteins freely floating within [1]. This model has since been improved and modified. In the past 40 years, the role of the bilayer has shifted from a passive environment in which biological processes occur to an important part of cell function [49].

In biological membranes, various types of lipids are present, including glycerolipids, sphyngolipids, phospholipids and sterols [50, 51]. Glycerolipids contain a mono-, di- or tri-substituted glycerol and function as energy storage in the fat molecules of animal tissues. They are found in membranes and in concentrations up to 8 mass% [52]. Sphingolipids contain an amino alcohol called sphingosine with a hydrophobic chain consisting of 16 to 26 carbons and are found primarily in the liver and in red blood cells in concentrations of up to 19 mass% [53]. Phospholipids make up to 40 mass% of the membrane in mammalian cells [54]. Phosphate (PO_4) groups are found in the hydrophilic head-group of the phospholipid, giving the molecule its name. Phospholipids, due to their high membrane concentration, have a large influence on the membrane's structure and behaviour [4, 55]. Sterols also make up a large percentage of membranes, and are characterized by their four-ring core structure [56]. Cholesterol in particular is found in the membranes of eukaryotic cells, and will be discussed in more detail in Section 1.4.1.

A phospholipid can be further categorized by describing the features of the hydrophilic head-group and hydrophobic tails. These classifications are based on the charge of the head-group and the length and degree of unsaturated carbons in the tails. Some common lipid head-groups include the phosphatidylserine (PS) head, with negative charge, and the zwitterionic (containing two counteracting charges)

phosphatidylcholine (PC) and phosphatidylethanolamine (PE). The acyl-chains of the phospholipid tails typically range from 12 to 24 carbons, and may contain from 0 (fully saturated) to 6 (polyunsaturated) carbon-carbon double bonds. These tails are described with the m:n format, with m representing the number of carbons in a chain, and n representing the number of double bonds. In the remainder of this document, the phospholipids will be referred to using the general term lipids. Table 1.1 lists a selection of lipids which are commonly used in biophysical experiments. The bold entries have been used for experiments in this thesis.

Properties of commonly used lipids					
Name	Abbrev.	Components	Chain length	M_w (g/mol)	Transition temp. (K)
1,2-dimyristoyl-sn-glycero -3-phospho-L-serine	**DMPS**	$C_{35}H_{65}NO_{10}PNa$	14:0	701.844	308
1,2-dipalmitoyl-sn-glycero -3-phosphocholine	DPPC	$C_{40}H_{80}NO_8P$	16:0	734.039	314
1,2-distearoyl-sn-glycero -3-phosphocholine	DSPC	$C_{44}H_{88}NO_8P$	18:0	790.039	328
1,2-dioleoyl-sn-glycero -3-phosphoethanolamine	DOPE	$C_{41}H_{78}NO_8P$	18:1	744.034	283
1,2-dioleoyl-sn-glycero -3-phospho-L-serine	DOPS	$C_{42}H_{77}NO_{10}PNa$	18:1	810.025	262
1,2-dimyristoyl-sn-glycero -3-phosphocholine	**DMPC**	$C_{36}H_{72}NO_8P$	14:0	677.933	297
1,2-dioleoyl-sn-glycero -3-phosphocholine	**DOPC**	$C_{44}H_{84}NO_8P$	18:1	786.113	253
1-palmitoyl-2-oleoyl-sn -glycero-3-phosphocholine	POPC	$C_{42}H_{82}NO_8P$	16:0-18:1 *	760.076	271
1-palmitoyl-2-oleoyl-sn -glycero-3-phospho-L-serine	POPS	$C_{40}H_{75}NO_{10}PNa$	16:0-18:1 *	783.988	287

Table 1.1: Commonly used phospholipids. Chain length given in (m:n) format, where m is the number of carbon atoms in a single tail, and n the number of double bonds present. Main phase transition temperature (gel to fluid) is cited for a single component membrane at full hydration [57]. Bold entries were used in experiments discussed in the thesis. Entries marked with * possess two differently structured tails.

Biophysical experiments rely on simplification to characterize and understand complex systems from the ground up. In the case of the complex biological membrane, the number of components is reduced until precise and reproducible systems can be produced and studied. Model membranes consisting primarily of lipids and small amounts of other relevant molecules can be artificially created in the lab with relative ease and good reproducibility. Lipid molecules self-assemble into two dimensional

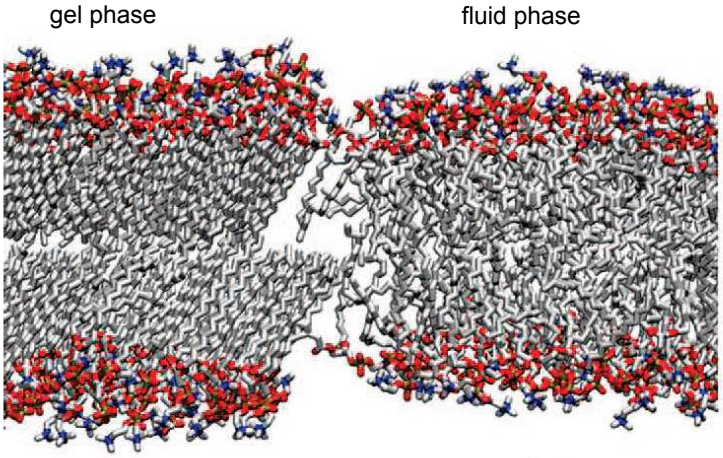

Figure 1.2: The gel (left) and fluid (right) phases of a DPPC lipid bilayer created in a molecular dynamics simulation. From Sane *et al.* 2009 [60]. Notice the difference in thickness and of chain features between the *gel* and *fluid* phases.

bilayers, representing the backbone of the complex cell-membrane. Lipid bilayers are capable of hosting many other biologically relevant molecules as well. The lipid membrane forms a periodic, quasi-crystal structure, which lends itself to scattering experiments using small wavelength probes like X-rays or neutrons.

1.3 Phase behaviour of lipid membranes

For a single component membrane, such as DMPC, the bilayer exists primarially in two different, structurally distinct phases: the gel (L_β) phase and the fluid (L_α) phase [58], although other phases (ripple phases) exist in certain conditions. By tuning the temperature or humidity of the sample these phases can be accessed. The dynamics of the lipid molecules are drastically different for different phases. For example, the lateral diffusion constant of a lipid in a pure DMPC bilayer in the gel phase are up to two orders of magnitude slower than the same lipid in fluid phase, when measured by fluorescence recovery after photobleaching [59]. A lipid in the gel-phase is closely packed together with its neighbours, and as a result, the acyl chain tails extend to the all trans conformation.

The phase accessed depends on the strength of the interaction between the lipid molecules. The two phases are significantly different in physical properties. Figure 1.2 shows a simulated DPPC lipid bilayer in the gel and fluid phase.

The L_β or *gel* phase is characterized by fully extended acyl tails in the trans-orientation. This results in rigidity and a long z-axis. This rigidity and lengthening allows for a tight packing of the lipid head-groups and a low area per molecule [61].

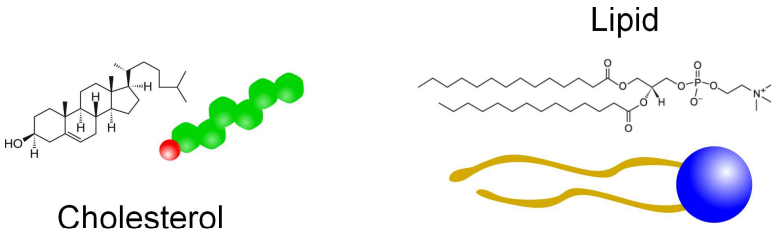

Figure 1.3: A chemical structure of cholesterol and a cartoon simplification (left) and the DMPC chemical structure and simplification (right). Cholesterol and DMPC chemical structures from Avanti Polar Lipids [48].

In the L_α or *fluid* phase individual lipid molecules undergo more thermal motions than in the gel phase. The lipid head-groups are more loosely packed, and thus have a larger area per molecule. The packing of the tails is not as efficient, due to the presence of gauche "kinks" in the C-C bonds [61].

DMPC and DMPS lipids

In the experiments presented in the following chapters, model lipid membranes have been constructed using primarily the zwitterionic saturated 14 carbon chain lipid DMPC and a small amount of DMPS, a lipid with negative charge on the head group and identical carbon chains to DMPC.

DMPC is one of the most well understood of the phospholipids [30, 62, 63, 64, 65, 66, 67, 68, 69]. The structure and dynamics of DMPC membranes have been explored in a variety of environments (temperature, relative humidity, pH, salt concentration and pressure). DMPC undergoes its main phase transition (from gel to fluid phase) at ~24 °C, allowing both gel and fluid measurements to be accessed with relative ease in a laboratory setting. As the majority of physiological lipid membranes possess some charge, DMPS was also essential to create accurate model membranes, and to facilitate interaction with protein [70].

1.4 Non-lipid membrane constituents

1.4.1 Cholesterol

Cholesterol (shown in Figure 1.3) also falls into the classification of lipid, but will be discussed separately here due to its unique role in biological membranes. Cholesterol is an essential component in animal membranes, allowing for the fluidity and flexibility of the membrane to be precisely controlled [71]. Cholesterol contains a hydroxyl group, which exhibits polar (hydrophilic) properties. The hydroxyl group is connected to a bulky and rigid steroid and hydrocarbon chain, which exhibit hydrophobicity. The large "body" (green section in Figure 1.3) and small "head" (red section in Figure 1.3), when in a lipid bilayer, hinder the motions of the lipid acyl-chains, allowing for tighter

packing. Eukaryotic cells can regulate the cholesterol content of cell membranes to produce a range of functionality in the cells.

Cholesterol may also be a key component in the formation and functionality of lipid rafts, although the presence of lipid rafts remains controversial [72]. Lipid rafts are non-equilibrium, dense regions which form in the bilayer. For a short time, lipid rafts provide a rigid structure which is necessary to host signalling or receptor proteins. The stability provided by the high cholesterol concentration in this micro-environment is necessary for protein complexes to assemble and function, and provides protection from unrelated enzymes.

1.4.2 Protein

Proteins are also present in biological membranes in high concentrations. Membrane proteins play a variety of roles in transport: moving molecules and ions across the membrane, capturing and releasing signal molecules and allowing a cell to interact with neighbouring cells. A protein can be classified as a bio-polymer, due to the many amino acids which are linked together to form the larger molecule. The structure of a protein is closely linked with its functionality. The primary structure of the protein is simply a chain of amino acids. The amino acids interact with each other with hydrogen bonding to form the secondary structure, containing alpha-helicies, beta-sheets and turns. The secondary structure then influences the tertiary structure or "folding" of the protein. This folding is a result of a minimization of the exposure of the hydrophobic amino acids to the surrounding water while simultaneously attempting to maximize favourable amino acid interactions [2]. The folded state of the protein is directly related to the protein's function. A protein's folded geometry is stabilized by relatively weak electrostatic forces, hydrogen bonds and sulfur bridges, and is therefore very sensitive to the solvent in which the protein exists. A change in temperature, pH or salt-content could result in a loss of this tertiary structure, so-called denaturing [73].

The majority of proteins exist as globule proteins, freely floating in an organism. However, proteins which exhibit a hydrophobicity profile similar to a lipid bilayer may also come in contact with or intercalate into the bilayer in order to reduce free energy, either temporarily (peripheral membrane proteins) or permanently (integral membrane proteins). These membrane proteins are estimated to make up >25% of proteins in a given cell or organism [74]. Membrane proteins play an important role in the biological processes involving the lipid bilayer, such as signalling, membrane fusion and active transport of nutrients and ions. Two classes of the integral membrane protein exist, monotopic or transmembrane. The integral monotopic proteins do not span the entire length of the bilayer, instead they may penetrate partially through a hydrophobic component, lay on the surface of the bilayer with an α-helix, exhibit an electrostatic interaction with the help of external ions, or a combination of these. Integral transmembrane proteins may pass one or more times through the lipid bilayer with α-helicies or β-barrels.

Amyloid-β peptide

A protein with fewer than 50 amino acids is often referred to as a peptide. One peptide of particular interest is the amyloid-β peptide. The understanding of amyloid-β (Aβ) and its effect on the neurons of the human brain have been of interest since the initial observations made by Alois Alzheimer in the early 1900s. Alzheimer first reported the presence of protenious plaques in the post-mortem brains of patients experiencing symptoms of dimentia towards the end of their lives in 1907 [14]. In the century that followed, much effort has been put towards a better understanding of the link between amyloid-β and symptoms of Alzheimer's disease, yet as it stands, no consistent explanation of the origin of the disease's symptoms exists [75].

Amyloid-β is produced through the cleavage of the long (770 amino acid) integral membrane protein Amyloid Precursor Protein (APP). APP is expressed in many mammalian cells, but highly concentrated in the synapses of neuronal membranes. The APP is cleaved in the bilayer by γ- and β-secretases, resulting in the 37-49 amino-acid long amyloid-β peptide. The most common cleavage product is 40 to 42 amino acids in length, referred to by the number of amino acids present (i.e. $A\beta_{1-40}$ and $A\beta_{1-42}$), and consisting of hydrophobic and hydrophilic components. After cleavage, the resulting monomeric Aβ peptides may exit the bilayer and proceed to form oligomeric "seeds" which recruit more monomers and eventually lead to plaques. Focus has been put on dissolving or reducing the number of plaques formed, however fewer plaques does not lead to in a decrease of symptoms [76].

If the Aβ peptides do not leave the lipid bilayer after cleavage, the presence of monomeric peptides may influence the structure and dynamics and thus the functionality of the biological membrane [22, 23, 44, 45, 70, 77].

1.5 Literature review

It is well known that the structure of the model membrane and the time rate associated with dynamics can change substantially from lipid to lipid, and is closely related to the temperature and humidity of the surroundings. The addition of other components to the bilayer, such as cholesterol or protein also affects the structure and the motion of lipids in the bilayer [59].

One can experimentally access the gel and fluid phases of a lipid bilayer by controlling temperature and hydration of the sample. Raising the heat of a membrane sample causes more fluctuations in the tails, breaking up the closely packed orientation. A similar effect can be achieved through hydration. A bilayer with low hydration does not experience the same freedom of movement as a fully hydrated bilayer. Above 98% relative humidity, a substantial swelling of the d-spacing, the total bilayer repeat distance, occurs [63, 64, 78]. The additional water molecules near the hydrophilic side of the lipid bilayer allow for fluctuations not possible in the dehydrated analogue, and as a result dynamics are changed [66]. Since a fully hydrated bilayer in the fluid phase is the most biologically relevant phase, many experimentalists strive to recreate this condition

in membrane biophysics experiments. The challenges and strategies to achieve this will be discussed in detail in Chapter 5.

The characteristics of the lipid molecules also play a significant role in the macroscopic properties of the bilayer. The gel to fluid phase transition temperature increases as the number of carbon atoms in the acyl-chain increases. The degree of unsaturation (number of C-C double bonds in the tails) will also have a significant effect on the bilayer phase transition temperature, each additional double bond significantly decreasing the transition temperature [79].

As was previously mentioned, the addition of other molecules into the bilayer may also significantly alter the dynamics of the system. Cholesterol, for example, is a necessary component of animal cells, and is used to regulate the rigidity of the bilayer. With the addition of cholesterol, the phase behaviour becomes more complex, and the liquid ordered (Lo) phase manifests above ∼25% cholesterol (in DPPC) [80]. Many of the membranes in animal cells and organelles contain large ratios of cholesterol, up to 50% for mammal plasma membranes [46]. The presence of cholesterol at low concentrations in the gel-phase of a lipid bilayer generally causes a decrease in order, increasing the lateral diffusion rate. In the fluid phase, however, the opposite is true. The addition of a small amount of cholesterol results in a slowing of the lateral diffusion [59].

In general, the addition of even small amounts of other membrane components into a bilayer can cause significant changes in both the long-range and internal dynamics of bilayer lipids as observed by fluorescence techniques and NMR [59] and by neutron scattering [81]. The dynamics over these time-scales often determines or strongly affects the biological functions, such as diffusion through a membrane, or integral membrane protein behaviour [82].

1.5.1 Structure of model membranes perturbed by amyloid peptides

The structural parameters which characterize model membranes have been studied successfully through diffraction techniques, notably X-ray and neutron diffraction (see Section 2.2 for a detailed discussion of the experimental approach to such measurements). Fourier reconstruction of either the electron or neutron density profiles allows one to determine the organization of molecules across the lipid bilayer with Ångström resolution. Other details can also be determined by scanning in-plane (i.e. lipid hydrocarbon chain nearest neighbour distances). For a lipid bilayer consisting of saturated lipid molecules, a typical bilayer density profile is shown in Figure 1.4. The addition of small amounts of other molecules would change the electron/neutron density at a particular part of the bilayer, giving a hint to the location. Additional molecules may also disrupt the bilayer organization or change the lamellar repeat spacing.

In 1996, Mason *et al.* used X-ray diffraction to determine the location of the peptide fragment amyloid-β_{25-35} a fluid phase lipid bilayer [84]. For a peptide introduced to a bilayer hydrated with distilled water, the peptide resided only on the hydrophilic surface of the POPC bilayer, however introducing a NaCl buffer resulted in a portion of the peptides intercalating into the bilayer centre. This was observed with large amounts of peptide (>10 mol%).

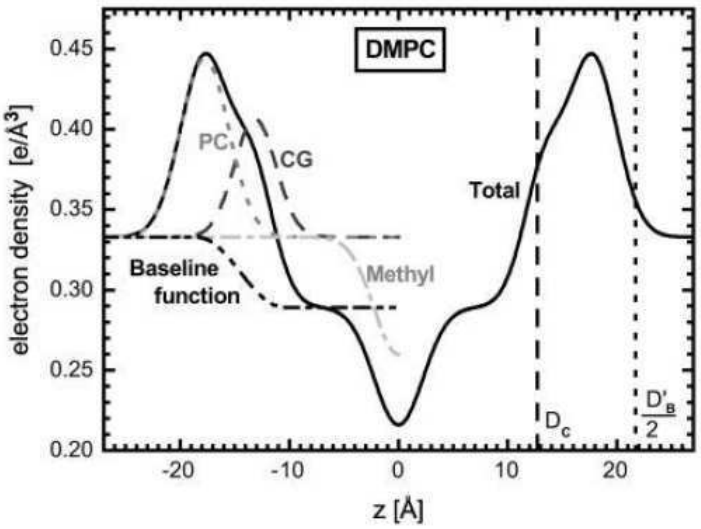

Figure 1.4: Reconstructed electron density profile of a DMPC lipid bilayer. The profile phosphatidylcholine (PC) group, the carbonyl-glycerol (CG) group and the methyl groups are shown with their respective contributions as dashed lines (left) and summed to create the total reconstruction (right). From Kučerka *et al.*, 2005 [83].

The next measurement on the sub-nanometre organization of the lipid bilayer was published in 2002 by Dante *et al.* [22]. In this paper, the group used deuterium labelling of the Leucine residue to determine the peptide location in the bilayer. Two types of bilayers were prepared, the zwitterionic POPC, and an anionic bilayer containing POPS, having negatively charged headgroups, which replaces the need to use the NaCl buffer solution. The pure POPC bilayer hosted two populations of the peptide, but the signal from the intercalated portion was very weak, corresponding to approximately 1/8 of the peptide residing in the bilayer, and 7/8 on the surface. A slightly anionic bilayer showed about a 1:1 distribution of the peptide.

This experiment was replicated by the same group in 2003 [70], but with a different preparation protocol. The peptide was externally applied to the system after the bilayers had already formed. Both techniques resulted in identical peptide placement. Again, the bilayer was constructed with some negatively charged lipids, resulting in an anionic bilayer.

Further experiments involving the full-length amyloid-β_{1-42} peptide have also been carried out by the group. Unilamellar vesicles have been prepared and observed using small-angle neutron scattering [23], and by neutron reflectivity and atomic-force microscopy [85]. This peptide causes a bilayer thinning of and a softening as probed by the atomic force microscope.

Recently, Dies *et al.* have performed an X-ray experiment with an anionic bilayer and

the addition of either amyloid-β_{25-35} or amyloid-β_{1-42} [86]. Both peptides reside in two populations in the bilayer. The higher resolution inherent to X-ray measurements allowed for more structural details, including the orientation of the peptide (not just the location) to be determined. The amyloid-β_{25-35} is best modelled as slightly tilted from its axis, whereas the amyloid-β_{1-42} resides with its C-terminus in the centre of the bilayer.

Experimental evidence has also been presented with systems containing cholesterol. Cholesterol is an essential component of eukaryotic cells [56] and is found in high concentration in neuronal synapses [87]. Dante *et al.* have measured the amyloid-β_{25-35} peptide in bilayers containing cholesterol [77]. They have shown that by increasing the amount of cholesterol in the bilayer, the percentage intercalated peptide decreases, with no observable signal for a sample containing 20 mol% cholesterol.

1.5.2 Dynamics of model membranes

The dynamic behaviour of a membrane is closely linked to the specific function or functions the membrane must perform. These dynamics occur over a wide range of time and length scales, with the larger properties of the bilayer arising from the properties of the molecular bilayer components.

The dynamics of model lipid membranes, made of many identical lipid molecules, can be divided into contributions from the head groups, the tails and the whole lipid. In experiments, these are observed as a superposition of motions, including trans-bilayer flip-flop, lateral diffusion, bilayer undulation and bending, protrusions out of the bilayer, rotation of whole molecules and molecular components, conformational changes and vibrations. These dynamics occur on length scales from Ångströms (local dynamics of single lipids) to tens of nanometres (bilayer undulation and bending), and from femtoseconds (molecular vibrations) to hundreds of seconds (trans-bilayer flip-flop) in time (see Figure 1.5). The long-range motion is interesting due to the impact it is expected to have on biological and pharmaceutically relevant bilayer properties, whereas the internal motions may be linked to transport across the membrane and trans-membrane protein processes.

The slowest bilayer dynamics are observable using mechanical (high-speed atomic force microscopy) or fluorescence based techniques [38, 39, 88, 89, 90, 91] (fluorescence correlation spectroscopy or fluorescence recovery after photobleaching). These techniques allow one to observe dynamic processes with relaxation times occurring on the ms and μs time-scale.

To observe faster processes, it is necessary to use techniques such as nuclear magnetic resonance (NMR), neutron scattering or molecular dynamics simulations. NMR can be used to observe processes with relaxations occurring on the ps to ms time-scale with pulse-field gradient and field cycling techniques [92, 93, 94, 95, 96, 97], whereas neutron scattering allows observation of processes occurring on the ps to ns range [34, 35, 98, 99]. Molecular dynamic simulations produce data which can be compared to these experimental techniques, with all-atom molecular dynamic simulations modelling processes from the fs to μs range [67, 100, 101]. Due to restrictions in computing

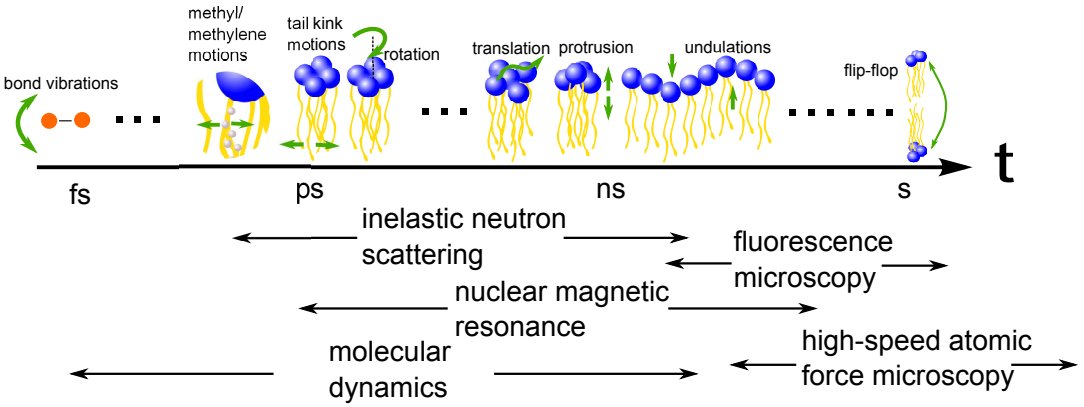

Figure 1.5: Typical relaxation times of dynamic processes of bilayer lipids. Each dynamic process is grouped according to the order of magnitude of the relaxations in time. A rough approximation of techniques used to measure (or simulate) each dynamic process is shown in the lower half of the diagram.

power, a trade-off is often made between the spatial dimensions of the system and the time-scales which are simulated.

For quasi-elastic neutron experiments (described in detail in Section 2.3) , which measure incoherent scattering primarily from hydrogen atoms in the lipids, the observation made is restricted by the instrumental resolution and the dynamic range of the instrument [29]. The interpretation of the data is model-dependent. A guide to constructing the models based on the instrumental parameters and the assumed type of motion is presented in Section 3.1.2. For lipid bilayer samples, models using convolutions of Lorentzian curves are often used, as this type of interpretation can be related back to physical parameters. Recent experimental results from single component lipid bilayers observe two [32] or three [31] dynamic processes (depending on instrumental resolution), with relaxation times separated by orders of magnitude. This includes a Brownian-like diffusion of the lipid centre-of-mass (with relaxation time on the nanosecond time-scale), and other contributions from the internal lipid dynamics, manifesting as restricted dynamics on the picosecond scale.

This interpretation can also be replicated by using molecular dynamic simulations. The observation of the lateral mean-square displacement allows one to characterize the type of dynamics occurring over various time-scales. Flenner *et al.*, have calculated the MSD over their entire simulation range, from ∼10 fs to ∼100 ns [27], as shown in Figure 1.6. In this plot, three distinct regions can be seen. On the femtosecond time-scale, the coefficient β of the centre of mass motion can be fit with β=2, a Gaussian distribution. This region corresponds to the unhindered, ballistic regime before the lipid starts to experience collisions with surrounding lipids. In the picosecond regime, the time-dependence of the stretching factor is fit at ∼0.68, defining a sub-diffusive regime. Finally, for times larger than a nanosecond, β approaches 1. In this case, the only contribution observed is from the long-range diffusion of the centre of mass. The

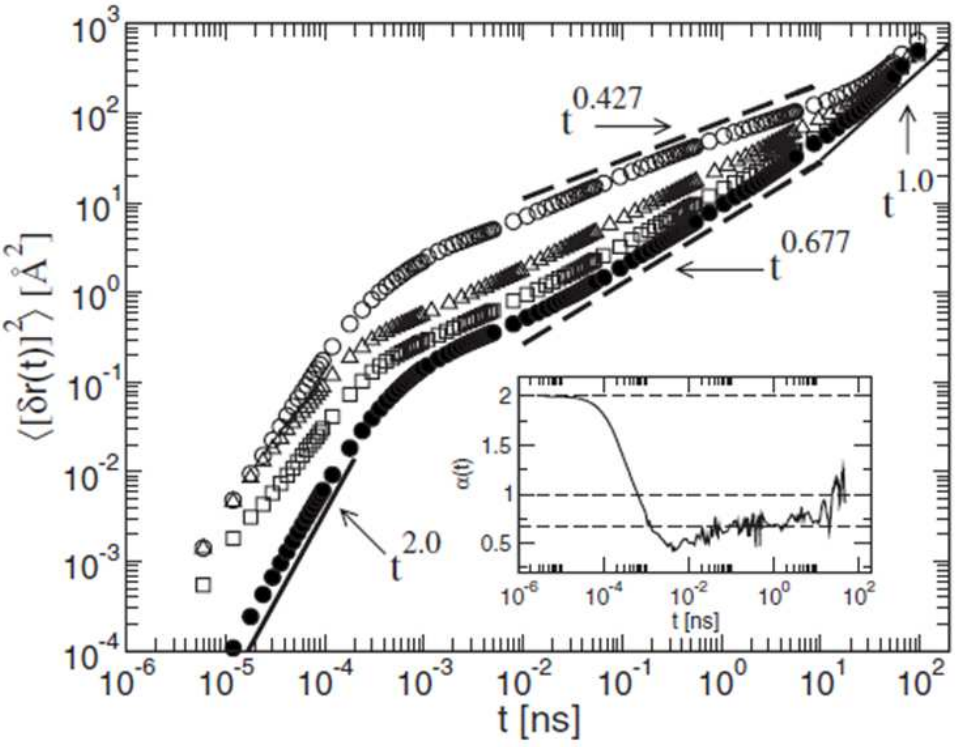

Figure 1.6: The mean-squared displacement of various atoms in a DMPC in a molecular dynamics simulation. The solid black symbols represent the centre of mass mean-square displacement of the lipid bilayer. The exponential dependence of the MSD with t defines the stretching of an exponential function of the autocorrelation function. Figure from Flenner *et al.*, 2009 [27].

sub-diffusive contributions approach the pure Brownian definition for long times. This type of simulation also leads to diffusion constants which can be compared, with good agreement, to experimental techniques [27, 28].

The first quasi-elastic neutron scattering experiment on lipid bilayers perturbed by amyloid-β peptides was performed by Buchsteiner *et al.* in 2010 [44]. This experiment was performed using an instrument with energy resolution (ΔE) of 93 μeV, which allows for dynamics happening on the picosecond time-range to be observed. In this paper, Buchsteiner presents two sets of dynamics; a "slow" process, with a typical relaxation time of ∼14 ps, and a "fast" process with a typical relaxation time of ∼4 ps. The slow dynamics were influenced by the addition of amyloid-β_{25-35}, with an acceleration of diffusion constants for temperatures far from the main-phase transition T_c, however near the phase transition a slowing is observed. The "fast" process did not show any change with the peptide presence.

A follow-up to this experiment in 2012, again by Buchsteiner *et al.* compares the amyloid-β_{25-35} to a larger amyloid-β_{22-40}, which is assumed to be the residues of

the full-length peptide which intercalates into the membrane (based on hydrophobicity arguments). These experiments were performed at 47°C, far above the main-phase transition temperature of the lipids. A fitting model using two Lorentzians was again used. A qualitative comparison between the two peptides shows both peptides seem to accelerate the lipid diffusion in the "slow" process, while no effect on the "fast" process is observed.

1.6 Thesis overview

This leaves open some of the scientific questions discussed in this thesis. First, the relaxation times of the fast and slow contributions observed by these neutron scattering measurements have been an order of magnitude faster than the nanosecond whole molecule diffusion predicted by molecular dynamics simulations. By using a combination of instruments with a range of instrumental resolutions, it may be possible to observe and deconvolute relaxations from one another, and to determine what effect an amyloid-β peptide fragment may have on these processes. Second, the interaction between various peptide fragments and cholesterol-rich membranes has not been systematically studied. By observing the location and changes in the bilayer structure with various amounts of cholesterol, a better understanding of this particular peptide, and the interaction of peptides and cholesterol-rich bilayers in general can be achieved.

The thesis is organized as follows: In this chapter the model biological membrane system is introduced and a review of existing literature involving this system is presented. Chapter 2 contains the theoretical principles and descriptions of instruments and techniques used to study the system. In Chapter 3 experiments on model lipid membranes with fragments of the (amyloid-β_{22-40}) are presented, particularly structural and dynamical changes induced by the peptide in a two component lipid membrane. In Chapter 4 structure and dynamic changes induced by the amyloid-β_{22-40} and the full-length amyloid-β_{1-42} in more complex model membranes containing cholesterol are investigated. In Chapter 5 techniques to control humidity for neutron scattering experiments are discussed, and the development of an improved variable humidity and temperature neutron scattering sample environment is presented, as well as experimental results from the commissioning of the chamber. Finally, in Chapter 6 the results of all studies are presented together and future experimental direction is discussed.

2 Experimental techniques

2.1 Scattering techniques

The lipid bilayer samples described in Chapter 1 have the periodicity and order which allows for the study of their properties with X-ray or neutron scattering experiments. Properties of matter have been probed with radiation since W. C. Röntgen first discovered X-ray radiation in 1895, for this discovery, he was awarded the very first *Nobel Prize in Physics* in 1901 [102]. Only a decade later, two more Nobel Prizes were awarded to Max von Laue (1914 [103]) and the father and son William Henry Bragg and William Lawrence Bragg (1915 [104]) for the discovery of diffraction of X-rays by crystals, and for furthering the analysis of crystal structures by means of X-ray, respectively. Neutrons were discovered a generation after X-ray radiation in 1932 by James Chadwick [105], and in 1935 he was awarded the *Nobel Prize in Physics* for this discovery [106]. Techniques and instrumentation for neutron scattering experiments were developed in the 1950s and 1960s, for which the *Nobel Prize in Physics* was awarded to Clifford Shull and Bertram Brockhouse many years later in 1994 [107]. These and other advancements in the fields of X-ray and neutron scattering have lead to a variety of techniques to manipulate and observe the interactions of photons and neutrons with various complex samples. Scattering of X-ray and neutron radiation has provided insight into the structural parameters and the dynamic properties of a diverse range of materials and systems including super-conductors and other magnetic materials, metals, polymers and biological materials (including protein crystals and lipid bilayers).

Both X-rays and neutrons can be used for scattering experiments, although the properties of X-rays [108] and neutrons [109] have some substantial differences. Some physical properties of X-rays, neutrons (and electrons, for comparison) are listed in Table 2.1. Experiments with X-ray radiation are often the preferred technique due to the ease of production (bench-top, in-house sources exist) and the high flux. Because the X-ray photons interact with the electrons of a sample, there is a limit of the thickness of samples and the complexity of the experimental sample environment [110]. Although the production of neutrons is much more involved and the intensity is significantly lower, a few of the properties of neutrons make neutron scattering an attractive choice. First, neutrons can penetrate much deeper into a sample (deeper than electrons or protons, which are hindered by the electrostatic repulsion), because neutrons have no charge [105]. This results in high transmission, which has both scientific and technical advantages. Thick samples can be used, as the neutrons penetrate deeply, and complex sample environments can be constructed (typically from aluminum, due to its high

transmission) allowing for experiments with sealed, "windowless", containers which can achieve high pressure, well defined atmosphere (inert gas, high humidity) and unique magnetic conditions. Second, neutrons scatter coherently and incoherently, which allows the observation of incoherent dynamics [109, 111]. Third, the neutron scattering cross sections are not dependent on the sample's atomic number, which allows for contrast variation and substitution, especially with the biologically relevant hydrogen isotopes ^1H and ^2H [112]. Finally, neutrons have magnetic properties which allow for observation of magnetic phenomena not possible with X-rays. Often a combination of X-ray and neutron experiments are performed to take advantage of both types of probes.

Table 2.1: Properties of common scattering probes

	X-ray	neutron	electron
mass	-	$1.68\text{x}10^{-27}$ kg	$9.11\text{x}10^{-31}$ kg
charge	-	-	-1 e
spin	-	s=$\hbar/2$	s=$\pm\hbar/2$
velocity	c	$\leq$10 000 m/s	$<$c
momentum	$\hbar$/c	mv	mv
energy	$\frac{hc}{\lambda}$	$\frac{1}{2}mv^2$	$\frac{1}{2}mv^2$
magnetic moment	-	$-9.65\text{x}10^{-27}$J/T	$9.27\text{x}10^{-24}$J/T
typical energy range	100 eV to 100 keV	1 meV to 500 meV	20 eV to 50 keV

2.1.1 X-ray and neutron production

The production of X-rays can be done on the large scale with a synchrotron, and on the small scale with a high-voltage anode in lab-based set-ups. In a synchrotron, a charged particle (proton or electron) is accelerated to relativistic speeds then bent with powerful magnets. During the bending, photons with high energies and broad spectra are produced. These photons pass through focusing and monochromating optics, interact with the sample and are counted by detectors around the sample. Alternatively, an in-house set-up offers convenience but with significantly lower intensities. X-rays are produced by accelerating electrons with an electric field to a high speed in vacuum, towards a metal target (the anode). The voltage involved is typically 10s of kV, which generates a continuous radiation through the *Bremsstrahlung* radiation process. High intensity, narrow wavelength bandwidth K_α and K_β peaks are produced, with the wavelength depending on the type of metal used for the anode.

The production of neutrons is limited to large-scale facilities. Neutrons are produced either by a reactor or at a spallation source. A reactor source produces a continuous neutron flux through a fission reaction held at criticality with a water or heavy-water moderator. In the fission process (see Figure 2.1), the decay of a heavy atom such as uranium is induced by a collision with a neutron. The nucleus, now heavier by one additional neutron, decays into smaller daughter nuclei and releases two to

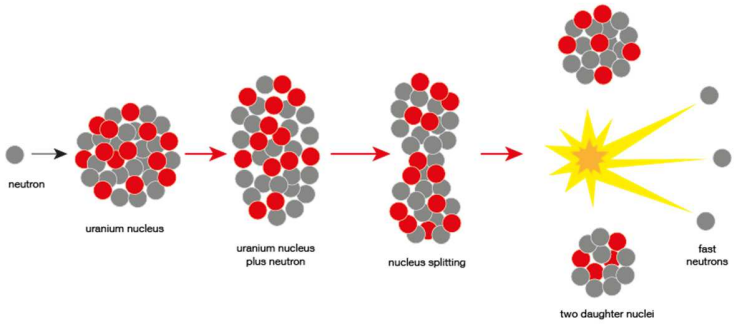

Figure 2.1: A nuclear fission reaction. Figure from FRM-II [113]

three additional neutrons. On average, one neutron continues on to induce the next fission reaction, while the remaining neutrons are extracted and used for experiments. Around the reactor core, neutron guides provide a pathway for the neutrons to exit the containment vessel and travel to the instruments. These guides may originate from the pool moderator, or from cooled or heated "sources", devices which shift the neutron energy higher or lower through collisions with a heated or cooled medium. Details are shown in Table 2.2. Examples of neutron reactor sources are the BER-II reactor at the Helmholtz-Zentrum Berlin in Berlin, Germany, the reactor at the Institut Laue-Langevin in Grenoble, France and the FRM-II reactor at the Maier-Leibnitz Zentrum in Garching, Germany, among others. All of the neutron experiments contained in this thesis have been performed at these reactor neutron sources. The typical flux of a fission reactor source is on the order of 10^{15} neutrons·cm^{-2}·s^{-1}, and is limited by the ability to remove heat from the reactor core. As such, it is unlikely that a reactor source with a significantly larger flux could be constructed.

To achieve larger neutron flux, spallation neutron sources have been implemented [114]. In a spallation source, protons are linearly accelerated to high velocities, and collide with a target made of heavy metal. This collision releases neutrons from the target's nuclei. Since the protons arrive in pulsed bundles, the resulting neutrons are also produced in pulses. Due to the lower heat produced by this technique, larger neutron flux on the order of 10^{17} neutrons·cm^{-2}·s^{-1} may be produced, although not in a continuous manner. Spallation sources exist at the SNS (Oakridge, USA), ISIS (Oxford, UK), PSI (Zurich, Switzerland), J-PARC (Tokai, Japan) and soon the ESS (Lund, Sweden).

2.1.2 Scattering theory

A scattering experiment relies on precise knowledge of the geometry and energy of the incident and scattered beam. Changes in the scattering angle or the energy of the photon or neutron relate to physical properties of the sample. The most common way to discuss a scattering experiment is in reciprocal space, defining a wavevector ($\vec{k}$) for the incident and final radiation, as is shown in Figure 2.2. The magnitude of $\vec{k}$ can be

	Cold	Thermal	Hot
Moderator	H_2/D_2	H_2O/D_2O	Graphite
Temperature (K)	25	300	2000
E (meV)	1-5	5-100	100-500
λ (Å)	3-30 Å	1-4 Å	0.4-1 Å
v (m/s)	700	2000	10 000
Samples	soft matter	condensed matter	condensed matter
	biology	magnetism	atomic structure
	magnetism	crystal structure	liquids

Table 2.2: Properties of cold, thermal and hot neutron sources.

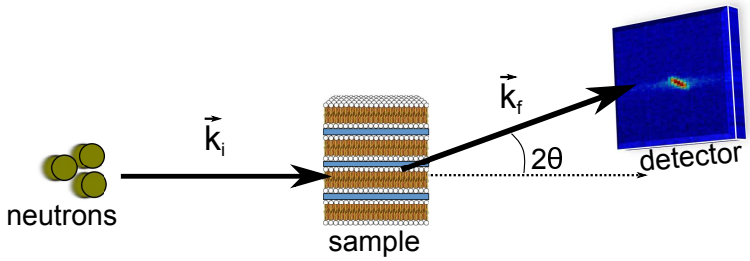

Figure 2.2: A typical scattering experiment.

directly converted back to real-space with $\left|\vec{k}\right| = 2\pi/\lambda$. One can describe the resulting difference between the final and initial wavevector with the reciprocal scattering vector $\vec{Q}$, constructed from a scattering triangle as is shown in Figure 2.3, with the scattering angle between the k_i and k_f vectors called 2θ.

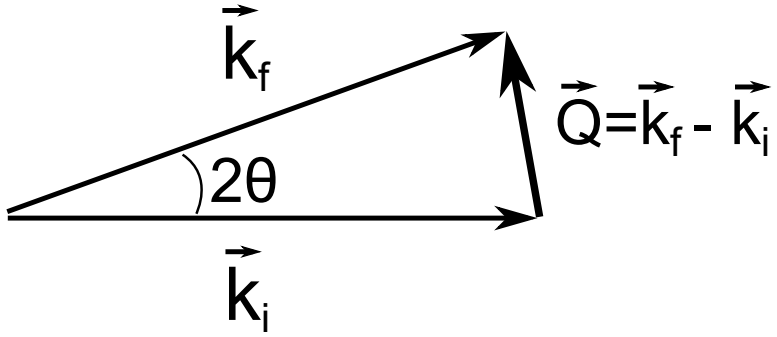

Figure 2.3: The scattering triangle, with the scattering vector $\vec{Q}$ defined as the vector subtraction of $\vec{k_i}$ from $\vec{k_f}$.

Depending on the set-up of the instrument used for the scattering experiment, information about elastic (no energy gain or loss during scattering) or inelastic (a gain or loss of energy through scattering) collisions can be gathered. For both X-rays

and for neutrons, the radiation may be treated as a particle or a wave, depending on what experimental conditions are to be probed. In the case of elastic scattering, the scattered particle's energy remains unchanged during a scattering event, which extends to an unchanged wavelength (λ) using the Planck-Einstein relation for photons (Equation 2.1), and the de Broglie relation for neutrons (Equation 2.2). The elastic scattering for a large number of collisions forms interference patterns, which reveal details of the structure and order of the sample. This type of experiment is referred to as a *Diffraction experiment*, and will be further discussed in Section 2.2.

$$E_{wave} = pc = \hbar kc = \frac{hc}{\lambda} \tag{2.1}$$

$$E_{particle} = \frac{p^2}{2m} = \frac{\hbar^2 k^2}{2m\lambda^2} \tag{2.2}$$

In the inelastic case, the scattered particle will gain or lose energy by interacting with a sample particle with kinetic energy of comparable magnitude. The change in energy between the scatterer pre- and post-collision is then analysed to determine dynamics of the sample. The principles of inelastic scattering techniques, in particular relating to quasi-elastic neutron scattering, will be discussed in section 2.3. Elastic and inelastic scattering can be used to study both the structural and dynamic properties of biological samples, using advantages provided by both X-rays and neutrons as scattering probes.

With neutron probes, a further separation of dynamics is possible by tailoring the experiment to observe either coherent or incoherent scattering. Coherent scattering arises from the constructive interference between wavelengths, and thus requires an ordered sample. Coherent dynamics describe structure or shape as well as the excitations of a lattice (phonons or magnons). Incoherent scattering arises from the interference of neutrons scattering from a single particle at different times. Dynamics probed by incoherent scattering can include both diffusive dynamics, with an average scattering centred around a zero energy transfer, and molecular vibrations which centre around a non-zero energy transfer value.

2.2 Structural measurements

A scattering experiment in which only elastic collisions are considered gives information of the equilibrium structure of the system. Particles scatter from crystal or semi-crystal structures in the system, resulting in an interference pattern which can be described by the Bragg relation (Equation 2.3, and Equation 2.4 in reciprocal space), and is shown in Figure 2.4. Constructive interference occurs if twice the spacing (d) multiplied by the sine of the angle (θ) is a integer multiple of the wavelength of the wave.

$$n\lambda = 2dsin(\theta) \tag{2.3}$$

$$\left|\vec{Q}\right| = \frac{4\pi sin(\theta)}{n\lambda} \tag{2.4}$$

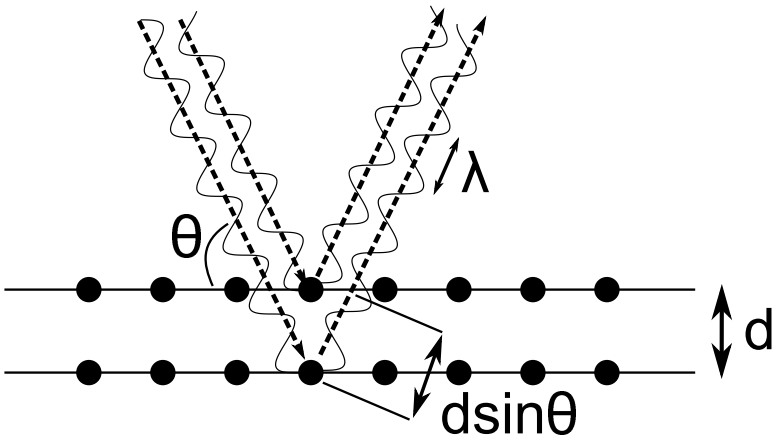

Figure 2.4: A pictorial description of the Bragg condition.

To measure a scattering event, one must consider the total scattering of the system, and determine how this relates to the detectable scattering. The total scattering from the system (σ_{total}) is defined over a solid angle Ω (Equation 2.5). Due to instrumental constraints, and because most of the scattering occurs in the forward direction, detectors are built to observe only a selected section of the solid angle. The differential cross section is thus defined as a geometrical portion of the total scattering, and can be defined by the incident and final wavevectors ($\vec{k_i}$ and $\vec{k_f}$), the scattering length of the sample (b) and the structure factor of the sample ($S(Q)$), as shown in Equation 2.6 and in Figure 2.5. This is a simplification of the double differential cross section which will be discussed in more detail in Section 2.3.

$$\sigma_{total} = \int_0^{4\pi} \frac{\mathrm{d}\sigma}{\mathrm{d}\Omega}\mathrm{d}\Omega \tag{2.5}$$

$$\frac{\mathrm{d}\sigma}{\mathrm{d}\Omega} = \frac{k_f b^2}{k_i} S(Q) \tag{2.6}$$

The scattering length of elements differs for the X-ray and neutron case. The X-ray scattering length scales linearly with the atomic number of the element, whereas for neutrons the scattering length does not follow such behaviour. The neutron scattering length does not depend on the size of the nucleus, and must be experimentally determined for each atom. In fact, isotopes of the same atom can have drastically different scattering lengths (*cf.* ^{1}H and ^{2}H). This difference is often exploited in neutron scattering experiments, to determine the phase input to the Fourier transformation, through contrast variation. The contrast variation approach will be discussed in section 2.2.2. The scattering length of some elements commonly found in biological

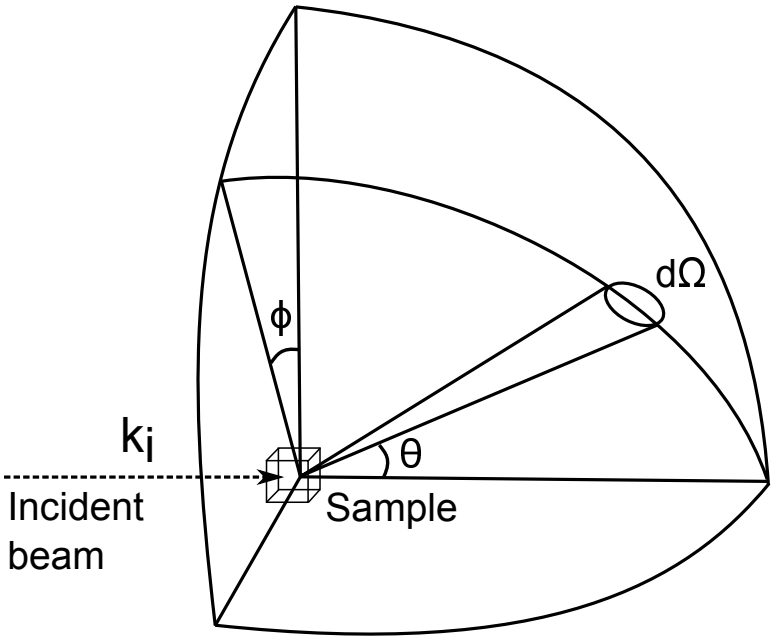

Figure 2.5: The scattering differential defined for a section of solid angle Ω.

samples are listed in Table 2.3. Below, the X-ray and neutron approaches to studying structure are discussed.

Table 2.3: X-ray and neutron scattering length of biologically relevant elements [112]

Element	Z	b_{X-ray} (x10^{-13} cm)	$b_{neutron}$ (x10^{-13} cm)
^{1}H	1	**3.8**	**-3.74**
D (^{2}H)	1	**3.8**	**6.67**
C	6	16.8	6.65
N	7	19.7	9.36
O	8	22.5	5.80
P	15	42.3	5.13
S	16	45.0	2.85

2.2.1 X-ray diffraction

Experiments contained in this thesis using the X-ray diffraction technique were performed using the Biological Large Angle Diffraction Experiment (BLADE) a Rigaku SmartLab X-ray diffraction system set-up at McMaster University in Hamilton, Canada. BLADE uses a copper rotating anode to produce photons with a broad, continuous energy spectrum, a result of *Bremsstrahlung* radiation. Sharp peaks are

also present, defined by the energy difference between electron shells. In particular, due to the copper anode, a narrow K_α peak with wavelength of 1.541 Å is produced. BLADE is operated with a maximum voltage of 45 kV and a maximum current of 200 mA, producing 10^{10} photons mm^{-2} s^{-1}.

The photons pass through collimators and slits which focus the beam. The X-ray source and point detector are on moveable arms which move on the surface of the Ewald sphere. This allows simple calculation of the scattering in reciprocal space, and has the advantage of a stationary and horizontal sample. The detector will scan along the horizontal and vertical directions, counting at each position, and observing the constructive and destructive interference relating to in and out-of-plane structure. A diagram of the set-up is found in Figure 2.6.

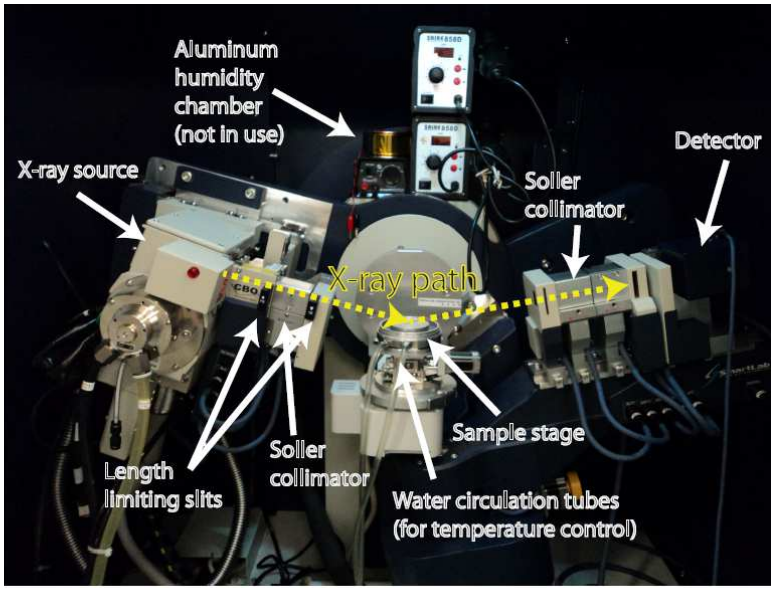

Figure 2.6: General overview of the BLADE X-ray diffractometer. The X-ray path, optics, sample stage and hydration chamber inside the BLADE casing. Figure reproduced from [115].

A typical scan with BLADE lasts approximately 18 hours, and produces a two dimensional reciprocal space map covering -0.3 to 3.1 $Å^{-1}$ in $\vec{Q}_{parallel}$ and from 0 to 1.2 $Å^{-1}$ in $\vec{Q}_{perpendicular}$. With this 2D map, a reconstruction of the features leading to scattering (i.e. reflectivity) is possible from the perpendicular (out of plane) data at $\vec{Q}_{parallel}$=0 (see Figure 2.7). Often the goal of a X-ray diffraction experiment is to reconstruct the structure of the bilayer. With oriented samples, it is possible to determine both in- and out-of plane structural details.

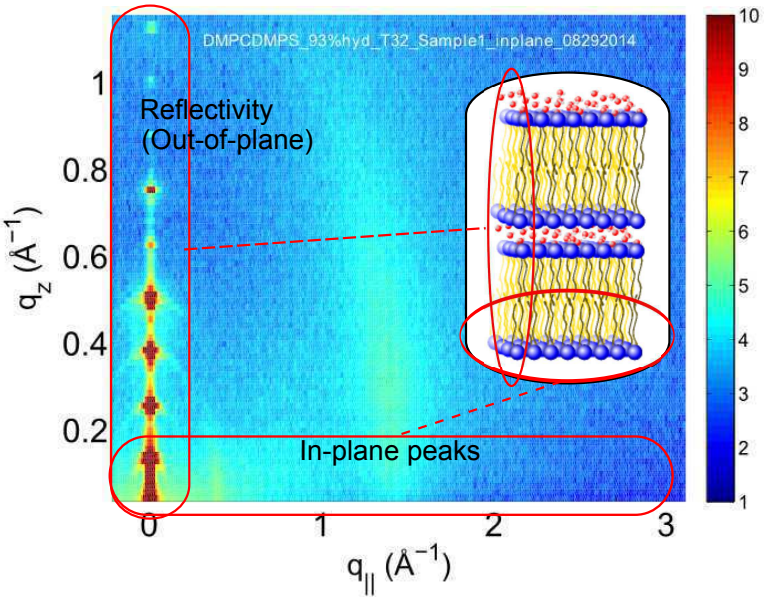

Figure 2.7: A typical 2D reciprocal space map of a stacked lipid bilayer (DMPC/DMPS) sample at 93% relative humidity and 32°C. Inset image of bilayer with corresponding reflectivity signal at $\vec{Q}_{parallel}$=0, and in-plane signal at $\vec{Q}_{perpendicular}$=0. Details are reconstructed through a Fourier treatment (to be discussed in the following section).

Diffraction analysis

The structural details of the out-of-plane scattering are obtained from Fourier analysis of the peaks centred at $\vec{Q}_{parallel}$=0. The spacing between these peaks directly provides the bilayer repeat distance, the *d-spacing*, by $d = 2\pi/(Q_n - Q_{n-1})$, as demonstrated in Figure 2.8.

First, the position of each peak in the spectrum is determined from the reflectivity curve. Plotting either the sine of the angle (or simply the magnitude of Q in reciprocal space) against the order of the reflection, n, one expects a linear relationship ($\sin(\theta)/n = \lambda/2d$ or $Q/n = 2\pi/d$). If satellite peaks are present, and result in a linear fit with a different slope, this indicates the presence of multiple domains with different d-spacings in the sample (e.g. a coexistence of multiple lipid phases).

If no secondary domains are observed (all peaks relate to a single d-spacing), the out-of-plane bilayer structure can be reconstructed using a Fourier summation (in the presence of multiple domains, Fourier reconstruction becomes non-trivial). The integral area (I(n)) of the peak relating to each reflection is determined, and used to calculate the form factor (F(n), Equation 2.7) of each reflection [116]. The form factor is related to the square-root of the peak intensity along with various experimental corrections, multiplied by the Fourier phase factor $e^{i\varphi_n}$ (discussed below). For these reflectivity experiments corrections for the absorption, and the Lorentz factor should be considered.

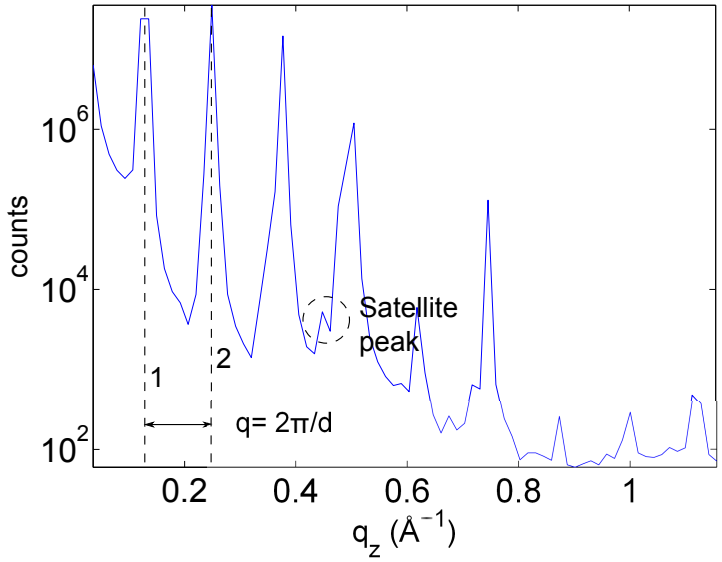

Figure 2.8: A reflectivity curve extracted from Figure 2.7, taking the vertical peaks centred at $\vec{Q}_{parallel}$=0. The spacing between adjacent peaks defines the d-spacing, displayed here for the first and second reflections. Smaller satellite peaks are often observed in a multi-component membrane, indicating sub-domains or defects.

Other factors such as the multiplicity factor and polarization are not considered, as lamellar samples do not result in symmetry-equivalent peaks coinciding on the detector (e.g. in rhombohedrial phases), and the X-ray tube produces unpolarized radiation. The absorption correction is necessary as the X-ray beam passes through a different amount of sample, depending on its angle of incidence. For most biological samples, low atomic number elements present in the sample, and relatively thin samples, result in negligible absorption, and A(n) is approximated at ∼1 . The Lorentz correction accounts for geometrical factors related to reflecting planes within the sample, which will change the detected intensity [117].

$$F(n) = \sqrt{I(n)A(n)sin(\theta)} \cdot e^{i\varphi_n} \tag{2.7}$$

The calculated form factor of each peak (2.7) is then summed to determine the electron density of a unit cell, calculated using Equation 2.8, with ρ_o the total electron density of the unit cell (calculated by considering the components of the sample), k a scaling factor (determined by assuming the electron density at certain points of the unit cell - i.e., the water electron density between bilayers) and d the experimentally determined d-spacing. The theoretical electron density is a summation over an infinite amount of form factors, but for X-ray diffraction experiments this infinite sum is truncated to the amount of observable Bragg reflections, typically less than 10 for

a lipid bilayer sample.

$$\rho(z) = \rho_o + (\frac{2}{kd}) \sum_{n=1}^{n_{max}} F(n) \tag{2.8}$$

The Fourier phase factors, $e^{i\varphi_n}$, are not determined directly by the measurement from the X-ray detector. Only the projection of the complex wave-vector onto the detector is detectable. This projection provides a measurement of the amplitude, neglecting the imaginary part (phase) of the form factor. This loss of information is a common occurrence in scattering, imaging and signal processing, and is referred to as the *phase problem*. For determination of the electron density of a lamellar system, perpendicular to the bilayer plane, we assume a centro-symmetric density ($\rho(-z) = \rho(z)$). This assumption allows one to replace the complex $e^{i\varphi_n} = cos(\varphi_n) + i \cdot sin(\varphi_n)$ by $v(n) \cdot cos(\varphi_n)$, where $v(n) = \pm 1$, thus simplifying a potentially infinite phase coefficient to two values. The scattering density is now displayed in its simplified form in Equation 2.9 [118].

$$\rho(z) = \rho_o + (\frac{2}{kd}) \sum_{n=1}^{n_{max}} v(n) \, |F(n)| \, cos\left(\frac{2\pi n z}{d}\right) \tag{2.9}$$

This simplification is still not enough to confidently assign phases to the Fourier reconstruction, as the number of potential combinations is 2^n (for a typical measurement of n=8 reflections giving 256 potential phases). With X-ray reflectivity measurements, a common strategy is to determine the sign of the form factor by gradually varying the hydration of the bilayer through humidity [115]. Hydration water enters the bilayer and causes dramatic changes in the unit cell resulting in increasing or decreasing reflectivity intensities, and thus changing form factors. This will be discussed further in Chapter 5 [119].

Once the d-spacing, whole unit cell electron density, form factors and crystallographic phases corresponding to each peak are determined, the Fourier reconstruction may be performed.

To compare samples, it is necessary to rescale the electron densities with the scaling factor k. The resulting scaled electron densities can then be overlaid or subtracted, to determine small structural changes present. This analysis is presented in Chapters 3 and 4.

In-plane analysis

Along with the reflectivity data used to generate the out-of-plane electron density, in-plane peaks also exist in the two dimensional reciprocal space map (Figure 2.7). The ordering of the bilayer is not as regular in-plane when compared to the out-of-plane reflectivity measurement, and consequently, the primary peak is wider and higher orders are not observable. The broad peak observed at $\sim$1.4 Å^{-1} is assigned to the mean spacing between lipid tails ($\sim$4.5 Å in real-space). Other more well defined peaks may

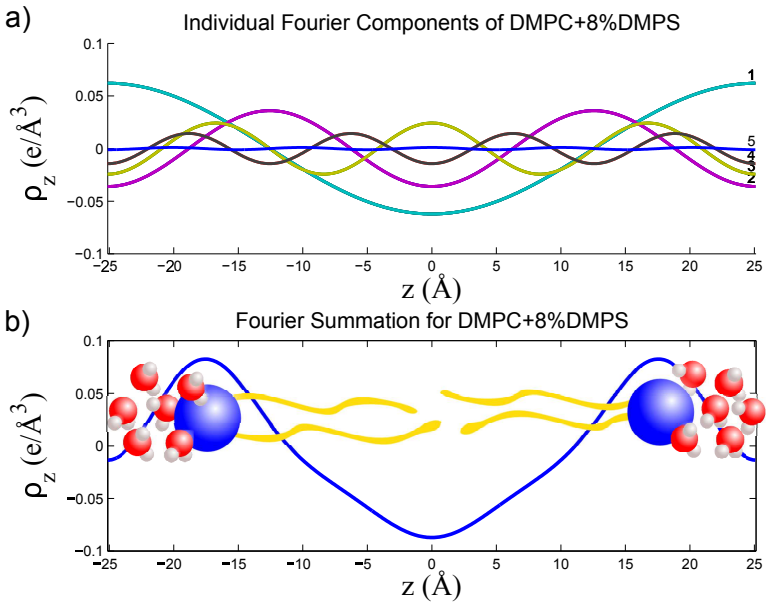

Figure 2.9: a) Individual Fourier components corresponding to the first five reflections. b) Unscaled summation of electron density components in *a*), lipid and water molecules overlaid to give a general idea of bilayer structure. The highest electron density is found at the head-group region of the lipids, due to the high concentration of heavy elements (phosphorous, oxygen) in the headgroups. The lowest electron density is found in the tail groups, where only carbon and hydrogen are present.

also be present, especially when more stable ordered structures form. The size and geometry of these ordered structures can then be determined through peak assignments.

It is often the case that one observes in-plane peaks which are not vertical, but exhibit some smearing or bending. This is the result of anisotropy in the sample, leading to a bending of the bilayer or the presence of multiple domains which do not join together. By integrating these peaks radially, analysis of the bending of the bilayer may be performed.

2.2.2 Neutron diffraction

Neutron diffraction experiments were carried out using V1 at BER-II reactor at Helmholtz- Zentrum Berlin (HZB, Germany), using MIRA at the FRM-II reactor at the Heinz Maier-Leibnitz Zentrum in Munich and at the D16 diffractometer at the Institut Laue-Langevin in Grenoble, France. The three instruments are very similar (see Table 2.4 for a comparison), although MIRA has additional features which allow for a wider range of experiments. V1 is typically used to measure biological membranes in diffraction set-up, whereas at MIRA, the polarization and triple-axis option (analyser) allows for magnetic excitations and other magnetic phenomena to be captured and D16

can be used in small angle geometry. In the scope of this thesis, V1, MIRA and D16 were all used in identical set-ups, with only small differences in the incident wavelength and detector geometry.

Table 2.4: Comparison of V1, MIRA, D16 diffractometers (HZB Website, FRMII Website, ILL Website)

Instrument	**V1 (HZB)**	**MIRA (FRM-II)**	**D16 (ILL)**
Location	Berlin	Munich	Grenoble
Reactor power (MW)	10	20	58
Flux at sample (n^o s^{-1} cm^{-2})	$1{\cdot}10^7$	$1{\cdot}10^7$	$1 \cdot 10^7$
Wavelength used (Å)	4.567	4.7	4.7
Monochromator	PG (002)	PG (002)	PG (002)
Detector type	^{3}He	^{10}B	^{3}He
Detector size (cm^2)	19x19	20x20	32x32
Detector pixel size (mm^2)	1.5x1.5	1x2	1x1
Polarization	No	Yes	No
Analyser	No	Yes	No

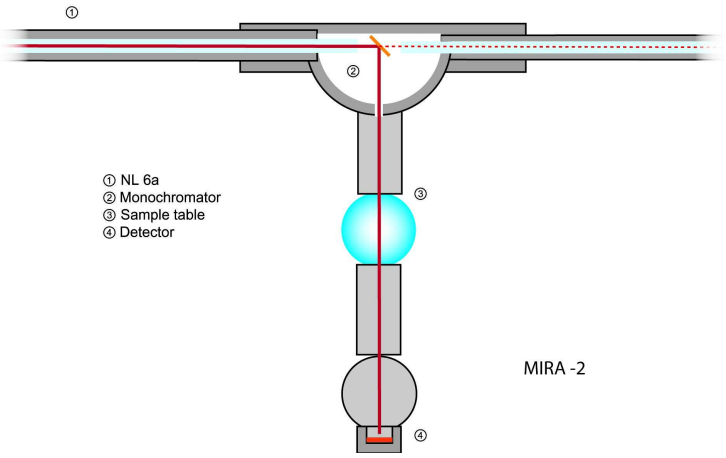

Figure 2.10: Set-up of the MIRA diffractometer at the Heinz Maier-Leibnitz Zentrum in position 2. The incident beam leaves the neutron guide (NL6a) after passing through the monochromator (2), diffracts through the sample (3), then is captured by the detector (4). The analyser is shown by the circular shape before the detector, but was not used in this set-up. Figure from FRMII Website.

The set-up of the MIRA diffractometer in position 2 (geometry for smaller incident wavelength) is shown in Figure 2.10. In this set-up, the wavelength of the neutrons leaving the monochromator is well defined (∼4.7 Å). The rotation of the sample generates sample constructive interference from neutrons resulting in Bragg peaks on

the detector, corresponding to Equation 2.3. The detector is also moveable, and can be positioned to capture peaks at an angle up to 2θ=60°. For the lipid bilayer samples measured, each sample produced between 5 and 6 Bragg peaks. Higher orders were not detectable due the intrinsic disorder of the membrane and the background noise.

The V1 diffractometer at HZB was also used. A photo of the V1 membrane diffractometer in Figure 2.11 shows the instrument.

Figure 2.11: An overhead view of the V1 membrane diffractometer. Photo courtesy of Thomas Hauß, V1, HZB.

Neutron diffraction analysis is handled similarly to X-ray diffraction (discussed previously in Section 2.2.1), with some advantages and other techniques due to the neutron scattering lengths. As is shown in Table 2.3, the neutron scattering length of atoms does not depend on the atomic number, but is a seemingly arbitrary value which must be experimentally measured. It is worth noting the difference between the isotopes of hydrogen, with b_{1H}=-3.74· 10^{-13} and b_{2H}=6.67· 10^{-13} cm.

One advantage of neutron diffraction is the contrast difference between ^1H and ^2H (or D) can be used for tagging specific atoms. Tagging of atoms using a substitution

of hydrogen isotopes is a useful way to determine position or structural details of a molecule in the unit cell. The substitution of hydrogen with deuterium is possible in polymers, lipids or even in proteins. Since the isotopes have almost the same chemical behaviour, structural changes are minimal . This is in contrast to tagging with fluorescent markers in optical measurements or heavy atom tagging for X-rays, which may influence structure or dynamics of molecules of interest. In this thesis, substitution of deuterated amino acids into the amyloid-β protein was used to determine the position of the protein within the lipid bilayer discussed in Chapter 3.

The hydrogen and deuterium scattering length difference also allows one to resolve the phase problem. Although the hydration swelling method is also used in neutron scattering, a unique feature of neutron scattering length differences of hydrogen isotopes allows one to solve the crystallographic phase problem by changing hydration water deuterium content. By using different concentrations of deuterated water (D_2O) in the humidity sample environment, changes in the form factor relating to different H_2O/D_2O ratios can be observed and used to determine Fourier coefficients. A minimum of three H_2O/D_2O ratios are necessary to determine the phase of a centro-symmetric sample, and to check if it passes through an extinction. The sample must contain a significant amount of hydration water in its unit cell to take advantage of this technique, and the number of water molecules per unit cell should remain constant. The number of water molecules is held constant with a humidity controlled environment.

The form factor of each peak should be linear, when plotted against the H_2O/D_2O ratio. With this in mind, one can assign the $v(n) = \pm 1$ values unambiguously.

In a similar way to the X-ray diffraction example, the samples are scaled such that the neutron scattering length density either agrees with calculated values for certain regions of the unit cell, or behaves consistently among samples. At this point, the difference between samples with and without deuterated tagging may be plotted together and the location of the tagged molecules determined.

2.3 Dynamic measurements

Scattering experiments can also be used to measure sample dynamics. Dynamic properties of the sample are reflected as energy changes induced by inelastic collisions of scattered particles. Such energy gains or losses can be measured using an instrument that is sensitive to the incident and scattered energy of the neutrons. Instead of a single differential scattering cross section, as in Figure 2.5, the energy is also considered. The result is the double differential cross section, Equation 2.11.

$$\sigma_{total} = \int_0^{4\pi} \int_{E=-\infty}^{\infty} \frac{\mathrm{d}\sigma}{\mathrm{d}\Omega} \mathrm{d}\Omega \mathrm{d}E \tag{2.10}$$

$$\frac{\mathrm{d}^2\sigma}{\mathrm{d}\Omega \mathrm{d}\hbar\omega} = \frac{k_f}{k_i} \left\langle b^2 \right\rangle S(Q, \hbar\omega) \tag{2.11}$$

This treatment allows measurement of the dynamic structure factor, $S(Q, \hbar\omega)$. In

this case, the measurement of energy allows us to detect the various contributions to the scattering length. The total scattering length (b) is related to the total scattering cross section by $\sigma_{tot} = 4\pi b^2$. The total cross section σ_{tot} is defined as the sum of the incoherent and coherent scattering cross sections, that is $\sigma_{tot} = \sigma_{coh} + \sigma_{inc} + \sigma_{absorption} + \sigma_{magnetic\ contributions} + \ldots$

To understand these contributions, we think about the scattering process caused by a neutron interacting with the atomic nuclei in the sample. The scattering from the sample depends on the scattering length, which depends on two factors: 1) the type of isotopes in the sample and 2) the orientation of the nuclear spin of each nucleus. This implies that even for a sample consisting of a single type of isotope, there is potential for different scattering lengths [111].

Coherent scattering occurs when every atom in the system possesses a scattering length equal to the average scattering length $\langle b \rangle$, which defines the coherent cross section $\sigma_{coh} = 4\pi \langle b \rangle^2$. The coherent scattering arises from the interference of waves interacting with the many nuclei in the sample.

Incoherent scattering arises from the correlation of the same atom in time. The waves interacting with individual atoms do not interfere with each other, as in the coherent case. The incoherent scattering cross section is defined as the difference between the total scattering cross section and the coherent scattering cross section, shown in Equation 2.13.

$$\sigma_{inc} = \sigma_{tot} - \sigma_{coh} \tag{2.12}$$

$$\sigma_{inc} = 4\pi \left[b^2 - \langle b \rangle^2 \right] \tag{2.13}$$

In the elastic case, presented in Section 2.2, the detectors see the interference from coherent scattering, and incoherent scattering results in an isotropic, angle independent background.

The dynamic structure factor, $S(\vec{Q}, \hbar\omega)$ relates back to an intermediate scattering function $I(\vec{Q}, t)$, and a real-space correlation function $G(\vec{r}, t)$ through Fourier transformations. These relationships are discussed in the following section.

2.3.1 The van Hove formalism

In 1954, Leon van Hove introduced a mathematical formalism which links various experimentally accessible functions describing particle correlation and time evolution together through Fourier transformations [120]. In this quantum-mechanical treatment of scattering events, the scattering can be represented in terms of energy, scattering vector $\vec{Q}$, or their reciprocals: time and position. Different techniques allow measurements of these values, and transforming between them can ease the interpretation of data. The various correlation functions are also separable in terms of the coherent and incoherent scattering, which further eases interpretation.

The measurable double differential scattering cross section can be written as:

$$\frac{\mathrm{d}^2\sigma}{\mathrm{d}\Omega\mathrm{d}\hbar\omega} = \frac{k_f}{k_i}\frac{1}{2\pi\hbar}\sum_{jj'}\left\langle b_j b'_j\right\rangle \int_{-\infty}^{\infty}\left\langle exp\left\{-i\vec{Q}\cdot\vec{R}_j(0)\right\} exp\left\{i\vec{Q}\cdot\vec{R}_{j'}(t)\right\}\right\rangle e^{-i\omega t}dt \tag{2.14}$$

with $\vec{R}_j(t)$ the position of a scatterer at time t, and b_j the scattering length. The measured double differential cross section can be split into a coherent and incoherent part. In Equations 2.17 and 2.18, the dynamic structure factor $S(Q,\hbar\omega)$ is written in a way which allows treatment of the coherent and incoherent scattering separately. In the coherent double differential, the summation is over different particles, all j and j'. Correlations considered here are from different nuclei at different times, preserving the phase relationship between incident and scattered neutrons and thus leads to interference scattering. The incoherent case, however, is a summation over individual particles, j, and compares the position of the same nuclei with time. This excludes the phase relationship between incident and scattered neturons, and does not result in interference scattering.

$$\left(\frac{\mathrm{d}^2\sigma}{\mathrm{d}\Omega\mathrm{d}\hbar\omega}\right)_{coh} = \frac{\sigma_{coh}}{4\pi}\frac{k_f}{k_i}\frac{1}{2\pi\hbar}\sum_{jj'}\int_{-\infty}^{\infty}\left\langle exp\left\{-i\vec{Q}\cdot\vec{R}_j(0)\right\} exp\left\{i\vec{Q}\cdot\vec{R}_{j'}(t)\right\}\right\rangle e^{-i\omega t}dt \tag{2.15}$$

$$\left(\frac{\mathrm{d}^2\sigma}{\mathrm{d}\Omega\mathrm{d}\hbar\omega}\right)_{inc} = \frac{\sigma_{inc}}{4\pi}\frac{k_f}{k_i}\frac{1}{2\pi\hbar}\sum_{j}\int_{-\infty}^{\infty}\left\langle exp\left\{-i\vec{Q}\cdot\vec{R}_j(0)\right\} exp\left\{i\vec{Q}\cdot\vec{R}_{j}(t)\right\}\right\rangle e^{-i\omega t}dt \tag{2.16}$$

The coherent and incoherent dynamic structure factors are defined as follows:

$$S_{coh}(\vec{Q},\omega) = \frac{\sigma_{coh}}{N}\frac{1}{2\pi\hbar}\sum_{jj'}\int_{-\infty}^{\infty}\left\langle exp\left\{-i\vec{Q}\cdot\vec{R}_j(0)\right\} exp\left\{i\vec{Q}\cdot\vec{R}'_{j}(t)\right\}\right\rangle e^{-i\omega t}dt \tag{2.17}$$

$$S_{inc}(\vec{Q},\omega) = \frac{\sigma_{inc}}{N}\frac{1}{2\pi\hbar}\sum_{j}\int_{-\infty}^{\infty}\left\langle exp\left\{-i\vec{Q}\cdot\vec{R}_j(0)\right\} exp\left\{i\vec{Q}\cdot\vec{R}_{j}(t)\right\}\right\rangle e^{-i\omega t}dt \tag{2.18}$$

In the van Hove formalism, the dynamic structure factor is simply a Fourier transform from time to energy of the intermediate scattering function, shown below.

$$I_{coh}(\vec{Q},t) = \frac{\sigma_{coh}}{N}\sum_{jj'}\left\langle exp\left\{-i\vec{Q}\cdot\vec{R}_j(0)\right\} exp\left\{i\vec{Q}\cdot\vec{R}'_{j}(t)\right\}\right\rangle \tag{2.19}$$

$$I_{inc}(\vec{Q},t) = \frac{\sigma_{inc}}{N}\sum_{j}\left\langle exp\left\{-i\vec{Q}\cdot\vec{R}_j(0)\right\} exp\left\{i\vec{Q}\cdot\vec{R}_{j}(t)\right\}\right\rangle \tag{2.20}$$

The intermediate scattering function can also be transformed in space, resulting in a pair correlation function from the coherent scattering, and a self correlation function for the incoherent case.

$$G_{pair}(\vec{r},t) = \frac{1}{(2\pi)^3}\int_{-\infty}^{\infty} I_{coh}(\vec{Q},t)\cdot e^{-i\vec{Q}\cdot R}d\vec{Q} \tag{2.21}$$

$$G_{self}(\vec{r},t) = \frac{1}{(2\pi)^3}\int_{-\infty}^{\infty} I_{inc}(\vec{Q},t)\cdot e^{-i\vec{Q}\cdot R}d\vec{Q} \tag{2.22}$$

The G_{pair} gives the probability of finding any particle at position $\vec{R}$ at time t, with the condition that a particle is at the origin at time $t = 0$ (the two particles can also be the same particles). On the other hand, G_{self} gives the probability of finding the same particle which was at the origin at time $t = 0$ at position $\vec{R}$ at time t. In this interpretation G_{pair} includes G_{self}. This interpretation makes it clear that structure and collective dynamics manifest as coherent scattering, and that diffusion and local dynamics manifest as incoherent scattering.

2.3.2 Observation of coherent or incoherent scattering

The coherent or incoherent scattering can be suppressed by modifying the scattering properties of the sample (through deuteration), the instrumental technique used or the geometry of the sample. The dynamic structure factor will show a combination of signals, which may include an elastic and quasi-elastic signal, both centred around $\hbar\omega = 0$, as well as inelastic peaks centred at non-zero energy transfer. These can be seen in Figure 2.12. Depending on the sample and the instrumental geometry it may not be possible to observe all of these contributions to the dynamic structure factor simultaneously. Finally, by measuring a sample which is disordered, such as a hydrated powder or a solution coherent signals can be suppressed.

The different scattering behaviour of hydrogen (^1H) and its isotope deuterium (^2H) with neutrons becomes especially useful when dynamics are of interest. The incoherent and coherent scattering behaviour of neutrons is vastly different (see Table 2.5), allowing experimental systems to be designed to highlight certain types of dynamics. If one wishes to observe diffusion or other incoherent dynamics of a hydrogen rich system, it is possible to deuterate all molecules which are not of interest, decreasing the coherent signal by a factor of ~ 40, and observing the quasi-elastic broadening. If coherent dynamics are of interest, deuterating certain parts of the sample and observing the inelastic peaks provides a signal which comes primarily from the deuterated molecules.

This approach is often used for lipid bilayer studies. Through deuteration of the hydration water and the lipid tails, one can observe primarily head-group dynamics or by deuterating tails and observing the coherent signals information about collective motions such as bilayer undulation and bending may be observed [34, 35, 99, 121].

In the scope of this thesis, the incoherent dynamics of lipids in the bilayer were of interest. For all dynamic measurements, the hydration water was fully deuterated, suppressing the incoherent water signal. Finally the inelastic peaks were not of interest,

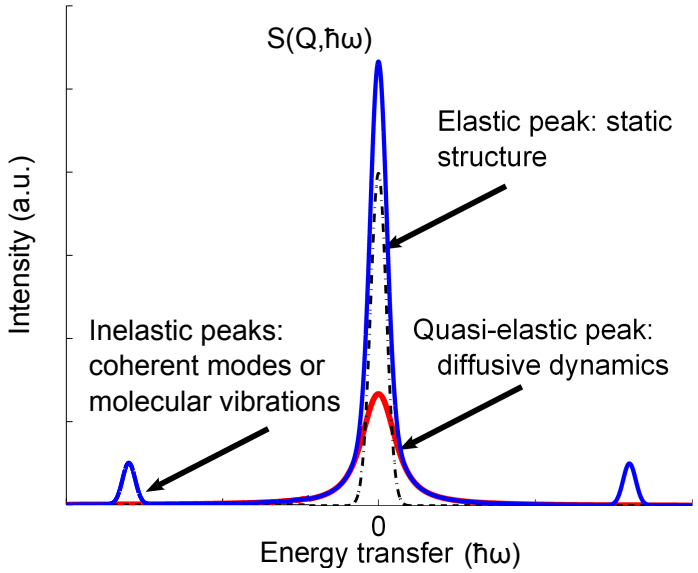

Figure 2.12: A general dynamic structure factor for a particular Q-value. Elastic contributions (no energy transfer) appear with a width defined by the instrumental energy resolution. A quasi-elastic signal, centred around the $\hbar\omega = 0$, arises from diffusive dynamical processes. Inelastic peaks arise from either coherent dynamical processes (phonons or magnons) or from lattice vibrations or excitations.

and the measurements made were all using instrumental geometry which captured primarily the elastic and quasi-elastic contributions to the scattering, around the $\delta E = 0$ in energy transfer. Such dynamics are revealed by neutron scattering and are further discussed below.

2.3.3 Quasi-elastic neutron scattering

The incoherent scattering arising from relaxing motions in the sample appears as a broadening of the elastic line, centred around $\Delta E = 0$ (as shown in Figure 2.12). To observe the inelastic scattering, an instrument must be capable of measuring the neutron energy before and after the scattering event. The energy of the incident neutron and of the scattered neutron are then compared. Experimentally this type of measurement is performed by using the spin-echo, backscattering or time-of-flight techniques. Spin-echo takes advantage of the polarizability of neutrons to observe changes in neutron spin before and after scattering events. This technique does not result in a measurement of the dynamic structure factor, but rather directly measures the intermediate scattering function. Spin-echo measurements access the longest relaxation times, with typical relaxations measured on the order of tens to hundreds of nanoseconds. Backscattering and time-of-flight measurements result in a

Table 2.5: Neutron incoherent and coherent scattering cross sections for common biological elements. [112]

Element	Z	$\sigma_{incoherent}$ (x10^{-24} cm^2)	$\sigma_{coherent}$ (x10^{-24} cm^2)
^{1}H	1	**80.27**	**-3.74**
D (^{2}H)	1	**2.05**	**6.67**
C	6	0.001	5.559
N	7	0.5	11.01
O	8	0.0008	4.232
P	15	0.005	3.307
S	16	0.007	1.0186

measurement of the dynamic structure factor. Experiments in this thesis in Chapter 3 used the backscattering and time-of-flight techniques, and will be explained in more detail in the following sections.

Both the backscattering and time-of-flight techniques measure the dynamic structure factor. An important feature of these measurements is the energy resolution. The energy resolution is related to the observable time-window through the Heisenberg uncertainty principle (Equation 2.23). The finer the energy resolution of an experiment, the broader the observable time-window. In general, the backscattering technique results in a high energy resolution ($\sim \mu eV$), giving access to a broad experimental time window ($\sim ns$), and thus access to dynamical processes with relaxation times in the nanosecond time-scale. Time-of-flight instruments have typical energy resolution of $10 - 100$ μeV, giving access to the dynamics with relaxation times between 1 and 100 ps. The set-up of backscattering and time-of-flight instruments can be tuned to observe particular dynamics.

$$\sigma_E \sigma_t = \frac{\hbar}{2} \tag{2.23}$$

Backscattering

A quasi-elastic neutron scattering instrument using the backscattering technique is generally tuned to produce an energy resolution in the μeV range, and thus allows for the measurement of dynamic processes in the ns time-range.

The backscattering technique relies on the scattering from a "perfect" crystal. If the crystal properties are well defined with a very low mosaicity, divergence of the incident beam is sharpened considerably at the backscattering angle ($\theta = 90^\circ$ *or* $2\theta = 180^\circ$) due to Bragg's law (see Figure 2.13). In backscattering quasi-elastic neutron scattering instruments, this property is often used twice, first on the monochromator, and second on the analyser. Backscattering measurements in this thesis were performed on the samples in Chapter 3 at the IN16 Backscattering spectrometer at the Institut Laue-Langevin in Grenoble, France.

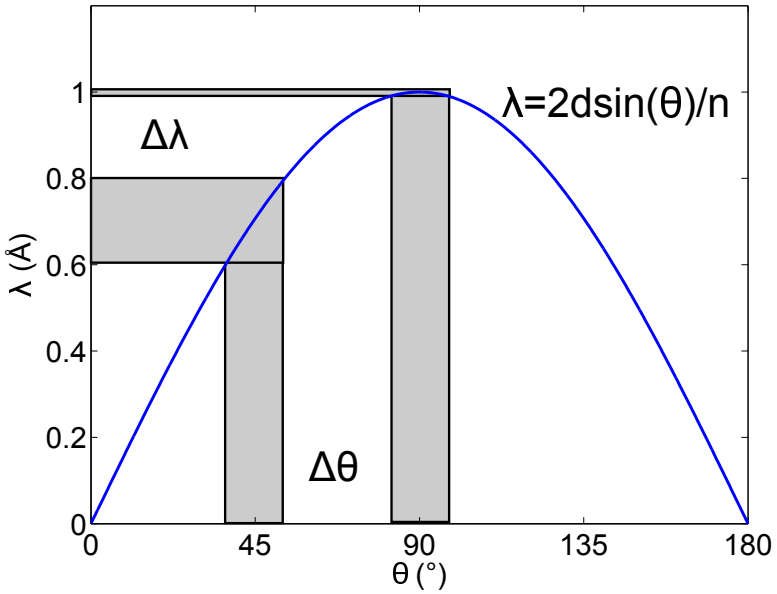

Figure 2.13: Divergence of wavelength at 45° and 90°. Backscattering condition from a "perfect" (infinitely small mosaicity) crystal sharpens any wavelength divergence.

The IN16 spectrometer was (IN16 has recently been upgraded to IN16b in 2014) located on a neutron guide which was aligned to a cold source (see diagram: Figure 2.14). A deflector redirects the primary wavelength of the neutron beam out of the neutron guide, which is then focused, and modified with a filter and chopper to remove neutrons with energies much larger or smaller than desired. A second deflector sends the neutrons towards the monochromator, this rotates with a frequency that defines the neutron pulses. Before the neutrons hit the monochromator they have a spread of energy. The Si(111) monochromator backscatters the neutrons, defining a very narrow energy spread. The neutrons then scatter off of the sample and are sent towards an array of carefully aligned Si(111) crystals, which act as a second backscattering crystal. The neutrons pass through the crystal once again, and are detected. In this set-up, with a stationary monochromator, the instrument is acting more like a (very expensive) diffractometer, observing only the elastic scattering. By attaching the monochromator to a Doppler-drive, a spread of incoming energy is achieved. Since the neutrons are moving at a velocity of ∼1000 m/s, and the Doppler-drive's maximum velocity is closer to ∼1 m/s, each packet of neutrons will see a slightly different monochromator d-spacing, as the monochromator moves towards or away from the incoming neutrons. Thus each packet has an energy, and the scattered neutrons are binned according to their respective energy changes.

Changing the chopper speed can allow access to narrower or broader energy resolutions, defined in Equation 2.24, with E_o=2.08 meV, the characteristic energy of a Si(111) crystal. The incident energy is defined by the monochromator, when it

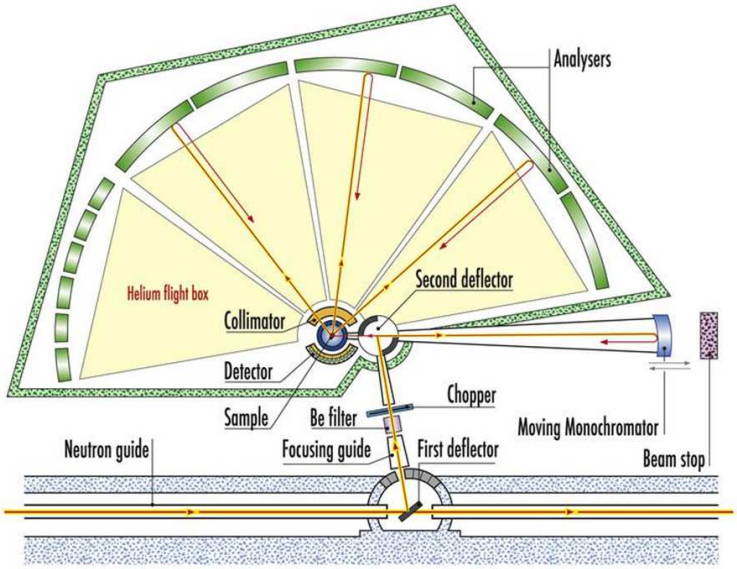

Figure 2.14: The backscattering spectrometer IN16. Diagram from ILL.

is stationary, $E_i = E_f$, and when the monochromator is being driven by the Doppler $E_i = \frac{m_n}{2}(v_o + v_{mono})^2$, with v_o the incoming neutron velocity, and v_m the instantaneous velocity of the monochromator while the neutrons backscatter.

$$\Delta E = E_m - E_o = 2E_o\frac{v_m}{v_o} + E_o\left(\frac{v_m}{v_o}\right)^2 \tag{2.24}$$

Time of flight

A time-of-flight spectrometer generally accesses a lower energy resolution than the backscattering spectrometer, ranging from 10 to 100 μeV. This relates to a time-window on the order of 10 to 100 ps. The velocity with which a neutron travels is defined by its energy through $E_k = \frac{1}{2}mv^2$. A time-of-flight spectrometer determines the neutron energy by calculation of the time the neutron travels a known distance. Typical instrument designs rely on a series of choppers (rotating discs with alternating absorbing and transmitting portions) to select a neutron bunch and define the incident wavelength spread. The rotation ratios between choppers at different locations along the neutron path define the wavelength and the pulse-width of the incoming packet.

A simplified calculation of the energy broadening from the sample to detector can be made by calculating the first and last neutron of a bunch to arrive at the detector. In this simplification, we make the assumption that the incident neutron beam was monochromatic, with every neutron possessing the same energy. This monochromatic neutron bunch scatters with our sample, and a short time later arrives at the detector, a distance d_{SD} away from the scattering site. The first neutron arrives after a time t_o,

and the last neutron arrives after a time t. The difference between the two times is defined as $\Delta t = t - t_o$. The spread in energy can be defined by spread in flight-times, as in Equation 2.26.

$$\Delta E = \hbar\Delta\omega = \frac{1}{2}m_n\left(\Delta v\right)^2 = \frac{1}{2}m_n d_{SD}^2\left(\Delta\frac{1}{t_o} - \frac{1}{t}\right)^2 \tag{2.25}$$

$$\Delta E = \frac{1}{2}m_n d_{SD}^2\left(\Delta\frac{\Delta t}{t_o^2 + \Delta t t_o}\right)^2 \tag{2.26}$$

In Chapter 3, experiments were done with the time-of-flight spectrometer TOFTOF at the FRMII reactor at Heinz Maier-Leibnitz Forschungszentrum in Munich, Germany. This spectrometer uses a series of choppers to define the energy spread of the neutron bunch, and thus the energy resolution of the measurement. A schematic of this spectrometer is shown in Figure 2.15. TOFTOF is named due to the two time-of-flight (TOF) measurements which are done on a neutron bunch. The first TOF is the monochromation of the incident beam, which takes place before the sample, and the second TOF which describes the time it takes the neutrons to travel from the sample to the detector.

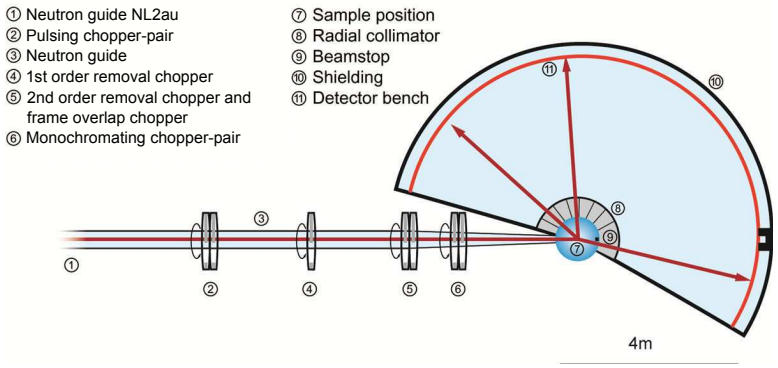

Figure 2.15: Schematic of the time-of-flight spectrometer TOFTOF at the Heinz Maier-Leibnitz Forschungszentrum in Munich, Germany.

The rotation speed of the choppers allows one to select the incoming wavelength, which defines the observable energy and Q-range (shown in Figure 2.16).

2.4 Sample Preparation

The samples used in all experiments were prepared by dissolving all materials into a solvent and depositing this lipid/protein/solvent mixture onto substrates with an artist's airbrush. In all cases, the required amount of lipid, cholesterol, or peptide was measured either directly by weight, or by dissolving a weighed amount into a solvent at a known volume, then distributing out aliquots by volume.

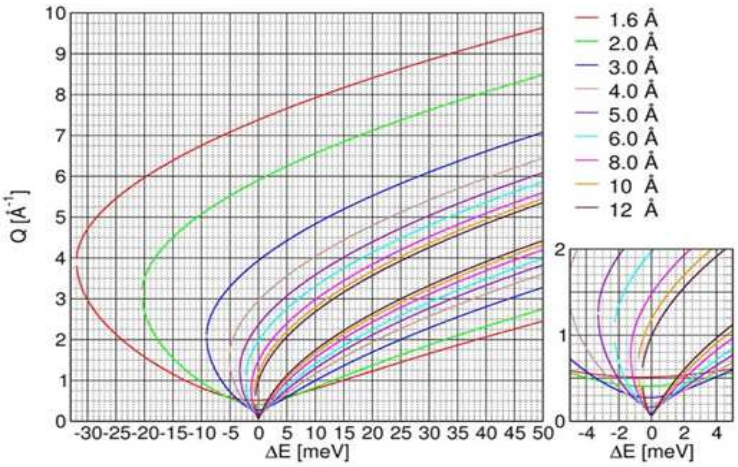

Figure 2.16: The range of available scattering parameters for TOFTOF.

For samples containing peptide, the first step was to dissolve the peptide into trifluoroacetic acid (TFA), at a concentration of ∼4 mg/mL. TFA has been shown to prevent pre-aggregation of monomers before interaction with the membrane [122]. The TFA was then evaporated with a stream of Argon for ∼10 min.

All components were dissolved into a 4:1 volume ratio of chloroform:methanol in a concentration of 15 mg/mL, and combined to the required ratio for each sample. The dissolved mixture was sealed then sonicated in a water bath sonicator for ∼2 min, then vortexed to ensure good mixing. The mixture was then introduced to the reservoir of a clean artist's airbrush (between samples excess solvent was sprayed through to clean any residual material). The mixture was then sprayed slowly onto sample substrates (Si-111 wafers in most cases). After sample deposition was finished, the samples were placed into a vacuum desiccator at room temperature for a minimum of 12 h to allow all remaining solvent to evaporate.

Samples were optimized for each of the three types of experiments in this thesis (Figure 2.17). A typical sample for use in a quasi-elastic neutron setup had ∼100 mg of sample material, ∼10 mg for neutron diffraction and ∼1 mg for X-ray diffraction. The size and the amount of sample material was chosen based on the dimensions of the incoming beam, and the type of scattering which must be detected. The size of the beam for neutron scattering is generally larger with considerably lower flux than found in X-ray setups. For a quasi-elastic experiment, instead of looking for high-intensity peaks formed by constructive interference, one observes the incoherent scattering off of the main peak spread over various angles and time-channels. Thus it is necessary to use more sample material for a QENS measurement as compared to a diffraction measurement.

This method of sample preparation results in well-oriented lipid bilayer samples (average mosaicity between 1° and 5°) [77, 123, 124, 125]. Based on the mass of

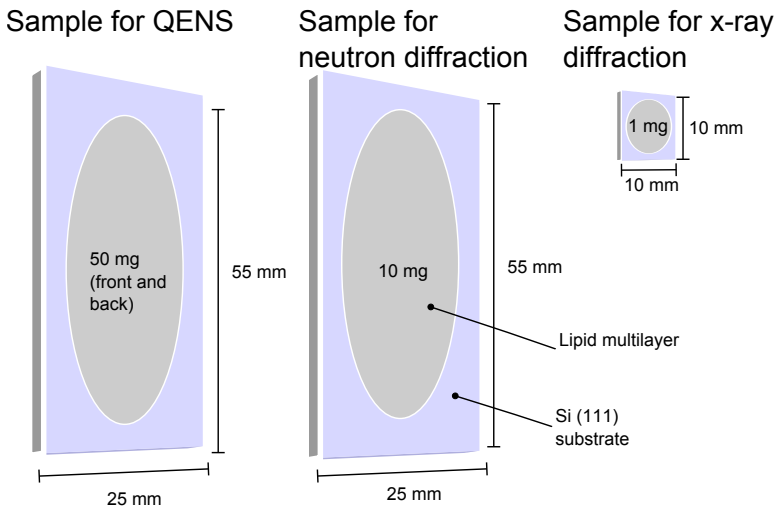

Figure 2.17: Lipid bilayer multilayer samples on Si(111). Each sample was optimized for the type of experiment (a double sided sample with a total of 100 mg for QENS: left, a 10 mg sample for neutron diffraction: middle and a 1 mg sample for X-ray diffraction: right), but prepared using the same process (as described in text).

sample material, the area of the wafer covered by sample and the measured d-spacing, an estimate can be made of the number of lipid bilayer stacks on the sample. For the samples described in this thesis, $\sim$10 000-50 000 bilayers exist on each sample substrate, providing sufficient repeated layers to obtain a scattering signal.

3 Amyloid-β fragment 22-40 in lipid membranes

A clear understanding of membrane dynamics and the changes which occur in the presence of the neurotoxic amyloid-β peptide is necessary to better understand the origin of the symptoms associated with Alzheimer's disease. In particular, the experiments which follow test the effect of the lipid sized 22-40 peptide fragment, with similar size and hydrophobicity to the bilayer lipids which make up the majority of the sample.

Fragments of the full-length amyloid-β peptide are known to exist *in situ*, and from a practical point of view, using part of the peptide which is thought to intercalate into the membrane without including the hydrogen rich 1-21 residues reduces significantly the scattering signal coming from the peptide itself, allowing a cleaner measurement of the lipid dynamics. A molecular diagram is shown in Figure 3.1.

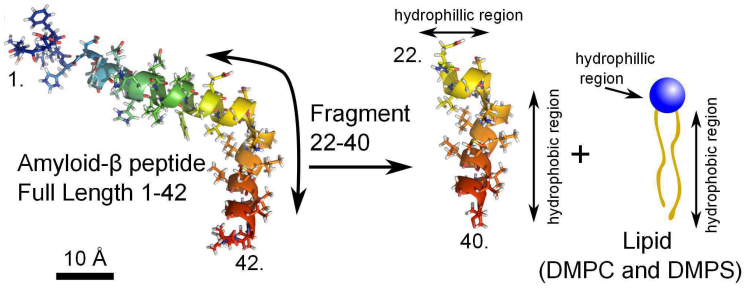

Figure 3.1: The full length (1-42 amino acids) peptide, and the fragment (22-40 amino acids) used in the following experiments. Samples were made with a DMPC/DMPS mixture and a 1.5 mol% of amyloid-β_{22-40}. Peptide structures were presented using the PyMol graphics program [126].

3.1 Experimental results

In this chapter, experiments on a multi-component lipid membrane are presented. The effect of a small amount of amyloid-β peptide on a model lipid bilayer are tested through a pair of complementary experiments.

- Structural changes in the lipid bilayer are observed via neutron diffraction

Table 3.1: The composition of the samples used for the structural investigations using neutron diffraction.

	DMPC (mol%)	DMPS (mol%)	$A\beta_{22-40}$ pro (mol%)	$A\beta_{22-40}$ deu (mol%)
lipid sample	92	8	-	-
$A\beta_{protonated}$ sample	90.6	7.9	1.5	-
$A\beta_{deuterated}$ sample	90.6	7.9	-	1.5

experiments, using a deuterium labelled peptide fragment to determine the location and structural changes induced by the peptide's presence (Section 3.1.1)

- Dynamical changes of bilayer lipids observed with quasi-elastic neutron scattering experiments, determining diffusion coefficients for a variety of dynamical processes in the lipid bilayer (Section 3.1.2)

Lipid bilayer samples were prepared using the method described in Section 2.4. For each experiment in this section, the lipid ratio of 92:8 mol% DMPC:DMPS was used. DMPC and DMPS are lipids consisting of saturated 14-carbon tails. The difference between the two lipids is the head-group; the PC in DMPC is a neutrally charged phosphatidyl-choline group, and the PS in DMPS is a negatively charged phosphatidyl-serine. Lipid membranes in biological systems possess charged lipids, and for interaction between peptides and lipids, it is necessary for the membrane lipids to contain a slight charge. Additionally, for samples containing peptide, a ratio of 1.5 mol% of peptide to lipid was used.

3.1.1 Location of deuterium tagged amyloid-β in a lipid bilayer

The primarily hydrophobic amyloid-β_{25-35} fragment intercalates into the membrane. Up until this point, no experimental evidence has been presented showing that the lipid sized amyloid-β_{22-40} interacts with the membrane, but due to hydrophobic arguments it has been hypothesized that this peptide will also intercalate [45]. To determine the location of the amyloid-β_{22-40} peptide fragment in the lipid bilayer, and to observe any structural changes the peptide's presence may induce, an experiment involving neutron diffraction was performed. This experiment was performed at the diffractometer MIRA at the FRM-II reactor in Munich, Germany (described in Section 2.2.2).

The samples which were measured are listed in Table 3.1. There were three samples prepared using the procedure described in Section 2.4, with 10 mg of sample deposited onto a single-sided silicon wafer. One control sample exists, containing only lipids. The other two samples contain amyloid-β_{22-40} at 1.5 mol%. The deuterated sample and the protonated sample are identical, except for the labelling of two Valine amino acids (number 39 and 40) with eight deuterium atoms in the place of hydrogen. This creates a sixteen deuterium atom label on one end of the peptide fragment, shown in Figure 3.2. The protonated and deuterated peptide fragments will result in identical

bilayer structure, with a signal difference due to the tagged label, making localization possible.

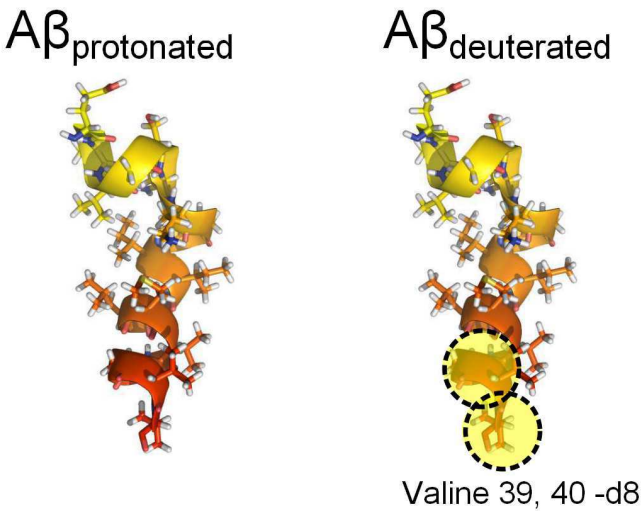

Figure 3.2: The amyloid-β_{22-40} peptide (left) and deuterated (right) version, with deuterated amino acids labelled by dotted circles and highlighted.

The samples were mounted in a goniometer and sealed in a temperature regulated humidity chamber, held at 40°C, and humidity regulated with a saturated K_2SO_4 salt solution (∼98% relative humidity), as described in Section 5.2.2. All samples were given at least 8 hours to equilibrate before a scan was started. Each sample was scanned three times, with different $D_2O : H_2O$ ratios (8%, 20% and 50%). These variable $D_2O : H_2O$ ratio measurements will be used to solve the phase problem when doing the Fourier reconstruction in the following section.

The procedure in Section 2.2 was followed, first by summing up multiple scans to increase statistics, then by fitting each of the summed peaks for the three samples in question (shown in Figure 3.3). An exemplary data set (lipid sample) is shown in Figure 3.4. For each peak, a single Gaussian and a linear background was used for fitting. Notice the number of counts for each additional Bragg order (n). By the sixth order, the signal was too weak to be observed in all samples, even for long counting times.

The position of all peaks was used to calculate the d-spacing of each bilayer. The lipid sample had a d-spacing of ∼50.2 Å, the protonated peptide ∼52.1 Å and the deuterated peptide sample ∼52.4 Å. An inconsistency in d-spacing between the three $D_2O : H_2O$ ratios was observed, which was unexpected. This ±1 Å inconsistency can be explained by the sensitivity to humidity. In the 98% relative humidity region, small variations result in drastic changes. The intensities for each peak of each sample were then plotted against the D_2O percentage, to determine the Fourier phase coefficients.

Only the 8% D_2O will be analysed. At this ratio neutron scattering length density

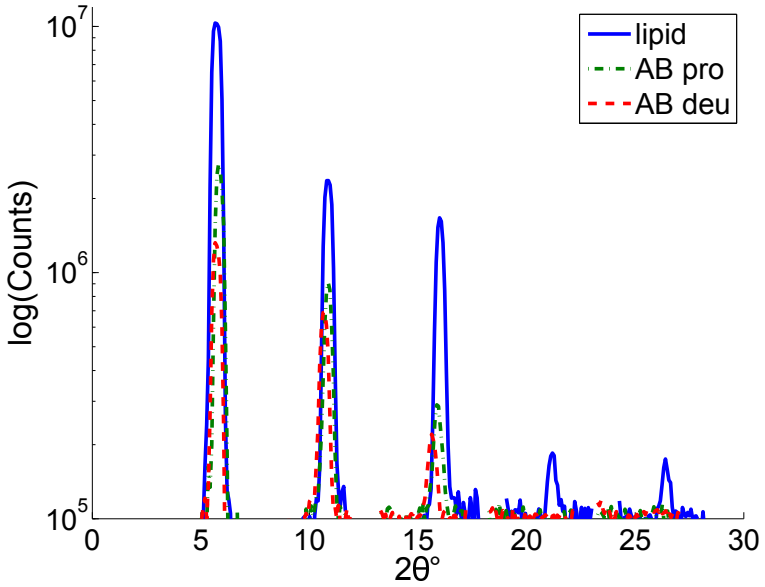

Figure 3.3: The first five Bragg reflections from the lipid (blue), A$\beta_{protonated}$ (green) and A$\beta_{deuterated}$ (red) samples. To plot these together, it was necessary to display the data logarithmically.

of water is zero, which provides the most sensitivity to observe the deuterated label.

The Fourier phase coefficients, as well as the intensities from the Gaussian fitting were then used in Equation 2.8 to recreate the scattering length density.

The reconstructed neutron scattering length density plots were then scaled (a general scaling was made with the total neutron scattering length density of the unit cell), and plotted together to compare the reconstructed densities. In Figure 3.5, the pure lipid, and sample with protonated amyloid-β have been plotted together. The lipid neutron scattering length density appears as expected, very similar to a DMPC bilayer in the fluid phase [83]. The addition of the peptide results in a smoothing-out of the lipid tails, and a lowering of the head-group intensity. The difference between the two samples containing amyloid-β results in a maximum centred at ∼5 Å in the deuterated sample. There is also a small contribution in the head-group region of the bilayer, which could be assigned to peptides residing on the surface of the membrane. The deuterated label is located on the 39 and 40 Valine atoms. This section of the peptide has been suspected to interact with the lipid tails, due to the average hydrophobicity of the amino-acids in this section [45].

With evidence that the peptide interacts with the lipid bilayer, and changes the bilayer structure, the next step was to check if the peptide would change the dynamics of the lipids in the bilayer.

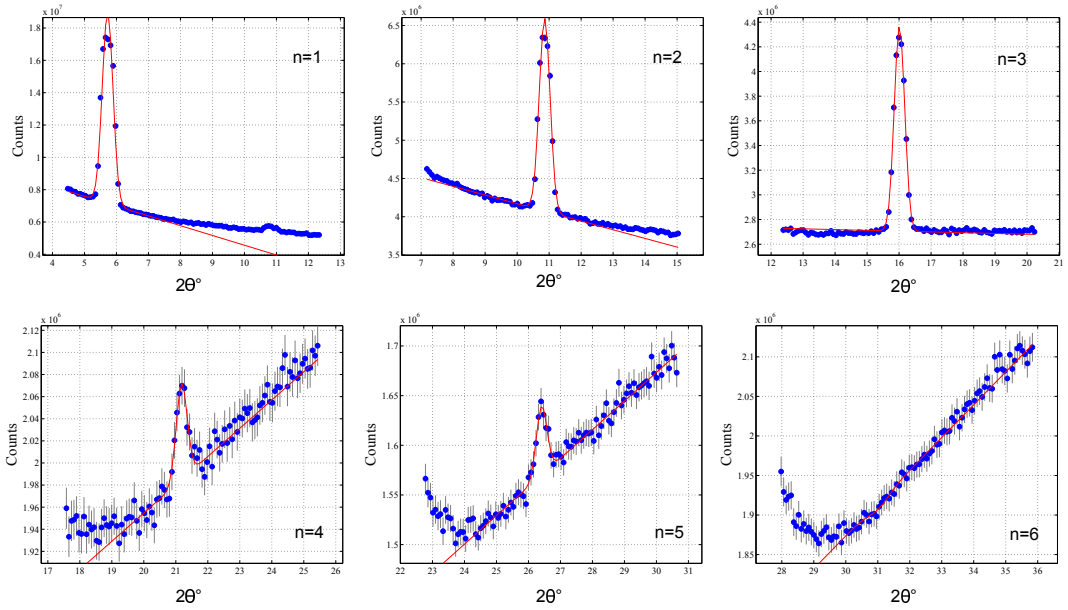

Figure 3.4: The fitted Bragg peaks for the first six orders of the lipid sample. The sixth order (bottom right) was not fittable, due to a weak peak signal. Typically 5 peaks are expected for bio-membranes observed with neutron scattering, due to mosaicity of the sample and background noise.

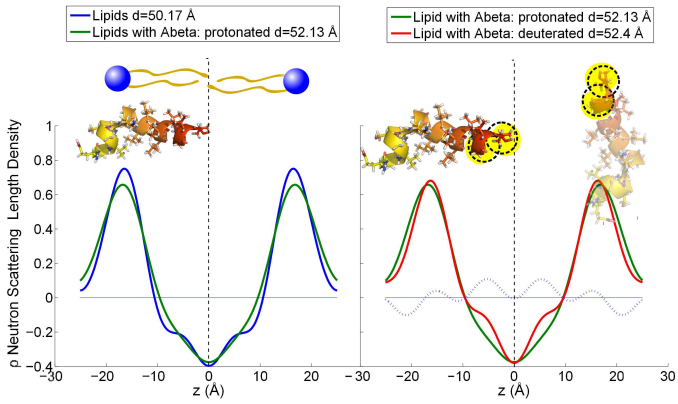

Figure 3.5: The amyloid-β_{22-40} peptide (left) and deuterated (right) version, with deuterated amino acids labelled by dotted circles.

3.1.2 Lipid dynamics perturbed by amyloid-β peptide fragment 22-40

Structural evidence showing that the amyloid-β_{22-40} fragment enters into the lipid bilayer and changes the *d*-spacing spurred the next step in the investigations, to see

the effect of the peptide on the dynamics of lipids in the bilayer.

To observe the dynamical changes, a series of quasi-elastic neutron scattering (QENS) experiments were performed. Refer to Section 2.3 for a brief experimental introduction to this technique.

The silicon substrate with multilayer lipid sample (described in Section 2.4) is mounted into an aluminum cylindrical chamber [127]. The substrate sits in a Teflon holder. On either side of the sample are troughs which were filled with a K_2SO_4:D_2O saturated salt solution, and a small tissue to increase surface area and speed up equilibration. The chambers are sealed airtight with Teflon, and the sample is given a minimum of 12 h to reach a saturation equilibrium. Before and after measurement, the sealed container with sample was weighed, to ensure the seal was leak-proof and no water has evaporated from the cylinder.

Because the lipid bilayers are oriented on the silicon substrate, it is possible to orient the sample with respect to the incoming neutron beam, allowing for anisotropic measurements of the in-plane and out-of-plane lipid dynamics.

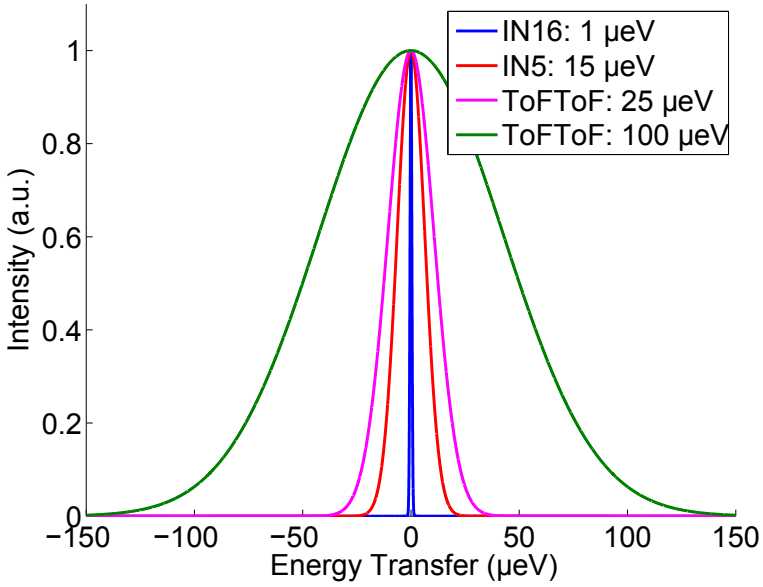

Figure 3.6: A comparison between the elastic energy resolution of the four energy resolutions used in this work. The energy resolutions span from 1 μeV (FWHM: IN16) to 100 μeV (FWHM: ToFToF). More information on the instrumental characteristics can be found in Table 3.2

To access a broad dynamic range, multiple measurements of the same sample at different energy resolution were taken. Three spectrometers (two time-of-flight and one backscattering) were used, allowing observation of relaxations from the picosecond to nanosecond range. The instrumental parameters of each measurement are listed in Table 3.2.

Spectrometer	ΔE (μeV)	λ(Å)	Q_{range} (Å^{-1})	t_{window} (ps)
IN16 (ILL)	1	6.3	0.6-1.9	400-1240
IN5 (ILL)	15	10	0.3-1.1	10-83
ToFToF (FRM-II)	25	8	0.5-1.3	4-50
ToFToF (FRM-II)	100	5	0.7-1.7	1-12.4

Table 3.2: Spectrometers used and their respective elastic energy resolution (ΔE), wavelength (λ), Q-range and resolution time (t_{window}). Conversion from energy to time was calculated using $t_{resolution}$=1.24 μeV·ns/ΔE_{FWHM} [128]. An estimate of the lower limit of the time window was given by the dynamic range, determined from the spectrometer's characteristics, the upper limit is estimated from the instrumental resolution, characterized with a vanadium standard.

The normalized elastic resolutions of the four instrumental setups which were used are plotted in Figure 3.6.

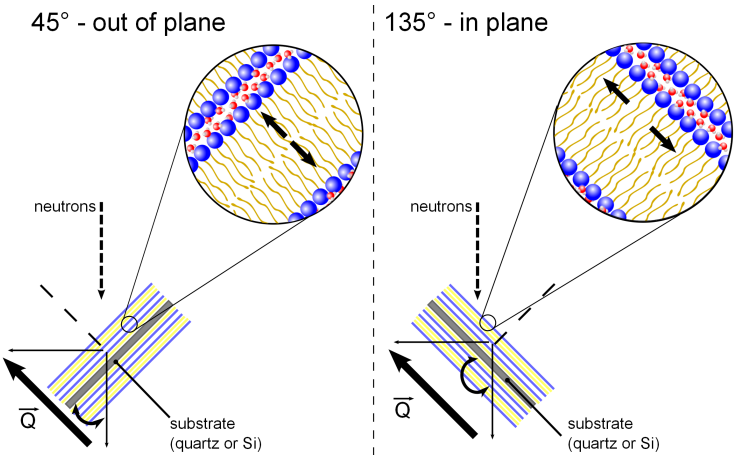

Figure 3.7: An oriented sample allows for measurements of both the out-of-plane (45°) and in-plane (135°) scattering geometries. Neutrons, represented by the dashed arrow travel towards the sample and are scattered with the momentum transfer $\vec{Q}$ (thick arrow), defined by the vector subtraction $\vec{k_f} - \vec{k_i}$.

If the sample scatters completely elastically the signal which is observed is simply a Dirac-delta peak convoluted with the Gaussian energy resolution, resulting in a Gaussian shaped signal. On the other hand, if some quasi-elastic dynamical processes occur in the sample, a broadening of the signal will be observed. If the sample undergoes more than one dynamical process, multiple broadening forms may be present. For this reason, the energy resolution must be selected so that the effect of a range of dynamic processes may be observed. A process which is too slow will have a very narrow

line-shape, and will be indistinguishable from the elastic peak, whereas a process which is too fast with have a line-shape that is much broader, and will only give rise to a flat background signal.

The data from each of the instruments is first reduced and treated in LAMP [129]. This includes normalization to monitor counts, shifting data to ensure agreement between energy transfer channels and calculation of the channel and angle of each detector pixel to energy transfer and scattering vector, $\vec{q}$. To improve statistics, energy and scattering vector channels are rebinned. The steps of this process are presented in a flow diagram in Figure 3.8.

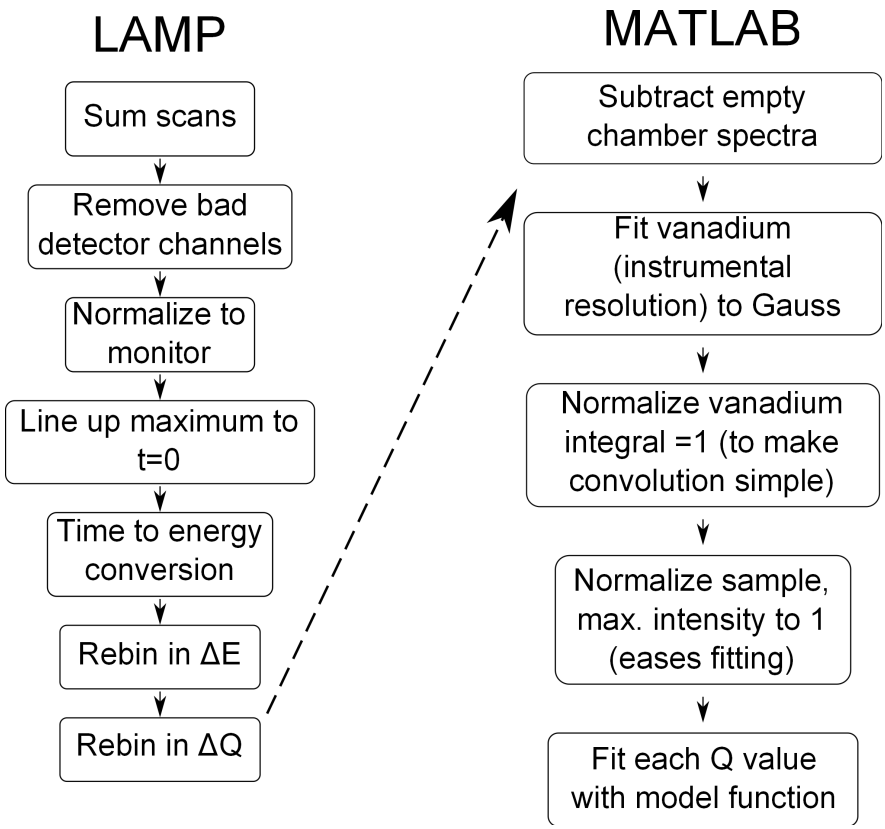

Figure 3.8: The data reduction and treatment steps presented in a flow diagram. The left column procedure is carried out in LAMP, while the right column is performed in MATLAB.

At this point in the analysis, each measurement can be represented by a two dimensional intensity map, represented by the measured structure factor $S_{measured}$ (Q,$\hbar\omega$). Figure 3.9 shows the same sample (DMPC/DMPS lipid sample) using identical conditions (135° and 30°C) for the four instrumental resolutions. In this figure, the typical quasi-elastic broadening of each sample is observed, corresponding to a lowering of intensity around $\Delta E = 0$ with increasing Q, with intensity being redistributed

outwards, towards positive or negative energy transfer.

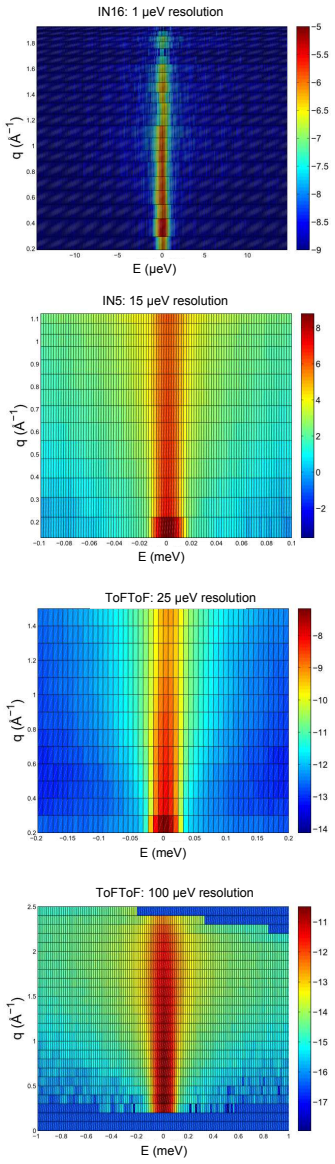

Figure 3.9: The measured structure factor $S_{measured}(Q, \hbar\omega)$ for the four instrumental resolutions used (from top to bottom: 1 μeV: IN16, 15 μeV: IN5, 25 μeV: ToFToF and 100 μeV: ToFToF.) Colour intensity presents data logarithmically.

It was mentioned previously (Section 2.3.1) that the structure factor may be represented as an intermediate scattering function, through a Fourier transformation from the energy (frequency) domain to the time domain. This treatment is a good starting point to get a physical sense of what range of dynamic processes can be

observed, and a general feel for the way the different instrumental resolutions relate to one another. This approach is further developed in Section 3.1.2 below. The accessible time-window and Q-range of each measurement is listed in Table 3.2 and shown graphically in Figure 3.10.

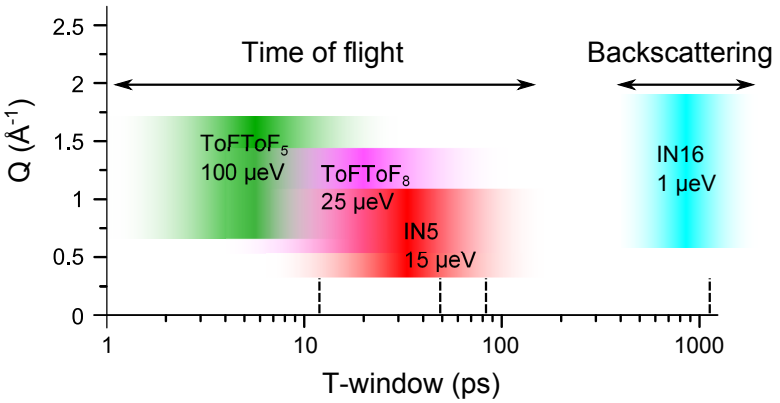

Figure 3.10: Accessible time-window and Q-range of each instrument used. ToFToF measurements are represented in green (100 μeV) and pink (25 μeV), IN5 in red (15 μeV) and IN16 in blue (1 μeV). The time-of-flight instruments had access to a time-window spanning from ∼1-100 ps, whereas the backscattering spectrometer allowed access a range of ∼0.4-1.2 ns

Due to differences in the geometry of each spectrometer, and the changes made to the incoming neutron beam to prepare the beam-packet, the same Q-range was not measured for every instrument. However, all instrumental resolutions measured have data for the Q=1 $Å^{-1}$, and thus the data from this Q-value could be Fourier transformed and plotted together.

The data was Fourier transformed using the *Fourier Transform* package in DAVE [130]. The data is further treated by dividing by the instrumental resolution function of each instrument, as determined by a scan of a vanadium standard. The data points approaching the longest times begin to fluctuate and the respective uncertainties of these points becomes very large, an artefact of the Fourier transform. A threshold value of uncertainty was selected as the cut-off for each instrumental resolution, points with uncertainties larger than the threshold were not included in the graph. The data was also scaled such that all points fall smoothly together. The lowest resolution (fastest time-window) measurement was chosen as the most accurate, and the remaining data sets were rescaled to agree with this data set. This is necessary to account for variations in instrumental geometry. The multiplication scaling factors ranged from 0.75 to 1.25. The combined intermediate scattering function of the four instrumental resolutions are plotted in Figure 3.11.

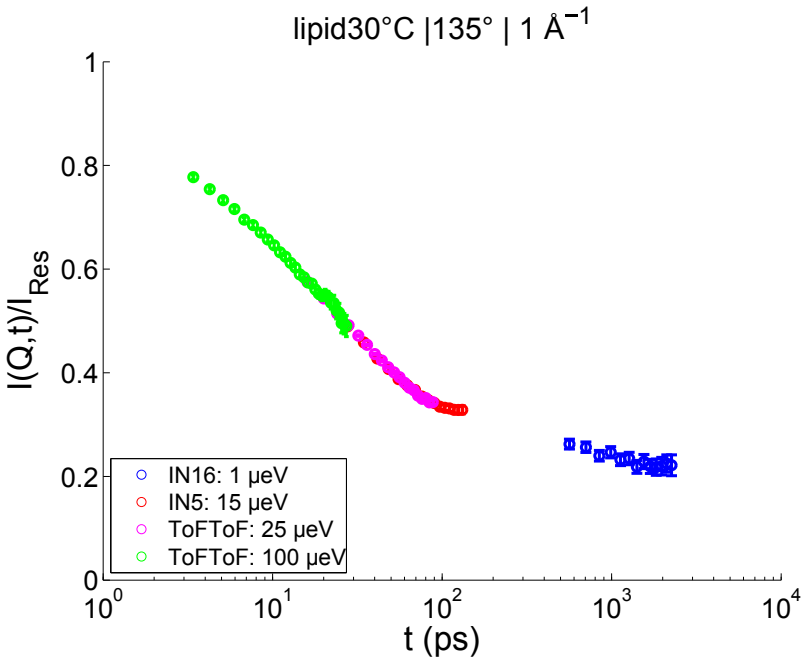

Figure 3.11: The combined intermediate scattering function of all four measurements of the 135°, 30°C lipid sample. ToFToF measurements are represented in green (100 μeV) and pink (25 μeV), IN5 in red (15 μeV) and IN16 in blue (1 μeV).

Building a dynamic model

Up until this point, no assumptions have been made about the nature of the dynamics which are being observed. To describe the data, it is necessary to select a reasonable model at this stage.

There is no universally accepted model to describe the dynamic structure factor representing the motions of bilayer lipids. Most fitting models are constructed from a combination of the functions listed below.

1. Dirac-delta: arising from stationary particles (and particles which are so slow that they appear stationary in the time-window of the spectrometer)
2. Constant background: arising from particles moving too fast to be observed at a particular spectrometer time-window
3. Lorentzian: arising from particles moving in a diffusive manner
4. Gaussian: arising from particles moving in an unrestricted ballistic or flow-like manner

5. Kohlrausch-Williams-Watts (KWW a.k.a. stretched exponential): arising from particles which exhibit a range of diffusive motions, rather than one distinct relaxation

$$S_{Lorz}(Q,\hbar\omega) = A(Q)\cdot\delta(\omega) + (1-A(Q))\frac{1}{\pi}\frac{\Gamma/2}{(\Gamma/2)^2+(\hbar\omega)^2} + bg \quad (3.1)$$

$$S_{Gauss}(Q,\hbar\omega) = A(Q)\cdot\delta(\omega) + (1-A(Q))\frac{1}{\sigma\sqrt{2\pi}}exp\left[\frac{-\omega^2}{2\sigma^2}\right] + bg \quad (3.2)$$

$$S_{KWW}(Q,\hbar\omega) = A(Q)\cdot\delta(\omega) + (1-A(Q))FFT_{\omega\leftrightarrow t}\left(exp\left[(\frac{-t}{\tau})^{\beta}\right]\right) + bg \quad (3.3)$$

Where:

Γ:	is the Lorentzian FWHM.
σ:	is the Gaussian width ($FWHM_{Gauss} = 2\sqrt{2ln(2)}\sigma$)
τ:	is the relaxation time ($\Gamma = \hbar/\tau$)
β:	is the stretching coefficient
$FFT_{\omega\leftrightarrow t}$:	represents the fast Fourier transform from frequency to time

It is commonly accepted that lipids exhibit Brownian diffusion over length scales larger than the lipid nearest neighbour distance, modelled by a combination of the Dirac-delta, Lorentzian and background functions [34, 35, 99, 121]. The line-width of the Lorentzian with respect to Q is then plotted. If the line-width shows a Q^2 dependence, a Brownian diffusion can be modelled and a diffusion coefficient may be extracted from the data. Recently, some publications have modelled dynamics Gaussian fitting models to describe a collective flow-like motion of lipids over short [36] and long length scales [43, 131], with a linear dependence of the line-width on Q, providing a mean lipid velocity. There have also been publications which use the KWW function to model lipid tail dynamics, using the stretching factor β to account for the range of motions along the tails, although the physical interpretation of this model is not straightforward [132].

The most recent approach to modelling lipid dynamics involves two or more Lorentzian functions, relating to dynamic processes separated by at least one order of magnitude [31, 32]. The slowest of the relaxations (ns time-scale) fits well to a Brownian diffusion process, whereas the fast (ps time-scale) Lorentzian functions deviate from the Brownian model. Deviations (offsets resulting in non-zero line-width at Q=0) can be interpreted as restricted motions, such as the motion of the lipid tails (confined by the tail itself), or head-groups (restricted by neighbouring lipids). Deviations at large Q can be interpreted as a jump-like diffusion, with lipids making rapid jumps to vacant neighbouring sites.

For the IN16 backscattering measurement (with energy resolution of 1 μeV), three test fitting functions were constructed using an elastic contribution (Dirac-delta), a

constant background, and one of either a Lorentzian (Eq. 3.1), Gaussian (Eq. 3.2) or KWW/stretched exponential (Eq. 3.3). These fitting attempts are shown in Figure 3.12. An indicator of the quality of the fit is the calculated χ^2 value, a sum of the difference between each point and the fit. In general, the Gaussian function resulted in the largest χ^2, and the Lorentzian and KWW fit profiles were close, with KWW always a touch better. For the remainder of the analysis, a model consisting only of Lorentzians was used, as the fits are comparable, the Lorentzian fit function contains one less fitting parameter and the physical explanation of a Lorentzian fit is much more straightforward than the KWW model.

Working first with the combined intermediate scattering function shown in Figure 3.11, and assuming that the time-range used allows us to observe all dynamics (no background necessary), a single process can be described by the Fourier transform of Equation 3.1, which transforms to an exponential decay function in the time-domain: shown in Equation 3.4.

$$I_i = [A_i(Q) + (1 - A_i(Q))exp(-t/\tau_i)] \tag{3.4}$$

An attempt was made to fit the data first with a single exponential, then with two and finally with three. The product of three exponentials was necessary to provide a reasonable fit. A sample of these fits for the lipid sample at 30°C and 135° is shown in Figure 3.13.

It is clear from Figure 3.13 that three relaxation processes occurring with well separated relaxation times can be observed in our data. The relaxation times of these processes vary with temperature, and with the presence of amyloid-β peptide, but no further analysis was done on the combined intermediate scattering function. Instead, with the knowledge of the general relaxation times, more detailed Q-dependent analysis could be performed on the dynamic structure factor. These relaxation times are ∼1 ns, ∼20 ps and ∼5 ps. By comparing these relaxations to literature values, these processes were assigned to different aspects of lipid motions, in particular, whole lipid molecule Brownian diffusion occurring in the nanosecond range, local lipid dynamics associated with rotation, ∼17 ps [35], chain kink diffusion ∼20 ps [121] and the dynamics of hydrogen atoms found in methylene and methyl groups of the lipid chains, ∼3-8 ps [133].

Thus a general intermediate structure factor capturing all three relaxations can be defined in Equation 3.5. With the indicies 1-3 defining the three relaxations from slowest (τ_1 ∼1 ns) to the fastest (τ_3 ∼5 ps).

$$\begin{aligned} I_{theo}(\vec{Q},t) &= I_1(\vec{Q},t) \cdot I_2(\vec{Q},t) \cdot I_3(\vec{Q},t) \\ &\text{with} \\ I_i(\vec{Q},t) &= [A_i + (1 - A_i)exp(-t/\tau_i)] \end{aligned} \tag{3.5}$$

This general intermediate structure factor can then be expressed as a dynamic

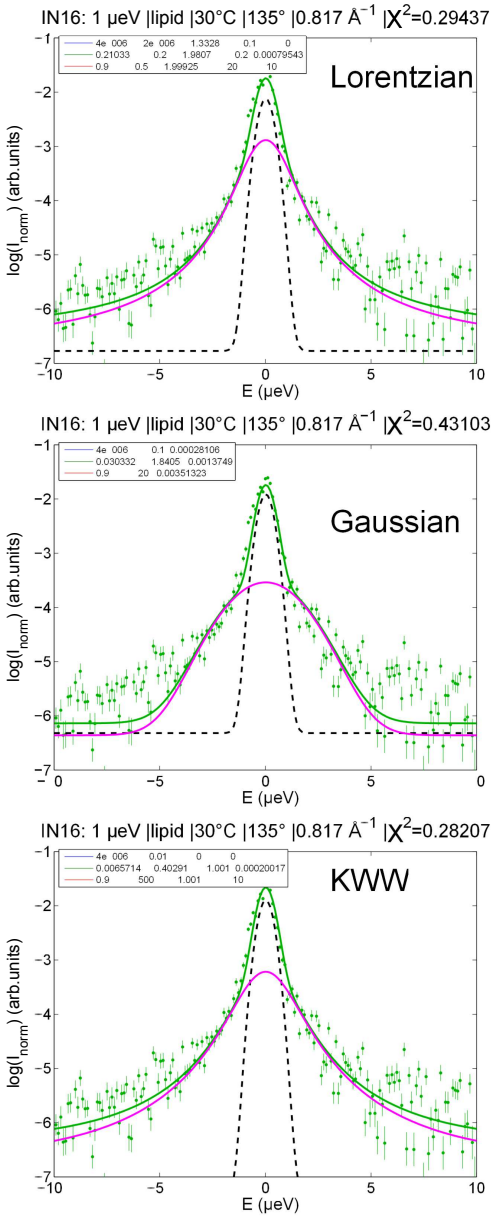

Figure 3.12: Potential fitting functions for the lipid sample at 30°C measurement by the IN16 backscattering spectrometer. Top: fit using Lorentzian based model in Equation 3.1. Middle: fit using Gaussian based model in Equation 3.2. Bottom: fit using Kohlrausch-Williams-Watts or stretched exponential based model in Equation 3.3.

structure factor S(Q,$\hbar\omega$) through a Fourier transformation. It is important to observe that multiplication in the time-domain is converted to convolution in the energy domain

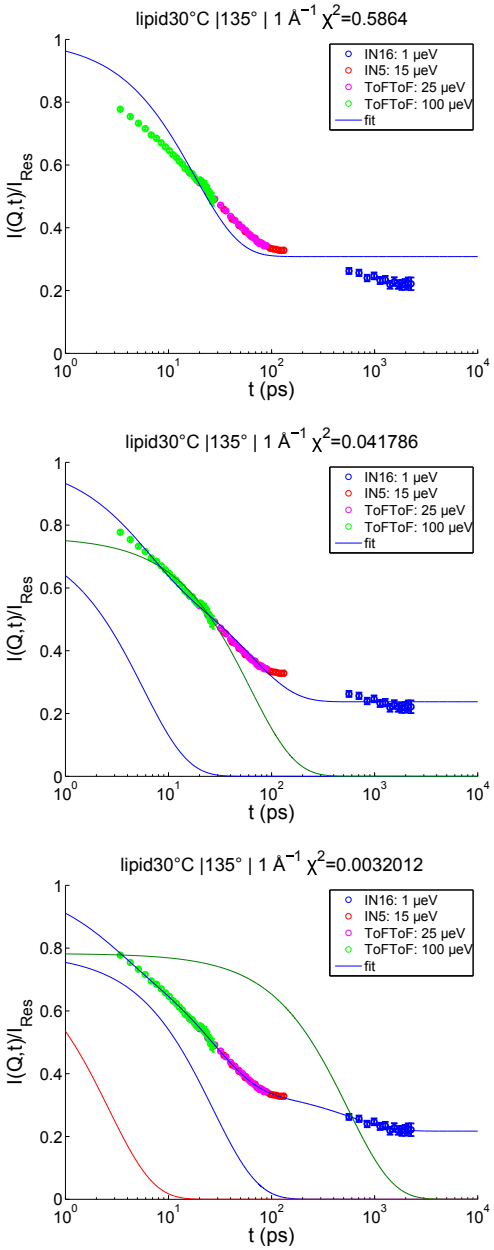

Figure 3.13: The combined intermediate scattering function for the lipid sample at 30°C and 135°. Top: an attempted fit with a single exponential, Equation 3.4. Middle: an attempted fit with the product of two exponentials. Bottom: an attempted fit with the product of three exponentials. For the two and three exponential fits, the individual components are plotted, as well as the product. These have been shifted vertically by the amplitude for clairity.

[134], resulting in Equation 3.6.

$$S_{theo}(\vec{Q},\hbar\omega) = S_1(\vec{Q},\hbar\omega) \otimes S_2(\vec{Q},\hbar\omega) \otimes S_3(\vec{Q},\hbar\omega) \tag{3.6}$$
$$\text{with}$$
$$S_i(\vec{Q},\hbar\omega) = [A_i\delta(\hbar\omega) + (1-A_i)L_i(\Gamma_i,\hbar\omega)]$$
$$\text{and}$$
$$L_i(\Gamma_i,\hbar\omega) = \frac{1}{\pi}\frac{\Gamma_i/2}{(\hbar\omega)^2 + (\Gamma_i/2)^2}$$

There are limitations of what can be observed by each particular spectrometer. It should only be possible to observe a specific relaxation when a spectrometer's instrumental resolution is *close* to the broadening which should be observed. Too fast of a process results in a dynamic structure factor with a very broad full-width at half maximum getting lost in the background noise, whereas a process which is too slow is narrow and cannot be separated from the instrumental resolution. The theoretical range is defined as $\frac{1}{10}(\Delta\tau_{resolution}) < \tau_i < 10(\Delta\tau_{resolution})$ [29] with $\tau_{res} = \frac{1.24ns\cdot\mu eV}{\Delta E}$ for a Gaussian-shaped resolution [128], although due to experimental uncertainties this range is sometimes smaller. By comparing the $\tau_{resolution}$ of the four measurements to the τ_i found from the analysis of the combined intermediate structure, simplifications of the theoretical dynamic structure factor can be made for each instrument. When a Lorentzian peak is too narrow (relaxation is too slow for this resolution), this contribution can be approximated as a Dirac-delta function. Alternatively, if a Lorentzian is too broad (relaxation too fast for this resolution), the contribution can be approximated as a broad and flat background.

When convolving two Lorentzians together, the result can be approximated as a Lorentzian with the width of the broader [31]. This approximation results in relatively simple scattering functions for each of the spectrometer's parameters, listed in Equation 3.7 and 3.8.

$$S_{IN16}(\vec{Q},\hbar\omega) = A_1\delta(\hbar\omega) + (1-A_1)L_1 + bg \tag{3.7}$$
$$S_{IN5,ToF8,ToF5}(\vec{Q},\hbar\omega) = [A_2\delta(\hbar\omega) + (1-A_2)L_2] \otimes [A_3\delta(\hbar\omega) + (1-A_3)L_3] \tag{3.8}$$

Using the model

Having generated a model which defines the relaxations which can be seen by each spectrometer, the fitting process can begin. The measured scattering function must be convoluted with the instrumental resolution and is rescaled by an instrumental scaling factor F, as is shown in Equation 3.9.

The backscattering instrument captures a single relaxation τ_1, and thus is fit with a single Lorentzian. The additional relaxations only contribute to a flat background,

as the dynamics are too fast to be observed on this spectrometer. An example fit is shown in Figure 3.14 a).

$$S_{measured}(\vec{Q},\hbar\omega) = F \cdot \Big[S_{theo}(\vec{Q},\hbar\omega) \otimes S_{resol}(\vec{Q},\hbar\omega)\Big] \tag{3.9}$$

Where:

$S_{measured}$:	is the measured dynamic structure factor, shown in Figure 3.9.
F:	is an instrumental scaling factor
S_{theo}:	is the theoretical dynamic structure factor
S_{resol}:	is the resolution function, defined by the instrumental resolution

The time-of-flight instruments each will experience contributions from the two fast relaxations τ_2 and τ_3. The slowest τ_1 contribution will appear as a Delta-contribution. Example fits from each spectrometer are shown in Figure 3.14 b), c) and d).

This fitting was performed for every Q value, to determine the broadening behaviour of each Lorentzian function. It was found that the IN16 backscattering scan, measuring on the ns scale, resulted in a Brownian-like broadening with respect to Q ($\Gamma = 2\hbar DQ^2$). The time-of-flight scans required an iterative fitting process. The fitting process started with the 15 μeV energy resolution scan (IN5). The narrow peak values (relating to τ_2) were then given as the start parameters for the 25 μeV ToFToF scan. The resulting fit for this value was then used as the start parameter for the ToFToF 100 μeV scan. The opposite order was then done with broad peak (relating to τ_3). This iterative fitting allowed both peaks to be fit with confidence, with the resulting slopes for each fitting function agreeing within error. The results of the fits are shown in Figure 3.15, and presented in Table 3.3.

It is assumed here that the small amount of amyloid-β peptide fragment is not enough to significantly change the nature of lipid motions, but only to modify the diffusion coefficients corresponding to these dynamics. Thus, the same fitting procedure is used for samples containing and without the peptides.

Since some of the diffusion coefficients were very close (often with overlapping error bars) statistical analysis was performed to test whether the differences between the samples with and without peptide were significant. This was performed as an unpaired t-test (also known as Welch's unequal variances t-test [135, 136]). The statistic, t (Equation 3.10), and the degree of freedom $d.f.$ (Equation 3.11) of the test were determined for each diffusion coefficient and its respective uncertainty and evaluated at the 95% confidence limit.

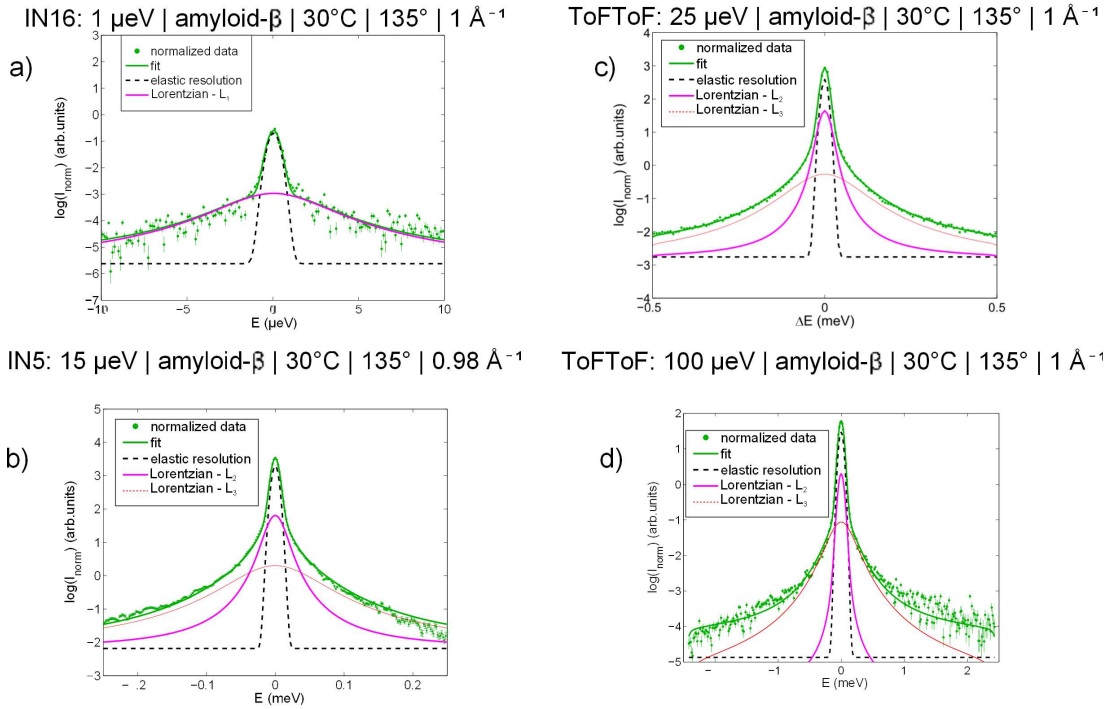

Figure 3.14: Exemplary QENS spectra and fits. For comparison, the Q∼1 Å^{-1} data from the four experimental resolutions are shown. a)IN16: ΔE=1μeV, b)IN5: ΔE=15μeV, c)ToFToF 8Å: ΔE=25μeV and d)ToFToF 5 Å: ΔE=100μeV. Data are shown on a logarithmic intensity axis with respective error values in green circles. This data set was fit using Equation 3.9, with Equations 3 and 4 of the main text as the theoretical scattering function. The data collected using IN16 were fit using Equation 3.7 with a single Lorentzian peak (pink), whereas two Lorentzian peaks (pink and red solid lines) as in Equation 3.8 were used to fit the IN5 (b) and ToFToF (c, d) data. The theoretical scattering functions were constructed by comparing the instrumental observation range to the relaxation times found using Equation 3.5

$$t = \frac{|m_1 - m_2|}{\sqrt{\frac{{s_{m_1}}^2}{n_1} + \frac{{s_{m_2}}^2}{n_2}}} \tag{3.10}$$

$$d.f. = \frac{\left(\frac{{s_{m_1}}^2}{n_1} + \frac{{s_{m_2}}^2}{n_2}\right)^2}{\frac{\left(\frac{{s_{m_1}}^2}{n_1}\right)^2}{n_1 - 1} + \frac{\left(\frac{{s_{m_2}}^2}{n_2}\right)^2}{n_2 - 1}} \tag{3.11}$$

Where:

m_i: are the fitted diffusion coefficients

s_{m_i}: are the standard uncertainty values of the diffusion coefficients

n_i: are the number of data points

60In the gel-phase ($15°C$), the peptide's presence changes the in-plane diffusion

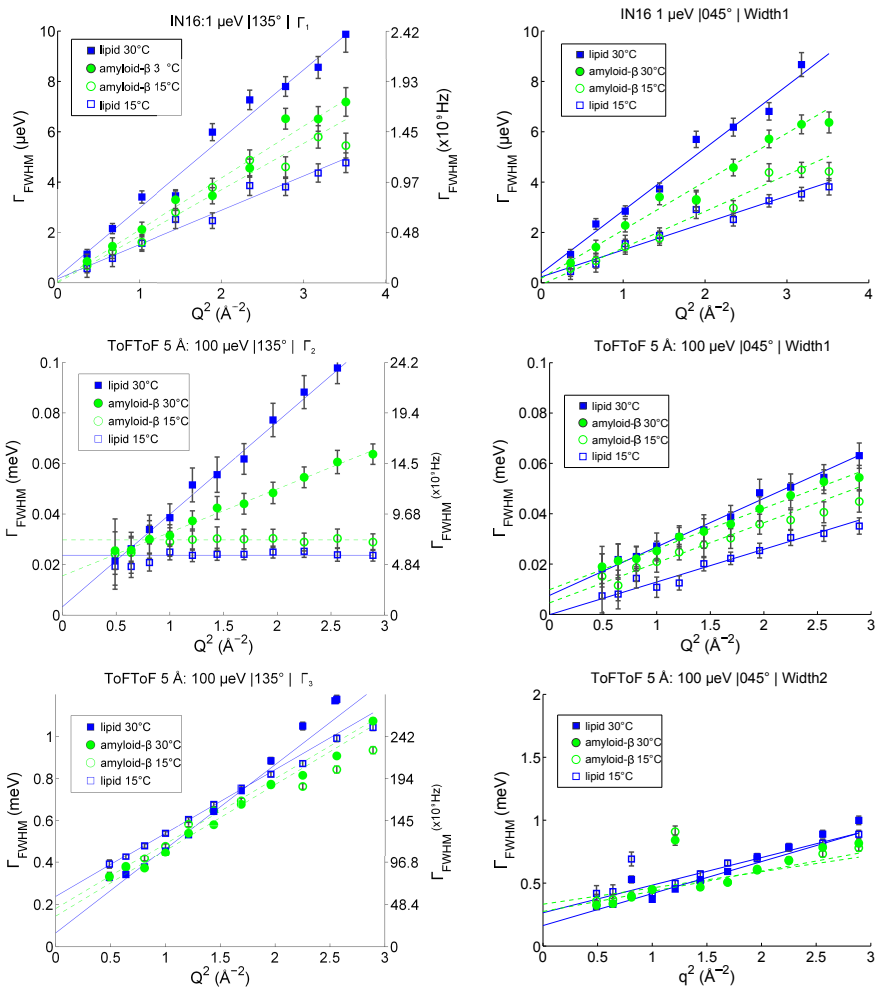

Figure 3.15: Quasi-elastic broadening of the L_1 (top), L_2 (middle) and L_3 (bottom) FWHM plotted against Q^2, fit to a Brownian diffusion model (L_1), a simplified diffusion model L_2 and L_3. The left column presents the in-plane dynamics, and the right column presents out-of-plane. Square blue data points correspond to the lipid sample, round green to the sample containing amyloid-β at 15°C and 30°C. For the middle and lower data sets only the ToFToF 100 μeV data is shown, but due to the iterative fitting process the other two time-of-flight measurements result in the same fit.

coefficient of the nanosecond (L_1) and mid-range (L_2) dynamics. The sample with peptide has larger diffusion constants than the pure lipid samples. All of the out-of-plane diffusion coefficients as well as the fastest (L_3) process in-plane are not significantly changed by the peptide's presence.

However, near the phase-transition temperature ($30°C$) the L_1 and L_2 diffusion coefficients show significant slowing both in-plane and out-of-plane. This is also seen

	L_1:45°	L_2:45°	L_3:45°	L_1:135°	L_2:135°	L_3:135°
15°C	D(x10^{-12} m^2/s)			D(x10^{-12} m^2/s)	D_{rot}(x$10^{10}/s$)	D(x10^{-12} m^2/s)
lipid	9.6±1.4	90±30	930±640	10.2±1.2*	3.6±0.1* †	1140±220
amyloid-β	10.1±0.6	100±20	630±450	11.7±1.4*	4.1±0.2* †	1160±200
30°C	D (x10^{-12} m^2/s)			D (x10^{-12} m^2/s)		
lipid	19.8±1.5*	127±22*	920±590	20.8±1.6*	250±30*	1620±300*
amyloid-β	14.3±0.9*	106±20*	760±600	15.8±1.4*	115±17*	1140±200*

Table 3.3: Diffusion coefficients determined from L_1, L_2 and L_3 Lorentzian width with respect to Q^2. The L_2 and L_3 coefficients were calculated as an average of the fitting for the three experimental energy resolutions which allow observation of these relaxations. The in-plane, 15°C values (labelled with †) are the rotational diffusion coefficient. An unpaired t-test (Welch's unequal variances t-test [135]) was performed to determine the statistical significance between diffusion coefficients of samples in the same experimental conditions (temperature and sample orientation). Differences between sample diffusion coefficients with and without peptide which are significant above the 5% confidence threshold are marked with (*).

for the fastest (L_3) diffusion constant when observed in-plane.

3.2 Conclusions and discussion

The structural and dynamic changes induced by 1.5 mol% of the peptide amyloid-β_{22-40} in anionic lipid bilayers (composed of 92 mol% DMPC and 8 mol% DMPS) were observed using neutron diffraction and quasi-elastic neutron scattering, respectively.

Through neutron diffraction with a deuterium labelled peptide, the location of the peptide marker could be determined, and the position of the peptide in the lipid bilayer could be inferred. The 39^{th} and 40^{th} residues of the peptide were labelled, leading to a clear maximum around ∼5 Å, providing evidence for peptide intercalation. This is in agreement with other neutron and X-ray diffraction experiments on the shorter amyloid-β_{25-35} peptide [22, 84, 86].

It is also worth noting that the bilayer *d*-spacing significantly increases (a 2 Å increase) for samples containing this small amount of peptide. This is seen for both the hydrogenated and the deuterium-tagged peptides in the bilayer. This is in agreement also with the previous structural measurements on other peptide fragments. The increased *d*-spacing may be the result of the peptide entering into the fluid-phase bilayer, and suppressing the fluctuations of the chains, a condensing effect, as has

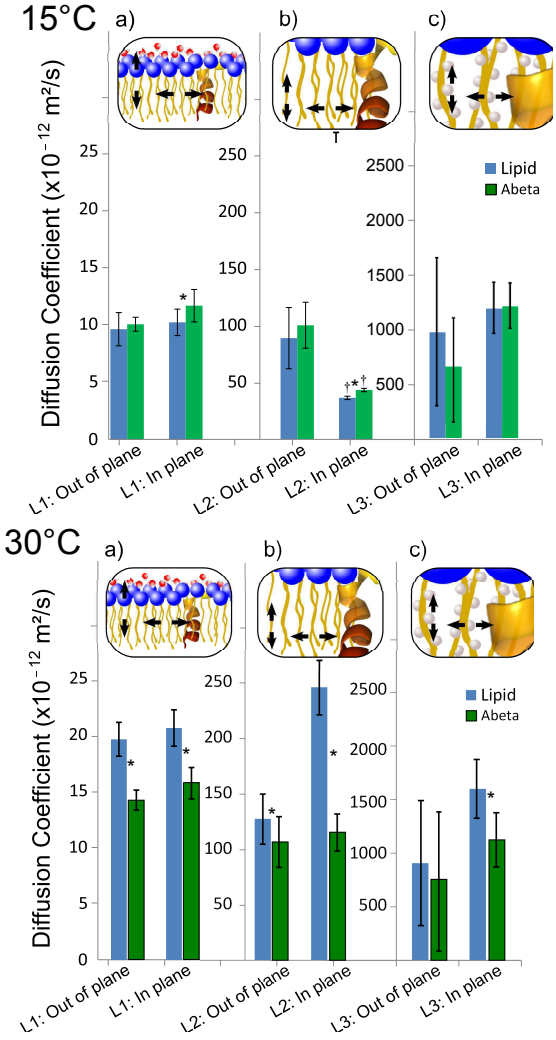

Figure 3.16: Diffusion coefficient comparison of the three relaxation processes at 15°C (left) and 30°C (right) as reported in Table 3.3, the L2 and L3 diffusion coefficients were averaged from the three time-of-flight measurement results. A cartoon describing potential dynamical processes associated with each relaxation is shown for each relaxation: a) whole lipid Brownian diffusion, b) chain kink and lipid tail dynamics, c) methyl and methylene group dynamics. The pure lipid sample is represented by the blue bars, whereas the sample containing amyloid-β is shown in green. The 15°C in-plane τ_2 (marked with †) was fit with a rotational diffusion model, units are 10^{10} s^{-1}. Statistically significant differences (95% confidence level) are marked with $*$

been reported for cholesterol [137, 138]. With a very small amount of peptide, local hydrophobic chains fluidity may be restrained. This strong local effect could also spread

to lipids not in direct contact with the peptide, but lipids attempting to mitigate the hydrophobic mismatch the peptide causes hydrophobic mismatch in the bilayer [139, 140].

With strong evidence that the 1.5 mol% of amyloid-β_{22-40} peptide intercalates into the bilayer and results in increased *d*-spacing, dynamical studies were carried out to determine what effect this peptide would have on the lipid dynamics in the bilayer.

A series of quasi-elastic neutron scattering experiments on aligned lipid bilayer samples with and without a 1.5 mol% peptide amyloid-β_{22-40} were performed. Measurements at four different instrumental resolutions allow for processes in a time-window from ∼1 ps to ∼1 ns to be observed. The data for Q=1 $Å^{-1}$ was Fourier transformed from the measured dynamic structure factor into the intermediate scattering function. A combined intermediate scattering function was produced by plotting the four dynamic structure factors together. Three processes could be observed, and can be attributed to whole lipid molecule Brownian diffusion, chain-kink diffusion and rotation, and methylene and methyl bound hydrogen atom dynamics.

In the presence of the peptide, a decrease in lipid diffusion coefficient was observed in all three relaxation processes at 30°C in the plane of the lipid bilayer, with a dramatic twofold decrease occurring in the τ_2 process: relating to lipid chain motions. In the gel-phase, a slight increase of the nanosecond and mid-picosecond lipid diffusion coefficients were found in the peptide containing sample in-plane, with no significant change out-of-plane.

At 30°C, near the phase transition temperature, the addition of the amyloid-β peptide fragment causes a drastic decrease in both the nanosecond and picosecond lipid dynamics. The addition of the peptide introduces an obstacle into dynamic lipid membrane, and thus the lipid diffusion coefficients are up to two times smaller in the presence of the amyloid-β peptide. The in-plane diffusion coefficients at 30°C are shown in Figure 3.16. The out-of-plane orientation also exhibits this trend, but the effect is not as dramatic and is not statistically significant for the fastest process. This result echoes our group's previous observations of the short Aβ_{25-35} peptide fragment's effect on lipid dynamics. Near the phase-transition temperature (∼30°C) the value of the diffusion coefficient decreases with the addition of Aβ_{25-35} [44].

On the other hand, at 15°C, in the gel-phase of the DMPC/DMPS mixture, the addition of the amyloid-β peptide fragment causes an increase in the lipid diffusion as observed over mid-picosecond to nanosecond timescales in-plane. If we take the evidence from Section 3.1.1 that the peptide intercalates into the membrane, the addition of this small amount of peptide may perturb the rigid gel-structure of the lipid tails and may overpower or alter the gel phase interaction between lipid molecules. This is in agreement with the observation at 15°C made previously for the hydrophobic Aβ_{25-35} peptide fragment[44]. The out-of-plane are not significantly effected by the peptide.

Additionally, in 2012, our group measured the effect of the presence of amyloid-β peptide fragments (22-35) and (22-40) on local lipid dynamics at 47°C (fluid phase) using QENS [45]. The spectra over all Q-values were summed and the resulting

Lorentzian half-width with and without peptide was compared. The presence of both $A\beta_{25-35}$ and $A\beta_{22-40}$ peptide fragments resulted in an increase of the width of the quasi-elastic contributions, hinting at an acceleration of the lateral diffusion of the lipids. In comparison to the 30°C measurement presented here, the peptide's effect of lowering lipid diffusion may occur only near the phase transition temperature, while at a higher temperature (47°C, as was measured previously) this effect is not large enough to compete with the kinetic energy of the system and as a result the peptide increases the lipid diffusion coefficient. Further measurements are necessary to compare this effect for the longer $A\beta_{22-40}$ at fluid phase temperatures.

In the present study, the decrease of lipid diffusion caused by the addition of $A\beta_{22-40}$ at 30°C (near the phase transition) is reminiscent of the influence of cholesterol and sodium glycocholate, as has been measured by Busch and Unruh [81]. $A\beta_{22-40}$ has both hydrophobic and hydrophilic domains, similar to cholesterol and sodium glycocholate. The presence of both hydrophilic and hydrophobic domains may influence the observed effect of these molecules.

A very recent study by Sharma *et al.* [33] uses a very similar approach to test the effect of the antimicrobial peptide melittin, a peptide of similar length and hydrophobicity to the amyloid-β_{22-40} peptide studied in this thesis. DMPC bilayer samples were prepared with and without a small molar amount (0.2 mol%) of melittin peptide and dynamical measurements were made in the gel and fluid phase of the bilayer. In the gel-phase, a small but considerable increase of nanosecond lipid diffusion was observed, whereas above the main phase transition temperature of the bilayer a considerable decrease in lipid lateral diffusion was observed with the presence of the peptide. These results reflect very closely the experimental findings presented in Section 3.1.2.

As of today, there is no consistent explanation of the cause of the symptoms of Alzheimer's disease. There has been much discussion in the literature about the role that amyloid-β peptides play in AD, and whether the toxicity arises from amyloid peptide plaques, monomeric peptides, some oligomeric intermediate structure or a combination of all of these forms [20, 141, 142]. The perturbation in lipid dynamics which are observed in the model membrane reflect the more complex behaviour of lipids in neuronal membranes, and may be responsible for autocatalytic increases in peptide cleavage by β- and γ- secretases [7, 8, 18], changes in fusion and vesicle formation processes involved in the signalling cascade [11, 12, 13, 26] or complications in ATP production for energy demanding synaptic processes [9, 10].

The clear trend of decreased lipid diffusion at 30°C, and increased diffusion at 15°C with the addition of only 1.5 mol% $A\beta_{22-40}$ presented in this chapter indicates that the lipid molecules' dynamic behaviour is dramatically affected by even a small amount of peptide. If monomeric forms of the peptide can cause changes in the diffusive motions of the lipids in neural cell membranes, as was presented in this paper for model membranes, significant changes to the processes which are regulated by lipid-lipid, lipid-protein and protein-protein interactions will be perturbed, leading to toxicity.

3.3 Notes

- A manuscript containing this work was published in Soft Matter.
  - **Barrett, M.**, Trapp, M., Lohstroh, W., Seydel, T., Ollivier, J., Ballauff, M., Dencher, N. and Hauß, T. “Alzheimer’s peptide amyloid-β, fragment 22-40, perturbs lipid dynamics." (2016) Soft Matter. 12, 1444-1451.

4 Amyloid-β peptide fragments in cholesterol-rich membranes

The next step in exploring the effect of amyloid-β fragments on model lipid membranes was to create more physiologically realistic membranes. Cholesterol is present in the membranes of eukaryotic cells, often in high molar ratios. The presence of cholesterol regulates membrane fluidity, and is often associated with the formation of protein complexes in the membrane [71].

A connection between Alzheimer's disease and cholesterol was first proposed by Sparks *et al.* in 1990 [143], but there is no consensus in the literature about cholesterol's role in the symptoms of the disease [144, 145, 146]. Approximately 25 mol% of the molecules making up synaptic membranes are cholesterol [87], which would make the synapse sensitive to cholesterol changes.

Cholesterol distribution and concentration in cells changes with aging [147, 148, 149], with high cholesterol levels often viewed as a risk-factor for Alzheimer's disease [150, 151]. Cholesterol has been shown to promote the activity of β secretase, increasing the production of amyloid-β from the amyloid precursor protein [152]. On the other hand, the neuronal cells of Alzheimer's disease patients have been observed to be depleted in cholesterol [153], leading to the notion that a cholesterol decrease allowed for the symptoms to manifest.

To gain a better understanding of how cholesterol effects the interaction of amyloid-β with lipid bilayers, experiments have been performed with various peptide fragments and model membranes containing cholesterol. Dante *et al.* have experimented with the amyloid-β_{25-35} peptide in bilayers containing cholesterol [77]. They have shown that by increasing the amount of cholesterol in the bilayer, the percentage intercalated peptide decreases, with no observable signal for a sample containing 20 mol% cholesterol. Recently, Dies *et al.* have shown that for a model membrane with saturated cholesterol plaques, the addition of the amyloid-β_{25-35} peptide pushes cholesterol out of the lipid portion of the bilayer and causes an increase in the amount of cholesterol in the plaques [86].

The interaction of larger peptides with cholesterol-rich membranes has not been characterized to high resolution of structural scattering experiments. In the following chapter, the structural changes in anionic lipid bilayers containing cholesterol induced by the full-length amyloid-β_{1-42} and the fragment amyloid-β_{22-40} are presented.

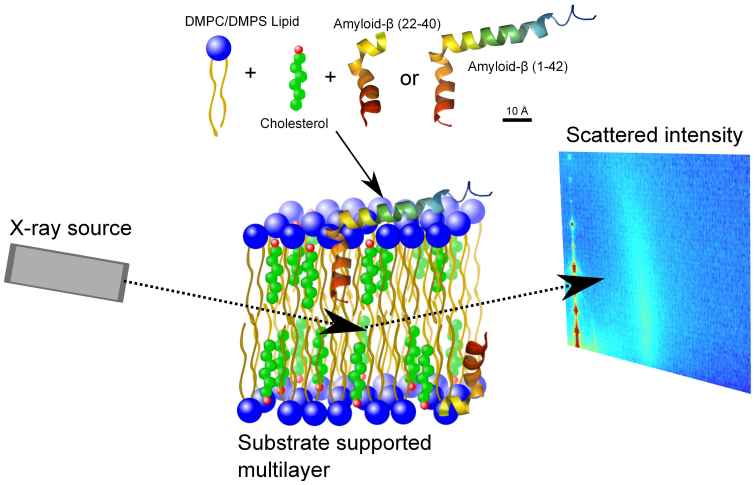

Figure 4.1: Schematic of the experimental setup. Samples were prepared with DMPC and DMPS lipids, cholesterol and amyloid-β_{22-40} or amyloid-β_{1-42} peptides. The samples were prepared as multiple hydrated lipid bilayers on a silicon substrate. The in- and out-of-plane X-ray scattering is gathered in a 2 dimensional reciprocal space map with a point detector.

4.1 Experimental results

X-ray diffraction experiments were performed on a series of samples consisting of a 92 mol% DMPC: 8 mol% DMPS lipid ratio and a variable amount of cholesterol, ranging from 10 mol% to 50 mol%. A selection of samples also contained 1.5 mol% of amyloid-β peptide, either the fragment amyloid-β_{22-40}, or the full-length amyloid-β_{1-42}. The composition of these samples, as well as experimentally derived quantitative parameters are presented in Table 4.1. Lipid bilayer samples were prepared using the method described in Section 2.4, depositing a mixture of lipids, cholesterol, peptide and solvent using an air-brush onto silicon wafers and allowing the solvent to evaporate in a vacuum desiccator after deposition. The samples were hydrated to 91% relative humidity in a sealed aluminum container with thin Kapton windows, and held at a constant temperature of 32°C during the X-ray diffraction experiment.

The details of the X-ray diffraction experiment are described in Section 2.2.1. The diffraction experiments resulted in a 2D reciprocal space map for each sample, providing separate information on both the in-plane and out-of-plane structure of the model membrane sample simultaneously.

The reciprocal space map obtained for each sample was treated in two separate fitting procedures to determine in-plane and out-of-plane details of the samples. The first, and most straightforward procedure was to determine the nearest-neighbour distance of the lipid hydrocarbon tails, in-plane. An integration of the intensity in-plane is made (as shown in Figure 4.3 a).

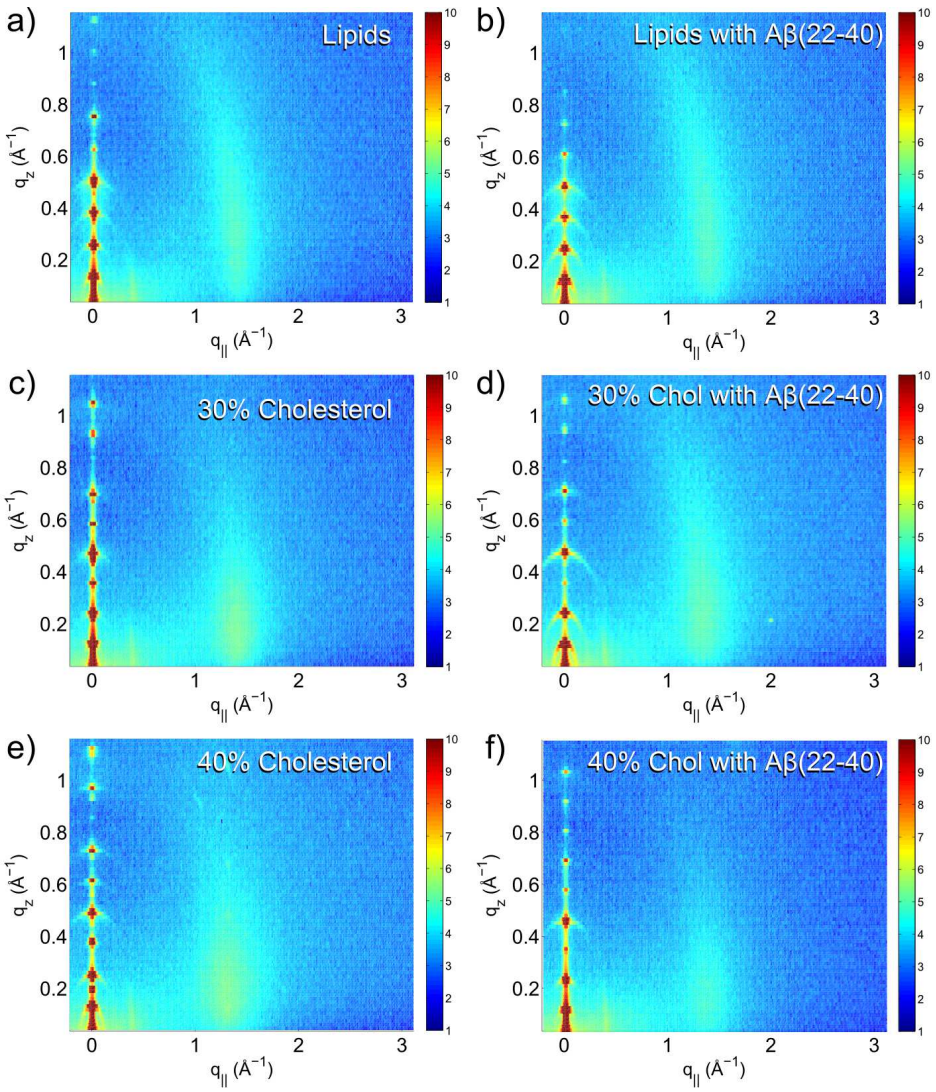

Figure 4.2: 2D reciprocal space maps of a selection of samples at 93% relative humitidy and 32°C. a) DMPC/DMPS (92/8%) lipids, b) lipid with 1.5 mol% amyloid-β_{22-40}, c) lipids with 30 mol% cholesterol, d) lipids with 30 mol% cholesterol and 1.5 mol% amyloid-β_{22-40}, e) lipids with 40 mol% cholesterol and f) lipids with 40 mol% cholesterol and 1.5 mol% amyloid-β (22-40).

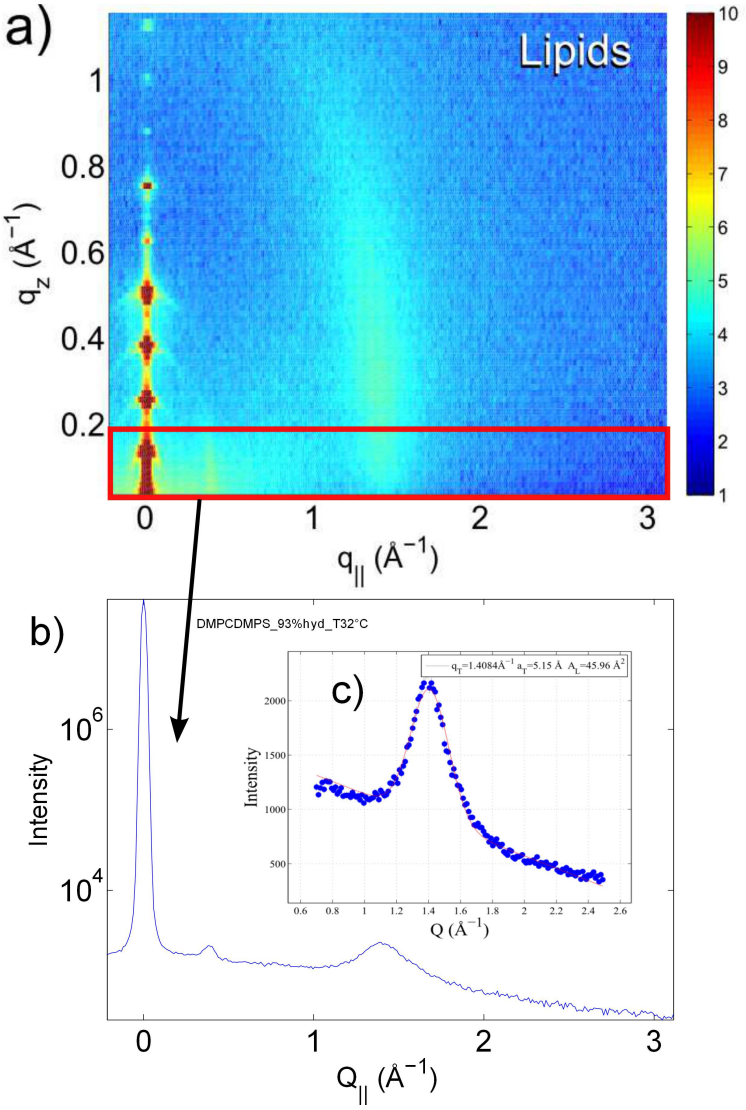

Figure 4.3: The in-plane nearest-neighbour fitting procedure. a) The reciprocal space map of a DMPC/DMPS sample, the red box indicates the area to be integrated, from $0 \leq Q_{||} \leq 0.2$ Å. b) The integrated intensity curve displayed logarithmically. c) A Gaussian fit to the lipid tail nearest-neighbour distance peak. The peak-centre q_T is used to determine the nearest-neighbour distance, and the area per lipid.

This nearest-neighbour distance is then used to calculate the area per lipid ($A_L = 16\pi^2/(\sqrt{3}{q_T}^2)$ [115, 154, 155], with q_T being the centre of the Gaussian peak used to fit the area per lipid. The assumption was made that the lipid tails are structurally ordered in hexagonal lattice, which is broad due to thermal fluctuations of the tails in the fluid phase. On the other hand, in the gel-phase of pure DMPC, the tails are much less mobile, resulting in sharper peaks (see reference [115]).

The out-of-plane scattering provides much more detailed information than the in-plane, and as such, the analysis is much more involved. The first step is to determine the lamellar repeat spacing (d-spacing) of the sample. Since the sample itself is made of thousands of repeating lipid bilayer/water units, with regularly spaced regions of different electron density the scattering arises as a series of constructive scattering peaks or Bragg peaks. By fitting the location of each of these peaks in reciprocal space, and converting to real-space ($d = 2\pi/Q$), the d-spacing of the sample can be determined with great accuracy. This procedure is presented in Figure 4.4.

The next set of data which can be extracted from the out-of-plane scattering peaks is the electron density of a unit cell in our sample. For each peak identified in the previous step, the area under the peak was determined with a trapezoidal integration. The phase coefficient array was taken as identical to the phasing used in [155], that is [-1 -1 1 -1 1 -1 1 -1 1 1 -1]). With these details, as well as the d-spacing (determined above), the Fourier reconstruction for selected samples was performed resulting in an electron density profile for each sample. This process is described in detail in Section 2.2.1.

From the electron density profiles, the maximum-to-maximum (d_{MM}) distance can be estimated (from the peaks of the electron density profiles). In the cases of a bilayer without peptide, this can be used to quantify the head-to-head distance, although with peptide the electron density can be further affected. An estimate of the water thickness (d_{water}) can also be obtained, by subtracting the total d-spacing from the maximum-to-maximum distance. These parameters are presented in Table 4.1.

The data presented in Table 4.1 has also been plotted in Figure 4.6. By following the changing parameters with increased cholesterol content, some trends begin to emerge. The samples which do not contain any peptide behave very similar to a DMPC/cholesterol system as described in reference [155]. For samples with a cholesterol content greater than 40 mol%, additional peaks which can be associated with cholesterol plaques, or a mixed lipid/cholesterol layer emerge. The d-spacing of the bilayer increases slightly with increased cholesterol content in the lower cholesterol range (<40 mol%), which is to be expected for a fluid-phase saturated lipid bilayer system [156]. At 40 mol%, a drop in d-spacing is observed, which is linked to formation of cholesterol plaques, therefore cholesterol leaving the lipid region of the bilayer. The 50 mol% cholesterol sample's d-spacing is very similar to the 40 mol%, indicating that the excess 10% cholesterol simply joins the plaque.

The presence of only 1.5 mol% of the peptide present in the sample results in an increase of the solubility limit of cholesterol in the bilayer. In reflectivity curves for the 40 mol% sample without peptide (Figure 4.5 a), peaks associated with the cholesterol plaques and a mixed domain containing cholesterol and lipid molecules are observed.

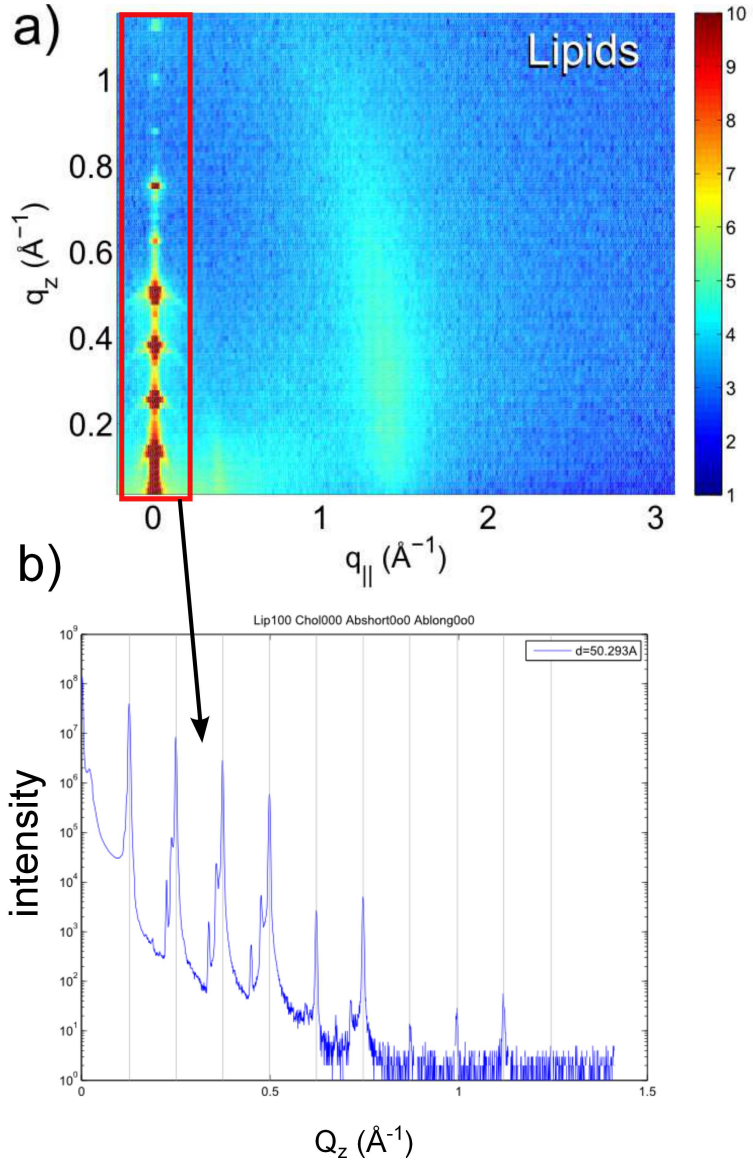

Figure 4.4: The out-of-plane nearest-neighbour fitting procedure. a) The reciprocal space map of a DMPC/DMPS sample, the red box indicates the area to be integrated, from $0 \leq Q_z \leq 1.2$Å. b) The integrated intensity curve displayed logarithmically. c) The reflectivity and lines fit to peak maxima, used to determine the d-spacing of the sample.

DMPC (mol%)	DMPS (mol%)	Chol (mol%)	Aβ_{22-40} (mol%)	Aβ_{1-42} (mol%)	d* (Å)	d_{MM}* (Å)	d_{water}* (Å)	A_L (Å^2)
Without peptide								
92.0	8.0	0	-	-	50.3	35.2	15.1	46.0 ± 0.2
82.8	7.2	10	-	-	52.7	-	-	46.4 ± 0.4
64.4	5.6	30	-	-	54.3	39.7	14.6	46.7 ± 0.1
59.8	5.2	35	-	-	54.3	-	-	47.3 ± 0.2
55.2	4.8	40	-	-	51.8	40.5	11.3	51.8 ± 0.4
46.0	4.0	50	-	-	51.4	-	-	53.6 ± 0.3
Aβ_{22-40}								
90.6	7.9	0	1.5	-	52.0	37.8	14.2	46.5 ± 0.1
63.4	5.5	29.6	1.5	-	53.2	40.0	13.2	50.2 ± 0.3
54.4	4.7	39.4	1.5	-	54.8	41.4	13.4	47.6 ± 0.1
45.3	3.9	49.3	1.5	-	58.4	-	-	50.5 ± 0.3
Aβ_{1-42}								
63.4	5.5	29.6	-	1.5	55.3	39.1	16.2	46.7 ± 0.2
54.4	4.7	39.4	-	1.5	54.6	40.4	14.2	47.6 ± 0.1
45.3	3.9	49.3	-	1.5	52.7	-	-	50.3 ± 0.3

Table 4.1: Composition of samples and measured sample parameters. d: lamellar repeat distance calculated from the Bragg peaks found in the reflectivity (all experimental uncertainties ±0.1Å), d_{MM}: maximum-to-maximum distance as determined from a Fourier reconstruction, d_{wat}: water layer spacing; calculated from d-d_{MM} and A_L: area per lipid, calculated from the in-plane Bragg rod location. (* with an uncertainty of ±0.1Å)

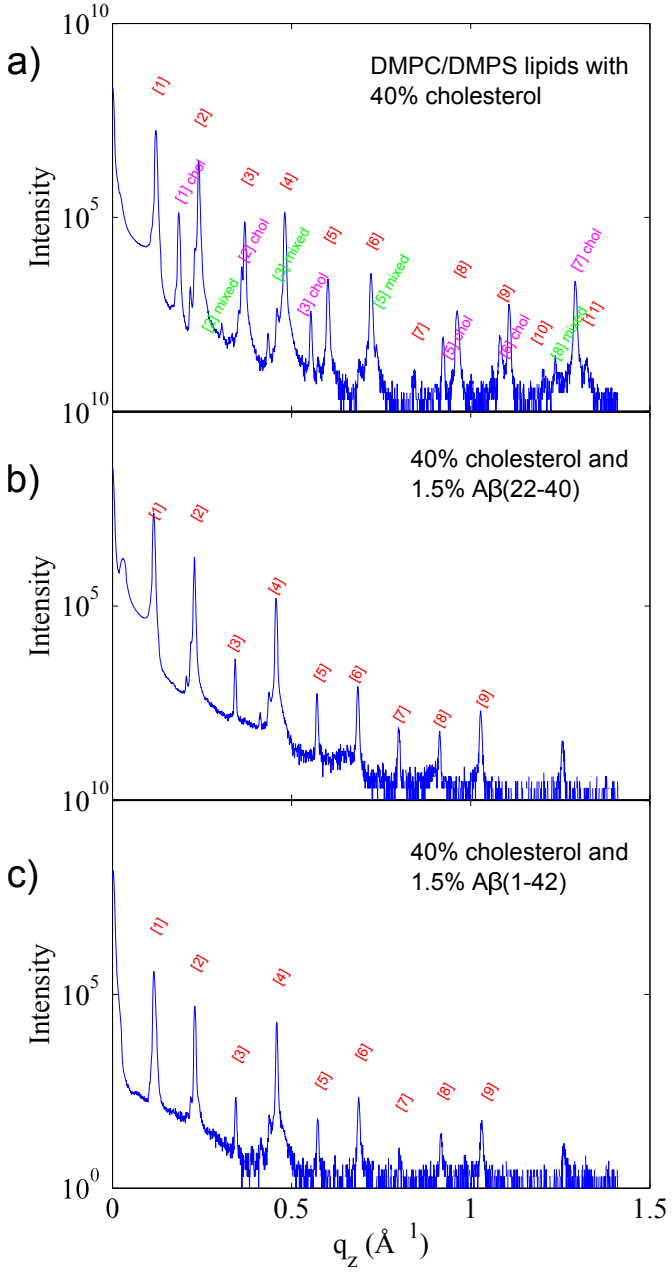

Figure 4.5: Reflectivity and peak assignment of a) DMPC/DMPS with 40 mol% cholesterol, b) DMPC/DMPS with 40 mol% cholesterol and 1.5 mol% $A\beta_{22-40}$ and c) DMPC/DMPS with 40 mol% cholesterol and 1.5 mol% $A\beta_{1-42}$. Peaks which correspond to a lamellar phase are presented in red. In the sample without peptide (a), peaks relating to a full cholesterol bilayer (pink), and a mixed lipid and cholesterol bilayer (green) are also observed.

These peaks do not appear in Figure 4.5 b, or Figure 4.5 c, the two samples with peptide. The *d*-spacing at 40 mol% for both samples containing peptide does not drop drastically in the lipid and cholesterol sample without peptide.

In Figure 4.6 a the sample series containing amyloid-β_{22-40} indicates that the bilayer repeat distance continues to increase up to 50 mol% cholesterol (which was the highest cholesterol sample produced). The *d*-spacing at 50 mol% cholesterol increases to a dramatic 58.4 Å.

The sample series containing amyloid-β_{1-42}, on the other hand, exhibits a gradual decrease in *d*-spacing when the cholesterol content increases from 30 mol% to 50 mol%. This decrease may be related to the fusiogenic effect of the full-length peptide [23]. This decrease in d-spacing is linked to a decrease in water-thickness (d_{wat} in Figure 4.6c). The thinning of the water layer may be due to electrostatic effects of the hydrophillic part of the peptide residing on the surface of the bilayer (as shown in the model fitting, Figure 4.10 b and d)

4.1.1 Position of peptide fragments in a lipid membrane

The electron density was scaled using the electron density of the unit cell as determined by the molar contents of each sample, and with the centre of the bilayer held at a constant 0.22 $e^-/\text{Å}^3$, the density of a methyl (CH_3) group found at the end of the lipid chain. For samples containing amyloid-β peptides, the electron density profile was further scaled to account for depletion of electron density caused by changing *d*-spacing and lead to a clearer difference between samples with and without the peptide. This step in the scaling procedure was also recently used by Alsop *et al.* to determine the location of Ibuprofen molecules in DMPC [157].

Assuming no drastic changes in the bilayer structure with the addition of the peptide, as was demonstrated in Section 3.1, the difference in electron density between the two profiles can be made. The difference profile will describe the location of the peptide. A difference plot for the DMPC/DMPS bilayer (without cholesterol) was created (see Figure 4.7 a). The difference between the electron density profile without peptide was subtracted from the counterpart containing 1.5 mol% amyloid-β_{22-40}. This difference is plotted in blue (measured) in Figure 4.7 b. A modelling procedure (described below) is used to determine the position of the peptide.

It is worth noting that if the bilayer structure undergoes major changes in the presence of the peptide, a direct subtration may not provide useful information regarding the peptide location or orientation. A more direct method would be observing deuterium labelled peptides in the bilayer. Since neutron diffration experiments are limited by low neutron flux and thus a small number of Bragg orders, the resolution of the Fourier transformation is often limited. The advantage to the X-ray diffraction experiment is the high number of Bragg orders, resulting in detailed high-resolution electron density plots, which can be compared with electron density profiles of peptide molecules. In the cases presented by previous authors for the amyloid-β_{25-35} fragment [22], and in this thesis in Figure 3.5 with neutron diffraction data, major changes in the bilayer structure are not observed, and thus a comparison of the electron density

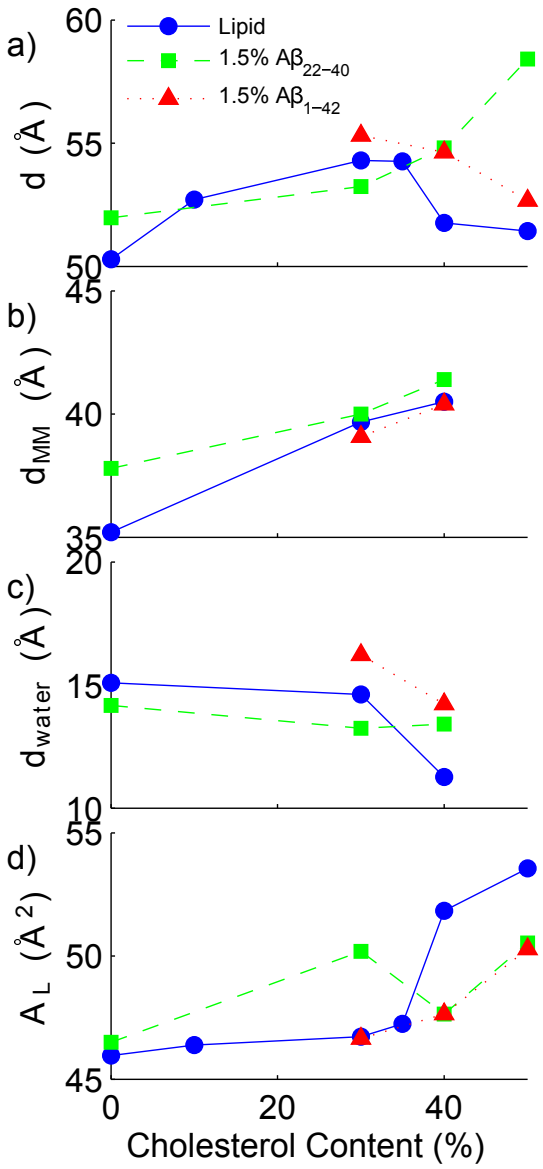

Figure 4.6: The dependence of a) *d*-spacing, b) maximum-to-maximum distance, c) water thickness and d) area/lipid on cholesterol content in the bilayer. Three sets of samples are presented, the sample series without peptide is represented by the blue circles and solid line, samples containing amyloid-β_{22-40} are shown with green squares and dashed lines, and samples with amyloid-β_{1-42} are shown with red triangles and dotted lines.

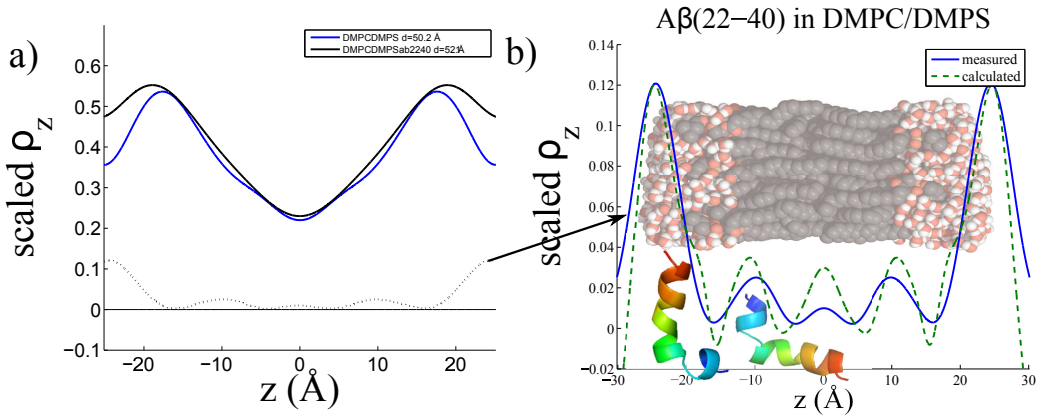

Figure 4.7: a) DMPC/DMPS electron density profile (blue) and DMPC/DMPS with 1.5 mol% amyloid-β_{22-40} (black). The difference between the electron density profiles is shown with a dotted line. b) The measured difference from a) is plotted in blue overlaid with the calculated model peptide distribution in green dotted. The two population model with one peptide population on the surface and the other embedded in the membrane best fits the experimental data.

profiles of a sample with and without peptide provides a high-resolution description of the peptide location and orientation.

The peptide itself is a complex molecule, with a large atomic variation in structure, and thus a complex electron density profile. To determine the position of the peptide, models were constructed using a solution structure of the peptide from the *Protein Data Bank* (reference 1IYT [158]). The orientation of the peptide was manipulated using PyMol [126]. The resulting electron density in 3D is projected onto the axis to give the electron density relating to the out-of-plane position. An example of one orientation of this modelling is shown in Figure 4.8. The position of each atom is plotted along the z-axis with the atom's associated number of electrons (e.g. a Hydrogen atom will have n_e^-=1, a Carbon atom has n_e^-=6). Since the peptide in our experiment was not in a cryogenic state, a thermal fluctuation was introduced to the model. Each atom was assumed to occupy a Gaussian distribution around the position derived from the PDB coordinate. This results in an electron density profile model which can be compared with the measured electron density profile.

4.1.2 Position of peptide fragments in a cholesterol rich membrane

Similarly to the pure lipid sample, the differences between samples containing 30 mol% and 40 mol% cholesterol were also measured (Figure 4.9). The electron density differences in most cases (except the 40 mol% cholesterol with amyloid-β_{1-42} peptide) could not be modelled with a single peptide population, as was seen for the cholesterol-free samples. The model which best represented the experimentally

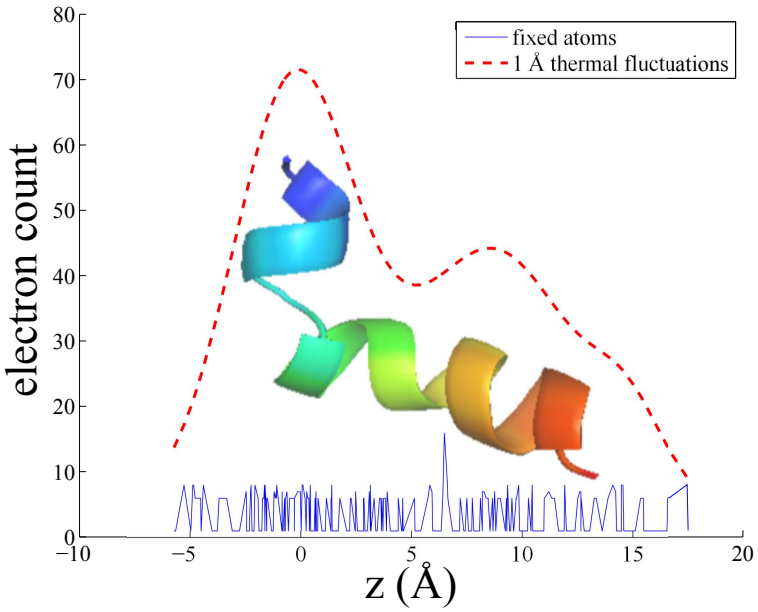

Figure 4.8: The modelled electron density profile of an amyloid-β_{22-40} peptide in the "parallel" orientation (C-terminus parallel to the lipid bilayer hydrocarbon tails). The blue *fixed atoms* data represent the number of electrons per atom, according to the z-position of the atom. The highest blue peak at ∼6 Å relates to the Sulfur atom (16 electrons) found in the amino-acid Methionine in position 35. The red-dashed line represents the electron density with each atom represented by a Gaussian distribution arising from thermal fluctuations.

determined electron density profile for each sample and represented a physically feasible situation was chosen. The modelled electron density profiles are presented in Figure 4.10.

The position of each peptide was modelled above and below the solubility limit of cholesterol in the bilayer, that is at 30 mol% and 40 mol%, for the fragment amyloid-β_{22-40} and the full-length amyloid-β_{1-42}.

Position of amyloid-β_{22-40}

A two population model best describes the location of the 22-40 peptide, with one population oriented parallel to the lipid tails, and the other rotated 90°, laying on top of the bilayer.

When increasing from 0 mol% cholesterol content and from 30mol% to 40mol%, no change in the orientation of the surface population is observed, however the intercalated population adopts a position where the long-axis of the peptide is parallel with the lipid bilayer tails, slightly rotated from the 30 mol% case, and pushed further away from the centre of the bilayer. The cholesterol-free sample's electron density difference indicates the end of the peptide resides near the centre of the bilayer, which agrees with the labelled neutron experiments in Section 3.1, which showed evidence of the 39^{th} and 40^{th} residues intercalated into the bilayer.

This finding supports previous X-ray and neutron scattering results with the amyloid-β_{25-35} peptide [77, 86]. Both of these publications report multiple peptide populations in the lipid bilayer. In the X-ray experiment (Dies *et al.* [86]), for a DMPC/DMPS membrane containing 30 mol% cholesterol, two surface bound populations are modelled, plus an embedded (intercalated) state. In the neutron scattering study (Dante *et al.* [77]), two peptide populations are observed, one on the surface, and one embedded into the membrane. Dante *et al.* report in a POPC/POPS membrane that as cholesterol content increases, the amount of peptide which embeds into the membrane decreases, up to 20 mol% cholesterol, which completely prevents intercalation.

Our modelling reflects this effect, as the ratio between surface and intercalated peptides increases with increasing cholesterol content. At 30 mol% cholesterol a ratio of 55:45 surface:embedded was modelled, whereas at 40 mol% cholesterol the ratio changes to 70:30 surface:embedded.

The two position model may also be related to the two stage model of peptide/membrane interactions [159, 160, 161]. This model describes two positions for a peptide. First: a peptide comes into contact with the membrane, typically the membrane surface. Second: the peptide embeds itself into the membrane surface, when the free-energy of insertion is overcome. The increase of cholesterol content may increase the free-energy of insertion [162], resulting in a larger population of surface and lower population of embedded peptides.

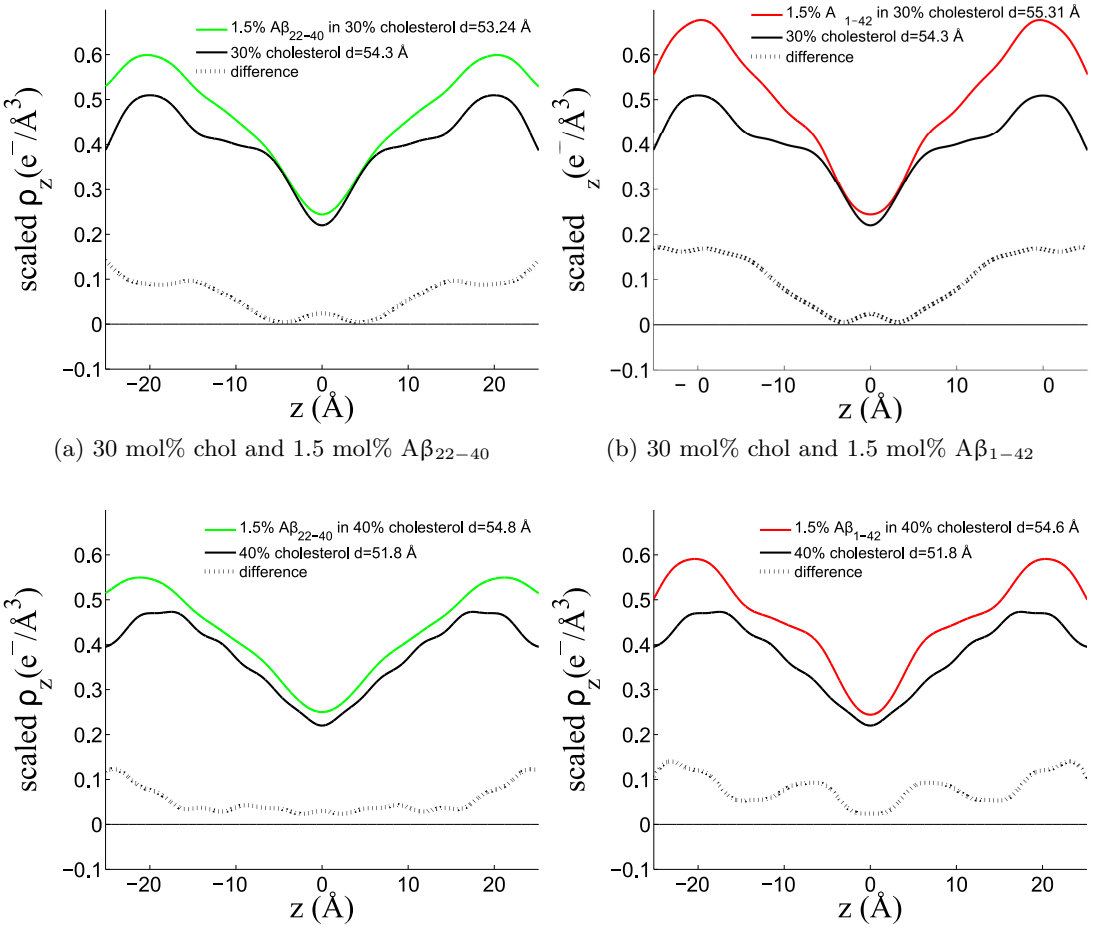

(a) 30 mol% chol and 1.5 mol% $A\beta_{22-40}$

(b) 30 mol% chol and 1.5 mol% $A\beta_{1-42}$

(c) 40 mol% chol and 1.5 mol% $A\beta_{22-40}$

(d) 40 mol% chol and 1.5 mol% $A\beta_{1-42}$

Figure 4.9: Fourier reconstructions of out-of-plane bilayer structure. a) DMPC/DMPS membrane with 30 mol% cholesterol (black line) and amyloid-β_{22-40} (green line) and difference (black dotted line) b) DMPC/DMPS membrane with 30 mol% cholesterol (black line) and amyloid-β_{1-42} (red line) and difference (black dotted line) c) DMPC/DMPS membrane with 40 mol% cholesterol (black line) and amyloid-β_{22-40} (green line) and difference (black dotted line) d) DMPC/DMPS membrane with 40 mol% cholesterol (black line) and amyloid-β_{1-42} (red line) and difference (black dotted line)

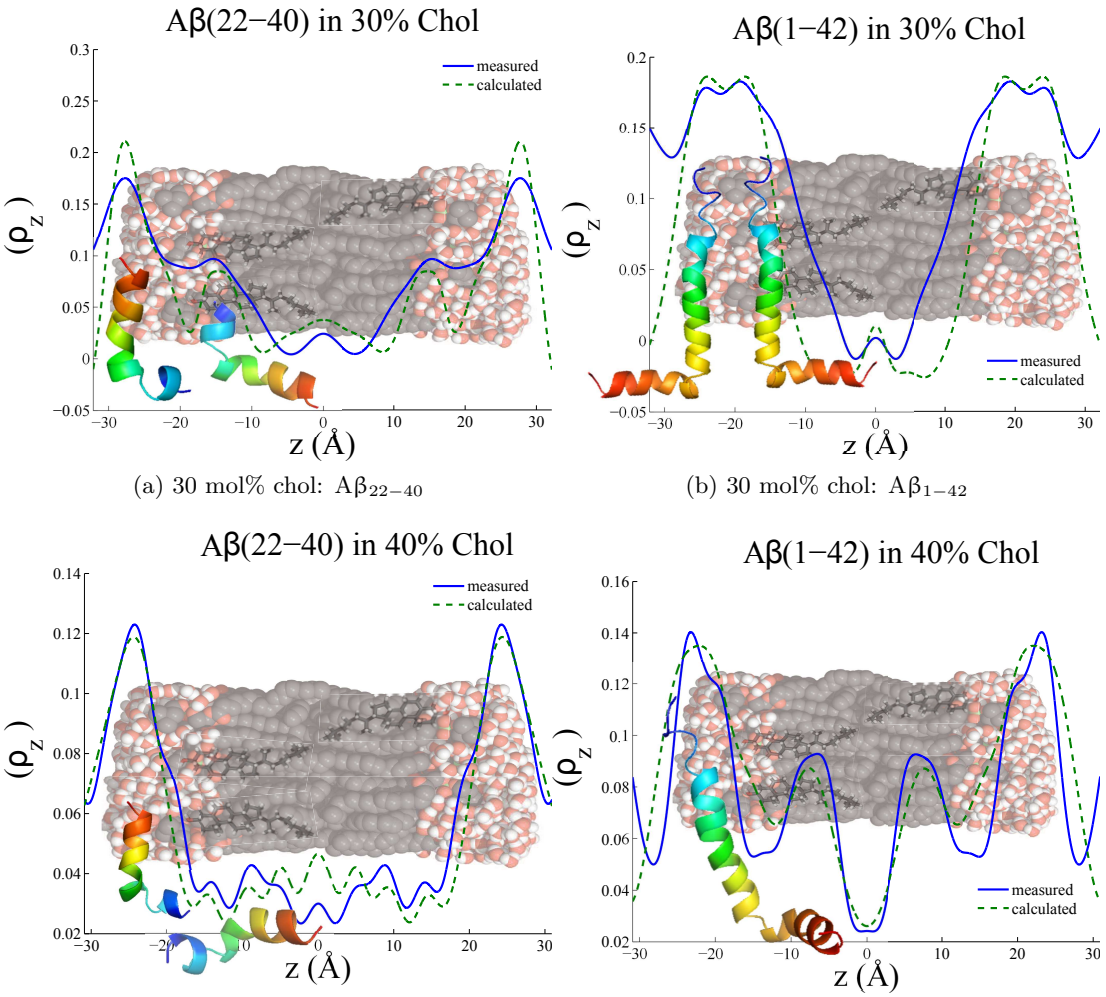

(a) 30 mol% chol: $A\beta_{22-40}$

(b) 30 mol% chol: $A\beta_{1-42}$

(c) 40 mol% chol: $A\beta_{22-40}$

(d) 40 mol% chol: $A\beta_{1-42}$

Figure 4.10: Measured electron density difference between sample with and without peptide (blue solid line) and model calculation (green dashed line) for a) 30 mol% cholesterol with $A\beta_{22-40}$ peptide fragment, b) 30 mol% cholesterol with $A\beta_{1-42}$ full-length peptide, c) 40 mol% cholesterol with $A\beta_{22-40}$ peptide fragment, d) 40 mol% cholesterol with $A\beta_{1-42}$ full-length peptide. Models were calculated by determing the electron density profile of solution protein structures from the protein data bank (reference 1IYT), and determining a feasible orientation in the membrane which resembles the measured electron density.

Position of full-length peptide amyloid-β_{1-42}

The position of the full-length peptide was modelled with the peptide C-terminus end (residues >30) residing in the bilayer parallel to the lipid chains, and the N-terminus laying on the bilayer surface. For the 30 mol% cholesterol sample, two populations were necessary to model the double peak near the water layer. The 40 mol% sample can be modelled with a single peptide population in the unit cell, with the peptide slightly shifted in the bilayer, not embedded as deeply as in the 30 mol% case. This reflects the increased cholesterol content expelling the peptide from the bilayer centre as was discussed in Section 4.1.2.

Also noteworthy is the thinning of the water layer seen for samples with this peptide. Figure 4.6 c) shows a drop in the water layer thickness of the full-length peptide samples between 30 mol% and 40 mol% cholesterol, which is not present for the other samples. It has been shown by using small angle scattering that the full-length peptide may have a fusiogenic effect on the bilayer [23]. It has also been shown that the full-length peptide produces pore-formation [85]. The segment of the peptide which lays on the membrane surface may act via electrostatics to decrease the water layer between membranes and to bring adjacent bilayers close together, as the first step to bilayer fusion or pore formation.

4.2 Conclusions and discussion

Structural disruption, formation of pores and membrane fusion may all be changes in the bilayer which occur and go hand-in-hand to give rise to the neurotoxicity associated with Alzheimer's disease.

The experimental evidence presented in this section, indicating both interaction and intercalation of amyloid-β_{22-40} and amyloid-β_{1-42} peptides into anionic lipid membranes containing cholesterol, supports the hypothesis that the monomeric forms of the peptide may play a role in the origin of symptoms in Alzheimer's disease.

Both peptides embed into a lipid bilayer containing 30 mol% and 40 mol% cholesterol, however the higher cholesterol content prevents deep embedding into the core of the membrane. The full length (1-42) peptide embeds into the bilayer, whereas the fragment (22-40) exhibits two populations, one surface and one embedded. This observation may be related to the two step model of protein insertion into the bilayer, with proteins first coming into contact with the surface, and intercalating if the potential energy barrier is overcome.

Evidence has been provided that both of these peptides increase the solubility limit of cholesterol in the bilayer, preventing the formation of cholesterol plaques. High concentrations of cholesterol are thought to be related to lipid rafts: highly transient, dense lipid patches in the bilayer, which host protein complexes. Lipid rafts may be involved with transport and signalling processes across the membrane, although this hypothesis remains controversial [139, 163, 164, 165, 166]. If the peptide prevents the aggregation of cholesterol, then the protein complexes which require stability to form

may be hindered [13, 24, 167].

It has also been shown that the bilayer *d*-spacing is significantly changed with the presence of peptides, especially at very high cholesterol content. Changes in bilayer structure can be detrimental to sensitive processes such as the processing of amyloid precursor protein (APP) by β- and γ- secretases. In the case that the bilayer is thicker than expected, the secretases may not properly cleave the peptide, resulting in neurotoxic fragments [18, 168, 169].

To compliment the structural measurements presented here, dynamic measurements (with quasi-elastic neutron scattering, for example) would provide further insight into this model system, and the complexities of lipid-peptide interactions in the membrane.

4.3 Notes

- A manuscript containing this work was published in the journal Membranes.
  - **Barrett, M.**, Alsop, R, Hauß, T. and Rheinstädter, M. C., "The position of $A\beta_{22-40}$ and $A\beta_{1-42}$ in anionic lipid membranes containing cholesterol." (2015) Membranes. 5(4):824-43.

5 Humidity chamber as sample environment

As mentioned previously in Section 1.3, the phase behaviour of a lipid bilayer sample can be modified by changing the environment in which it resides. A model lipid membrane is particularly sensitive to humidity and temperature. For biophysics experiments using neutron scattering, fine control of these parameters has been largely hindered by the performance of existing humidity sample environments. In order to advance the experimental potential of neutron experiments, the scientific community decided it was time to develop a new humidity sample environment which would allow for better precision and stability and make experiments more flexible and more efficient.

A cooperation between the Helmholtz-Zentrum Berlin (Berlin, Germany) and the Institut Laue-Langevin (Grenoble, France) was formed in the framework of the NMI-3 JRA-20 project to design and build an improved humidity sample environment for neutron scattering experiments. This project was carried out with three main milestones, which will be discussed in the following sections.

- Overview of existing humidity sample environments and specifications of a new humidity chamber: Section 5.2
- New chamber design: Section 5.3
- Building and commissioning of the new humidity chamber: Section 5.4

5.1 Humidity's role in biological experiments

When planning an experiment involving biological membranes, one important consideration is to measure the sample in a physiologically relevant environment. To produce a sample environment that best replicates *in situ* conditions, one must consider humidity and temperature. The lipid bilayer is very sensitive to both of these parameters and therefore accurate and precise control of both humidity and temperature is crucial.

The phase behaviour of even the most simple single component lipid bilayer is very rich. For a lipid bilayer containing only DMPC, two main lipid phases exist. The *gel* or L_β phase is characterized by a more rigid bilayer with individual lipids having straight tails (all trans-configuration) and well defined distances between lipids which allows for close packing of the lipids. At higher temperatures or higher humidity the bilayer transitions to the *fluid* or L_α phase characterized by more fluctuations in the lipid tails, a looser lipid packing behaviour, faster lipid diffusion and a more flexible bilayer.

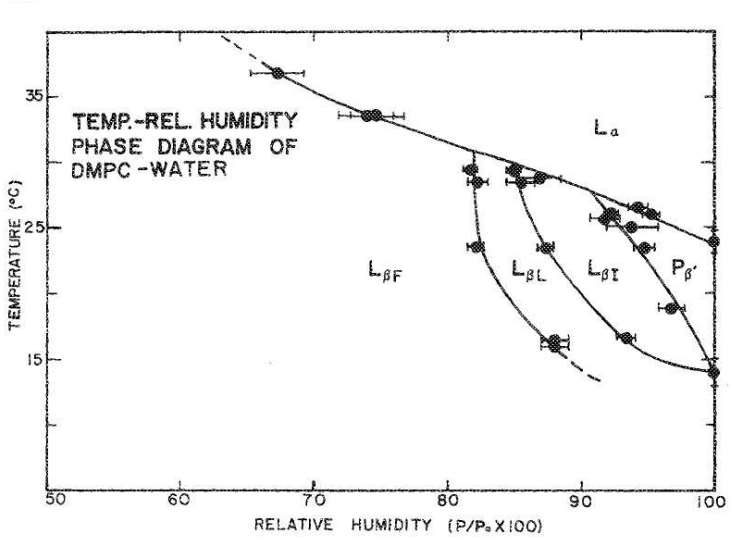

Figure 5.1: Temperature and humidity phase diagram of a DMPC lipid bilayer. From Smith *et al.* [58]

In the single component DMPC bilayer, other gel-like phases also exist, but can be accessed only at high humidity (as seen in Figure 5.1). Smith describes two additional L_β phases which first appear at humidity greater than 80% relative humidity and are characterized by tilted lipid orientations as a result of larger hydration forces. Finally, at humidity levels $\geq$92 % r.H. in DMPC, a ripple-phase, or P'_β is achieved. The ripple phase exhibits a very interesting diffractogram, with peak splitting as a result of ripples in the membrane [170].

Of course, real biological membranes are much more complex than the single component DMPC membrane, and also exhibit unique phase behaviour based on the ratio of bilayer components present. Controlled dehydration has also been used to induce fusion stalks between membranes [171] and to observe the protective effect of sugars against membrane rupture while freezing [172].

Since most biological processes occur under fully saturated hydration conditions, an obvious goal for experimental sample environments is 100% relative humidity. With a fully saturated sample, the model bilayer would behave, both structurally and dynamically, in a manner which is comparable to a natural membrane in excess water. A lipid bilayer stack will slowly take up water with small increases in d-spacing until a very high hydration pressure, where drastic swelling occurs [63, 173] (Figure 5.2). By nearing this thick, fully hydrated state, the lipid behaviour in the bilayer begins to more accurately represent the physiological case. However, this goal of full sample saturation is accompanied by many complications which often prevents a sample environment from reaching 100% relative humidity, including problems measuring the highest humidity with accurate sensors, and cold points in the humidity set-up.

Therefore, humidity sample environments should have the ability to access both the

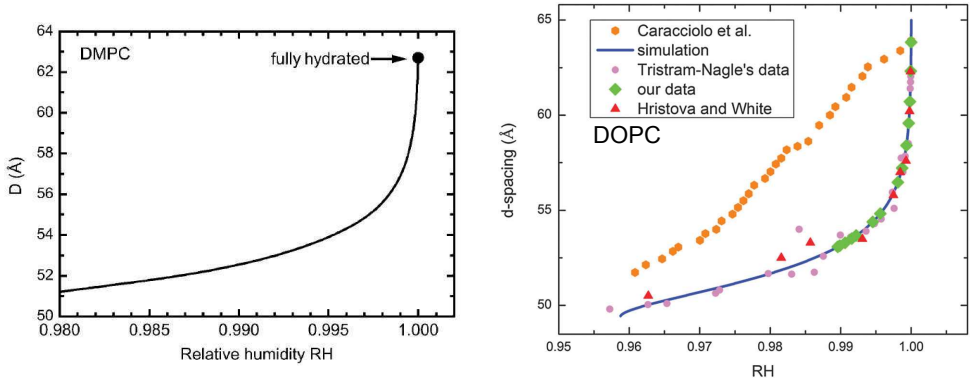

Figure 5.2: Swelling of a DMPC lipid multi-bilayer (left) and DOPC lipid multi-bilayer (right) induced by relative humidity. From Kučerka *et al.* and Ma *et al.*, [83, 173]

rich phase behaviour of the middle humidity range, and to replicate the biologically relevant high humidity region, all while controlling the temperature of the sample. In this chapter, the development, design and commissioning of a new humidity chamber for neutron scattering will be described.

5.2 Humidity control techniques and existing technology

To begin the design process, a survey of existing humidity control techniques was conducted. The existing humidity set-ups were compared, and a plan to develop a new chamber was made. In the following sections, each humidity control technique is discussed and compared to the end goal of accurate humidity control over a wide range of humidity while maintaining high temperature stability.

5.2.1 Bulk water

The most straightforward technique to reach a saturated (fully hydrated) lipid bilayer sample is through the use of bulk water. The sample is directly exposed to excess water, resulting in fast bilayer swelling [174, 175, 176, 177]. Although this technique is simple and works exceedingly well to achieve saturation, it is also has some large limitations. For example, an excess water environment may result in a loss of sample material. This is especially true for charged lipids, which are susceptible to dissolving in water. A charged lipid bilayer will disassociate from the substrate on which it was deposited, losing the very order and structure which is of interest in a scattering experiment. This is a problem due to the prevalence of charged bilayer lipids in biological systems [175, 178, 179].

Even if the system of interest is an uncharged lipid bilayer and is stable under excess water conditions, this technique has another drawback. The coherent and incoherent

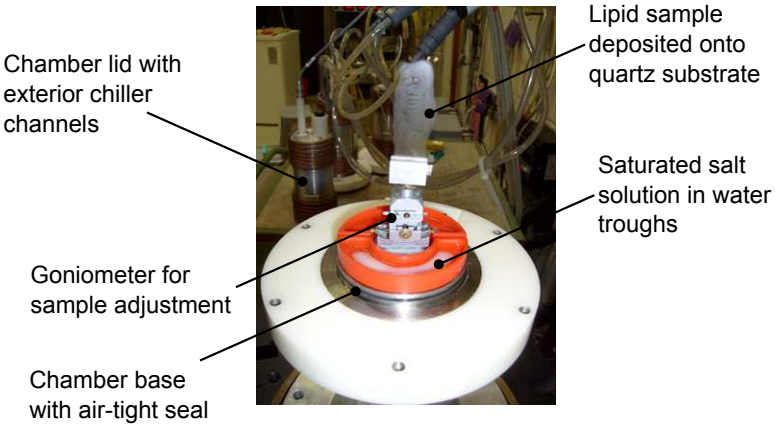

Figure 5.3: Typical saturated salt humidity chamber. Photo courtesy of Thomas Hauß, V1, HZB.

scattering signals from water are quite strong due to the large magnitude of neutron scattering lengths from hydrogen and deuterium (see Tables 2.3 and 2.5). Therefore, allowing the neutron beam to pass through a thick excess water layer results in a poor signal to noise ratio, as well as in unwanted scattering coming from the water. This can be avoided by using the bulk water set-up primarily in reflectometry geometry, allowing the neutrons to pass through a substrate with high transmission (e.g. Si), and avoiding scattering through water [179].

5.2.2 Saturated salt

Humidity control through a saturated salt solution is one of the most commonly used techniques. The principle behind this control technique is to limit the amount of water vapour in a closed container by modifying the exchange rate between liquid water and water vapour at a reservoir's surface. The addition of salt to the water reservoir decreases the probability that water at the surface will dissociate and enter the vapour phase. To make this technique robust, salt is added until it reaches saturation, forming a slushy mixture, rather than carefully measuring the salt and water ratio. The desired chemical potential, and thus relative humidity above the water surface is achieved with high accuracy (an example of such a humidity chamber is shown in Figure 5.3).

Many different salts have a characteristic humidity associated with their saturated state and are well characterized in a series of tables [180, 181, 182] (a selection of commonly used saturated salt solutions is listed in Table 5.1). However, this generates a non-continuous range of humidity values, with gaps occurring for humidity values that are not associated with any particular salt. The saturated salt solution technique is also labour intensive and relatively slow. When setting a new humidity, one must open an air-tight sample container, carefully clean the reservoir of all salt from the previous measurement, refill the reservoir with the new salt and wait for the sample to achieve the new desired hydration. This makes multiple chambers and multiple

Table 5.1: Relative humidity of commonly used saturated salt solutions at 20, 30, and 40°C [183].

	r.H. at 20°C	r.H. at 30°C	r.H. at 40°C
LiCl	11.3 ± 0.3	11.3 ± 0.2	11.2 ± 0.2
$MgCl_2$	33.1 ± 0.2	32.4 ± 0.1	31.6 ± 0.1
$Mg(NO_3)_2$	54.4 ± 0.2	51.4 ± 0.2	48.4 ± 0.4
NaCl	75.5 ± 0.1	75.1 ± 0.1	74.7 ± 0.1
KCl	85.1 ± 0.3	83.6 ± 0.3	82.3 ± 0.3
KNO_3	94.6 ± 0.7	92.3 ± 0.6	89.0 ± 1.2
K_2SO_4	97.6 ± 0.5	97.0 ± 0.4	96.4 ± 0.4

samples necessary during a time-limited experiment. In particular, when determining the Fourier phase coefficients of the sample, it is necessary to expose each sample to a series of different D2O/H2O ratios (minimum three for a centro-symmetric unit cell), further increasing waiting time, and potentially wasting neutron beam-time.

Since no special infrastructure is used (other than the presence of a water reservoir, which is also necessary for other techniques), saturated salt can be used in most humidity chambers. This technique is also suitable for reflectometry experiments, and the bulk-water chamber from Harroun *et al.* [179] also uses a saturated salt set-up for an indirect sample hydration.

Based on the discontinuous accessible humidity range, and the tedious multiple sample changes necessary while using this technique, it was decided against further pursuit of this technique for humidity control.

5.2.3 Gas vapour flow

A much quicker variant is the gas vapour flow technique. This technique involves two mass flow controllers regulating dry and humid gas flow. The two controllers are fed by a common gas source, typically compressed air or nitrogen, which gets split into two paths, passes through the mass flow controllers and is then either dried or hydrated. One gas passes through a desiccant, resulting in a stream of dry gas, while the other bubbles through water, keeping this stream near saturation. The rate of flow from each line is controlled by a feedback loop to a humidity sensor located in the vicinity of the sample. The sample environment then quickly reaches a constant humidity value, and the sample takes up the water from the atmosphere. Of the non bulk-water humidity control methods (saturated salt and temperature controlled), gas vapour flow is substantially faster than the other methods, with the only limiting factor being the rate at which the sample takes up the water.

The existing gas vapour flow set-ups work reliably for a continuous range of humidity from very dry (defined by the desiccant, typically $\sim$ 10 % relative humidity) to approximately 95% relative humidity [171, 184]. The upper limit arises from two sources: 1) small temperature gradients in the system, and 2) the range of the best

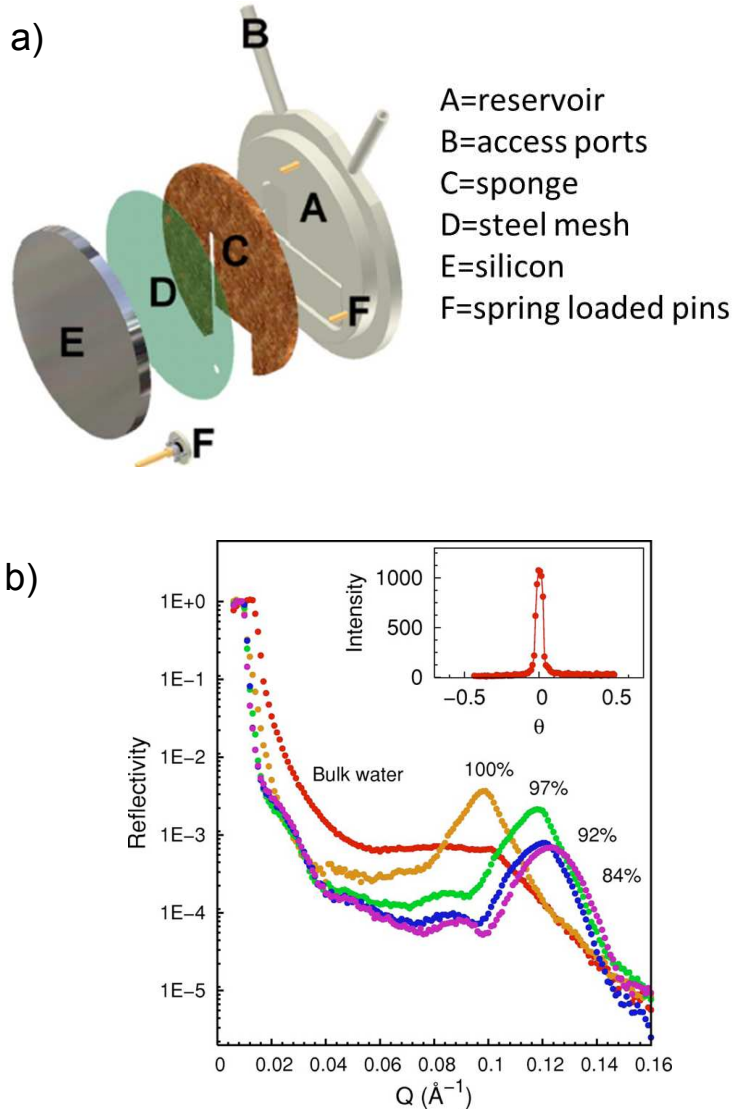

Figure 5.4: a) The DMPC lipid bilayer reflectivity bulk-water/saturated salt chamber. b) First order reflections gathered while using the reflectivity chamber. The peak shifts to lower-Q (large real-space values) with higher humidity, and is lost to bulk water. From Harroun *et al.* [179]

humidity sensors available. Small changes in temperature along the tubes where the very humid vapour travels result in condensation points. Condensation at a cool point in the system draws the vapour away from the sample. For example, for a sample at 30°C close to 100% r.H., a gradient of ∼50 mK can reduce the desired humidity by 3% (calculated using the Antoine equation 5.1). By insulating the entire set-up against small temperature variations this can be mitigated. The larger problem comes from

the performance of available humidity sensors. Of the humidity sensors which are of suitable size for a humidity sample environment, the measurement uncertainty above 90% relative humidity becomes large. The best resistive or conductive sensors available are rated to an uncertainty ±2-3% r.H. for the high humidity range. In practice, above ∼95% r.H., most sensors begin to indicate full saturation, and cannot be used to regulate a feedback loop.

Although the gas vapour flow method is fast, and provides a continuous range of accessible humidity, the limitations which exist for the high humidity range have left only the temperature control technique as a technique worth pursuing.

5.2.4 Temperature control

The relative humidity in a system can also be induced by controlling the partial vapour pressure through precise control of sample and reservoir temperature [173, 185]. Instead of keeping the entire system at a fixed temperature and regulating the partial pressure with a saturated salt solution, a similar effect can be achieved by cooling pure water in a reservoir and heating the sample. By lowering the temperature of the water reservoir a lowered partial vapour pressure $p_{reservoir}$ is provided to the system, resulting in less water vapour in the air, as in equation 5.2. The vapour pressure can be determined directly from temperature using the Antoine equation [186], Equation 5.1, with vapour pressure p, temperature in Kelvin and A, B, C constants unique to the liquid/gas system. For water between 1°C and 100°C, A=5.402, B=1838.7 (K), C=-31.7 (K) [187].

$$log_{10}p = A - \frac{B}{C+T} \tag{5.1}$$

This method allows a continuous range of relative humidity with the possibility of fast changes in humidity using temperature controllers. Although the change of humidity is not as quick as in a gas-flow system, a humidity change is significantly simpler than the saturated salt technique, as opening and replacing the water is not necessary. This technique has been used to create chambers which can achieve high relative humidity, or a range of humidity [173, 185]. The temperature control technique solves the problem of inaccurate humidity sensors above 95% r.H. by relying instead on thermometers with high accuracy. The drawback of this method is the requirement for an environment with extreme temperature homogeneity. As already mentioned in the gas vapour flow technique, a temperature gradient resulting in a cold spot in an undesired location creates a condensation point and, in principle, a new water reservoir of an uncontrolled temperature, typically lower than the desired temperature. However, an effective insulation of the humidity chamber can significantly suppress the influence of temperature gradients.

$$r.H. = \frac{p_{reservoir}}{p*_{sample}} \tag{5.2}$$

This method allows both mid- and high-humidity to be achieved as well as the

advantage of fully automated humidity control, independent of inaccurate humidity sensors. The one downside to this technique is the fact that small temperature gradients may make it difficult to reach the highest humidity values, which is a problem faced by both the gas vapour and temperature control techniques. Great care must be taken to suppress any cool spots in the chamber.

5.3 Development of the BerILL humidity chamber

With this survey of existing humidity chamber technology, the decision was made to pursue the temperature controlled humidity control technique. The geometric limitations (maximum diameter of chamber, dimensions of neutron beam, beam height) were taken into account, such that the chamber would be compatible with a large range of diffraction and reflectometry instruments at various neutron scattering facilities. Slight variations made to this design would also allow compatibility with small angle and quasi-elastic set-ups.

5.3.1 Initial design

The initial design was sketched out during a meeting at the ILL. The preliminary design is shown in Solidworks 3D render in Figure 5.5. This design was finalized using the SolidWorks computer assisted drawing program [188]. Heavy focus was placed on thermal insulation between three sections of the chamber, to insulate the inner chamber from the external temperature, and to insulate between the upper chamber (the location of the sample) and the lower chamber (the location of the water reservoir). Fluctuations in the external (room) temperature should have no effect on the inner chamber, and the inner chamber's upper (sample) section should also be thermally insulated from the lower (reservoir) section.

An insulating vacuum was used to decouple the inner and outer chambers, with all connections between the inner and outer chambers made of thermally insulating material (stainless steel or plastic). These connections are also further shielded by the chiller channels which circulate tempered fluid through the chamber.

Finite element simulations and modifications to initial design

Before this design was physically produced, a series of finite element simulations were performed using the *COMSOL Multiphysics* modelling software [189]. In order to simulate the equilibrium state of the chamber with a variety of external and internal temperature conditions, the heat transfer module was used. These simulations were carried out on the imported Solidworks CAD as well as a simplified radially symmetric model of the inner chamber. The latter allowed for parametric sweeps of various aspects of the chamber geometry, while keeping the simulation time reasonable (tens of minutes rather than hours per parameter change).

The finite element treatment involves separating a geometric problem into manageable *finite elements*. For each element (a small volume of the geometry), a

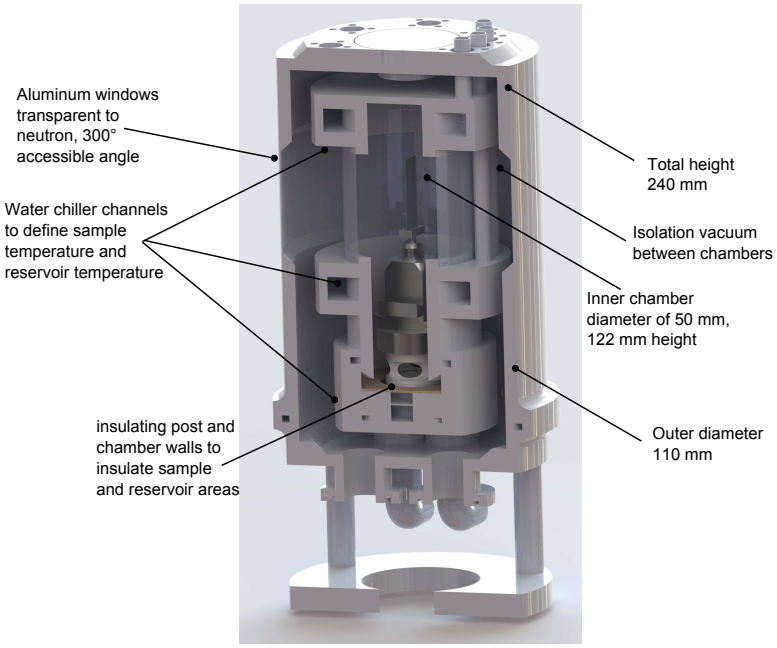

Figure 5.5: The first version of the design in Solidworks. Design by M. Barrett, D. Wallacher and A. Perkins.

set of partial differential equations is solved, ensuring that the boundary conditions of all neighbouring elements agree, while minimizing the global error function.

In these simulations, *Fourier's law of heat conduction* (Equation 5.3) is solved in the equilibrium case, where $\vec{q}$ is the local heat flux, k is the thermal conductivity, A is the cross-sectional area and ∇T is the spatial temperature gradient.

$$\vec{q} = -kA\nabla T \tag{5.3}$$

The first step to a simulation is assigning material properties to each of the chamber pieces. The density, thermal conductivity and any fixed temperatures are given in this step. We assumed all surfaces of the chiller channels were fixed temperatures.

Next, the geometry is split into a mesh of finite elements (see Figure 5.6). It is necessary to make the mesh fine enough to capture small temperature effects, but not so small that the geometry is over-defined and a simulation takes unnecessarily long to perform.

With all material properties of the components defined and a working mesh in place, the simulation calculates the equilibrium temperature of each element of the system. A series of water reservoir and sample chiller temperatures were simulated, to determine the influence of different temperatures in the system (from 60%-100% relative humidity and from 10°C-40°C).

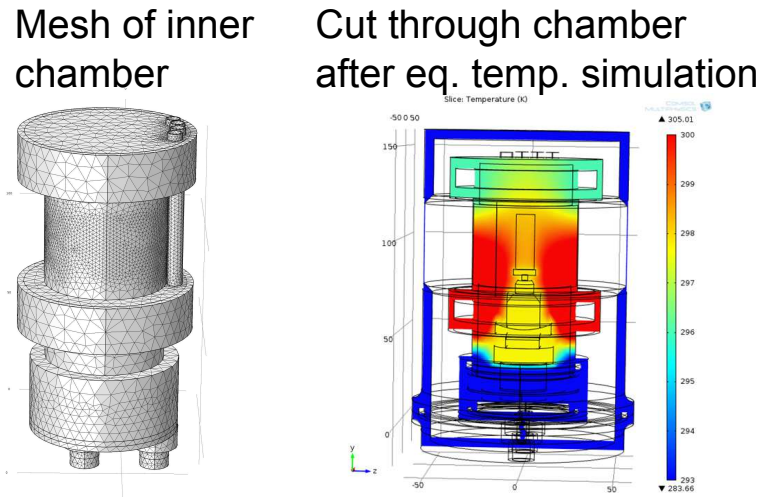

Figure 5.6: A working mesh of the inner humidity chamber (left). Temperature distribution in a vertical planar cut of the chamber after a simulation (right).

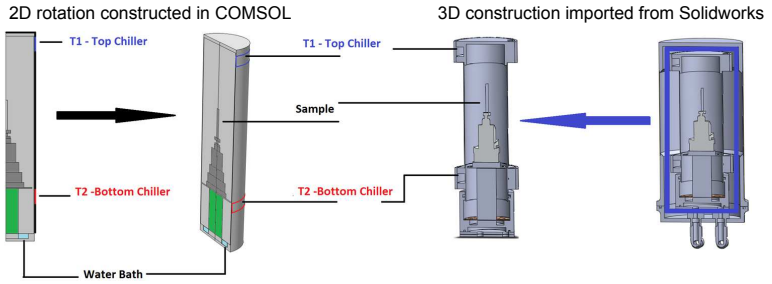

Figure 5.7: A 2D rotationally symmetric slice (left) is used to recreate the 3D model (right).

5.3.2 Radially symmetric simplification in COMSOL

The first simulations on a 3D model directly imported from the Solidworks CAD produced results which made physical sense, but lasted a few hours for each simulation. The geometry was simplified by recreating a version of the inner chamber directly in COMSOL (see Figure 5.7), defining all dimensions with equations, relative to other parts of the chamber. This allowed for geometric parameters to be defined through mathematical relations, giving the freedom to perform parametric sweeps through different geometries. The simplified model was a radial slice of the inner chamber, which is later rotated 360° to represent the 3D volume (as shown in Figure 5.7). This simplification reduced the simulation time to ∼5 minutes per simulation.

The results of a series of temperatures simulated with the radially symmetric geometry were compared with results from the 3D (SolidWorks imported) simulation (Figure 5.8), capturing the details of the more complex temperature profile.

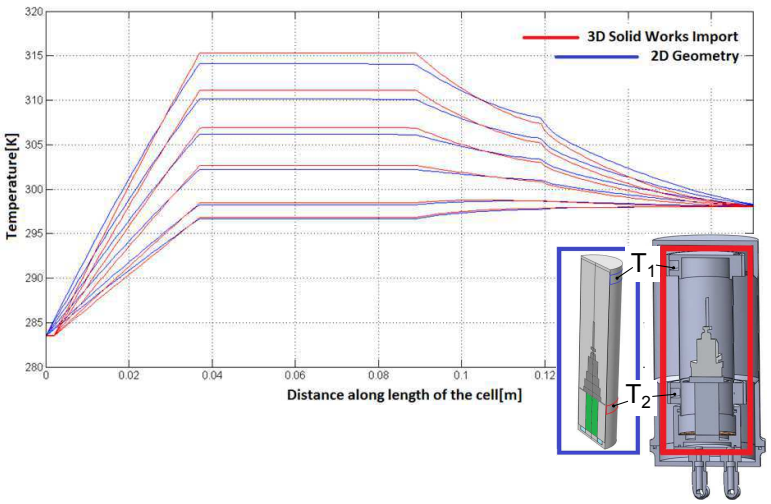

Figure 5.8: A comparison of the temperature from the bottom (d=0 m) to the top (d=0.16 m) of the inner chamber. The water bath temperature and upper chiller (T1) were held at 284 K and 298 K, respectively, while the middle chiller (T2) was varied between 297 K and 316 K. The 2D rotation captures the trend, with variations due to the simplification of the goniometer and rotation extrusion of the sample.

A series of parametric studies were carried out to determine what aspects of the design should be modified or improved: including changing the height of the chamber, the position of chillers and the shape of the sample post. The most striking modification was to the position of the T2 (middle) chiller. Having this chiller too close to the lower edge of the sample substrate (see Figure 5.9) resulted in a loss of the shielding effect this chiller between the water reservoir and the sample.

On the other hand, positioning the T2 chiller too low caused the water bath surface temperature to rise (Figure 5.10).

From these parametric simulations, the decision was made to lengthen the chamber as much as possible vertically, and have the T2 chiller located at the same height as the goniometer base.

Furthermore, to decouple the upper and lower sections of the inner chamber, instead of stainless steel (thermal conductivity $\sim$16 $W/(m \cdot K)$ [190]) as originally planned, the sample post and gliding seal ring were instead made with PEEK (polyether ether keytone, thermal conductivity 0.25 $W/(m \cdot K)$ [191]). This material greatly suppresses heat transfer from the bottom to the top of the chamber through the chamber walls and sample post. An additional heater was also included directly underneath the goniometer, to further shield the goniometer from the water reservoir.

With this series of modifications, the CAD was updated, and another round of simulations on the imported 3D geometry were performed (see Figure 5.11).

The final drawings were manufactured and the first tests and commissioning were

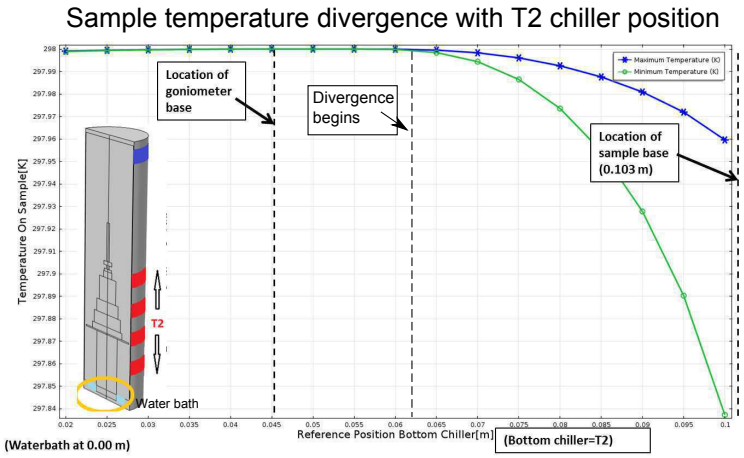

Figure 5.9: The sample high and low temperature values during a series of simulations varying the vertical position of the middle chiller (T2). The T2 and T1 (top) chiller were set to the same temperature (298 K), and the water reservoir at 283 K. At ∼2 cm above the goniometer base, the shielding effect of the T2 chiller starts to become less effective, and the maximum and minimum temperature points on the sample begin to diverge.

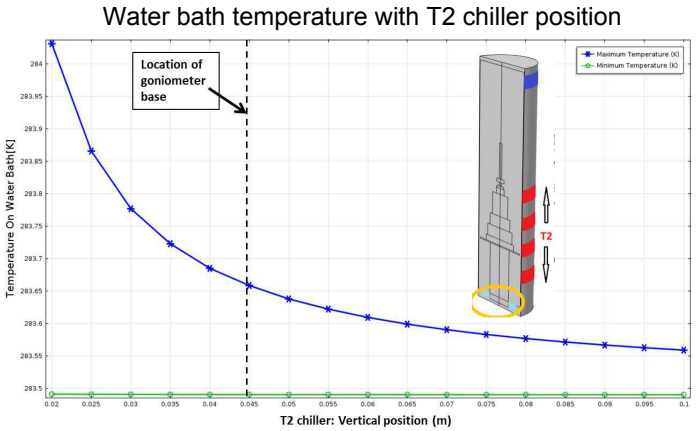

Figure 5.10: The water reservoir high and low temperature values during a series of simulations varying the vertical position of the middle chiller (T2). The T2 and T1 (top) chiller were set to the same temperature (298 K), and the water reservoir at 283 K. At the lowest T2 chiller position (2 cm from the water surface), the water surface temperature diverges by ∼0.5 K.

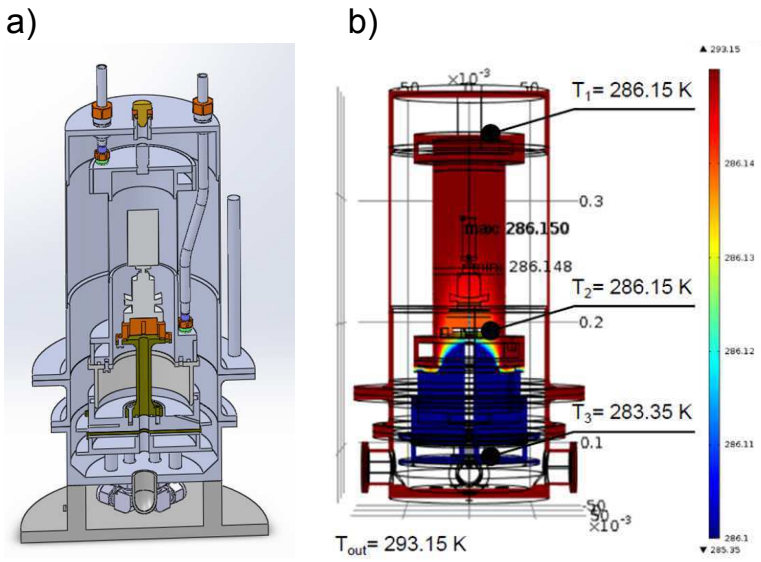

Figure 5.11: a) The modified chamber design: an elongated upper chamber, insulated from the lower chamber with PEEK plastic and an additional heater under the goniometer. b) COMSOL finite elements simulation of modified chamber, with upper chamber chillers at 286.15 K, water reservoir chiller at 283.15 K. The temperature difference over the sample is ∼2 mK.

performed in the Fall of 2014 at HZB, and in December 2014 on the D16 diffractometer at the ILL.

5.4 Commissioning of the BerILL humidity chamber

The parts of the chamber were manufactured by HZB and ILL and assembled in Berlin (Figures 5.12 and 5.13).

The entire set-up is shown in Figure 5.14. All controllers and sensors were integrated into a LabView [192] interface prepared by Nico Grimm [193]. The setup is listed below

- 10 Omega high performance thermometers
- 4 Lakeshore 350 temperature controllers [194]
- 2 Kapton heater foils (one below water reservoir, connected via weak-link, one under the goniometer) to remove thermal fluctuations
- 1 pressure sensor (to check for vacuum leaks)
- 1 humidity sensor (Honeywell HIH-4000, to check humidity equilibration time of the chamber)

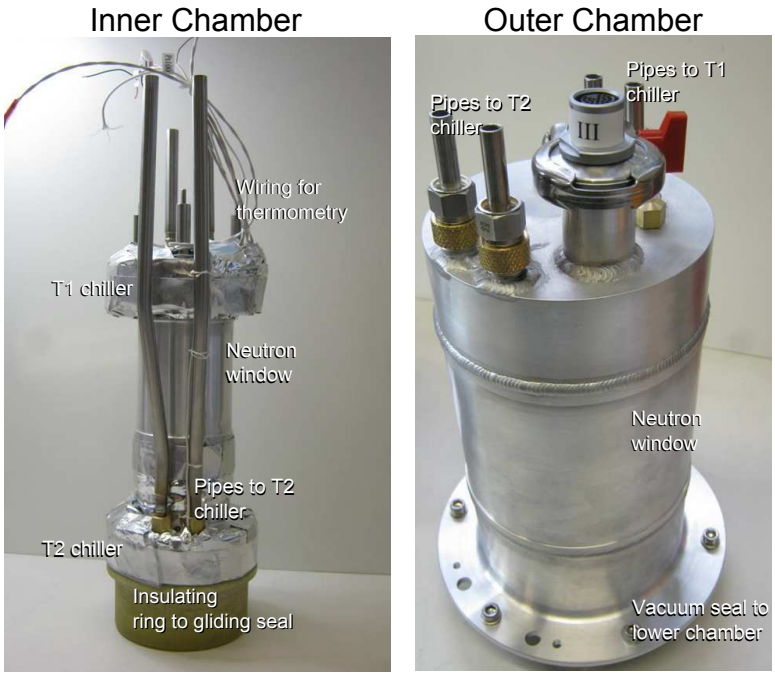

Figure 5.12: The inner (left) and outer (right) sections of the chamber lid, based on the design presented in Figure 5.11.

- 2 Julabo Presto A30 temperature control systems [195], regulated by external thermometers embedded in the chamber
- 1 vacuum turbo pump, for insulation between inner and outer chambers

The tests of the chamber in the neutron beam were done at the ILL on the D16 diffractometer (ILL) and the V1 membrane diffractometer (HZB). Existing humidity sensors which can fit into a chamber of this size are not accurate at relative humidity above 95%. This fact necessitates another high humidity observation method. The dramatic swelling behaviour of lipid membranes at high humidities is an excellent indicator of relative humidity close to full saturation. This behaviour is well characterized for commonly used single component lipid bilayers (discussed in detail in Section 5.1). By observing the shift of peak-position with a diffraction experiment , the d-spacing (lamellar repeat distance) can be calculated using Bragg's law 2.3.

Figure 5.15 shows the 2θ projection (x-axis) of the detector image as it changes in time (y-axis). The reservoir reaches its temperature setpoint in 30 minutes. One hour after the set-point was changed, a small fraction of the membrane has reached the sufficient hydration level to transition to the fluid phase (indicated by the right peak of the paired Bragg reflections). Four hours after the setpoint change, the majority of the sample has reached the fluid phase, with only a faint signal from the gel phase remaining. This phase transition arises from water coming into contact with the

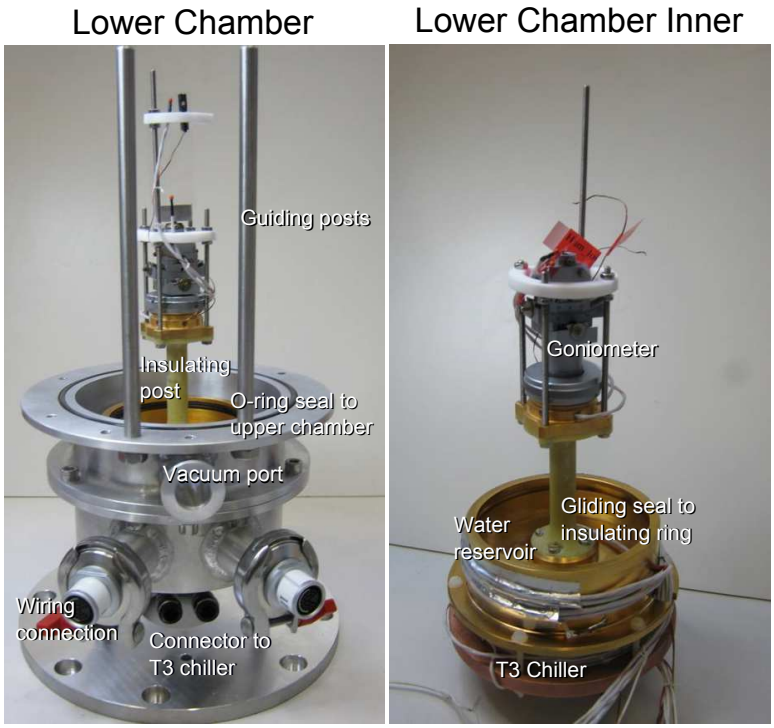

Figure 5.13: The complete chamber base (left) and the inner section of the chamber base (right), based on the design presented in Figure 5.11.

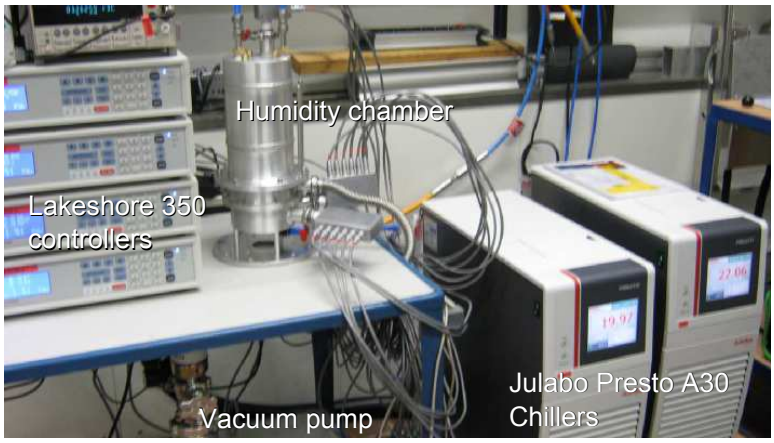

Figure 5.14: The complete humidity chamber set-up.

head-group section of the membrane. Increasing the hydration between bilayers allows for the bilayer to fluctuate more. Eventually, enough fluctuations exist that the forces holding carbon-carbon bonds in the lipid tails in all trans-state give way to "kinks", resulting in a smaller d-spacing, and thus higher angle Bragg reflections.

The design allows one to capture the phase transition of the bilayer sample. This gave us confidence that the physical principle of the chamber works for this type of sample, and also gave an estimation of the rate which the chamber and sample equilibrate.

It was not, however, possible to observe the extreme swelling which starts to occur above 98% relative humidity. Due to problems with the insulation vacuum (which could only achieve 10^{-3} mbar) and due to temperature gradients, the chamber could reach a maximum of 95% relative humidity.

5.4.1 Modifications and improvements after the first neutron experiment

A series of modifications on the chamber were performed, including a re-calibration of all thermometers, better insulation of the tubes running from the Julabo Presto chillers to the chamber, re-locating the connection between the T1 and T2 chillers inside the vacuum insulation to avoid a temperature difference between T1 and T2 and improving the internal gliding seal and the sealing around the piping of the upper chamber.

These improvements removed a difference of approximately 50 mK between the T1 and T2 sample chillers, and resulted in a one order of magnitude improvement in the vacuum (10^{-4} mbar). When considering the mean free path of the air molecules (Equation 5.4) this one order of magnitude improvement has a considerable effect. The mean free path defines how far a particle will travel before colliding with another, based on the particle density. A rough calculation shows that from 10^{-3} mbar to 10^{-4} mbar results in a path length change from 6 cm to 60 cm, which is now substantially larger than the dimensions of the vacuum chamber. Collisions are minimized, and thus heat transfer from the inner to outer chamber is suppressed.

$$\bar{l} = \frac{k_B T}{\sqrt{2}\pi d_m^2 P} \tag{5.4}$$

Where $\bar{l}$ the mean free path length in m, k_B Boltzmann's constant in J/K, d_m the average particle diameter, and P the pressure in Pascals.

A second prototype chamber was produced (BerILL 2.0, Figure 5.16) with a simplified chamber design and improved sealing is currently in commissioning at the ILL, for experiments which require an environment up to 98% relative humidity.

5.4.2 Off-line tests and mid-range humidity

Using the BerILL 2.0 prototype, the speed of equilibration of the chamber was tested off-line for a variety of temperature and relative humidity conditions, in the mid-humidity range (50%-70% relative humidity) with a calibrated humidity sensor. Humidity steps of 10% relative humidity were made with the sample at a constant temperature of 20°C, by ramping the water reservoir temperature up. The water

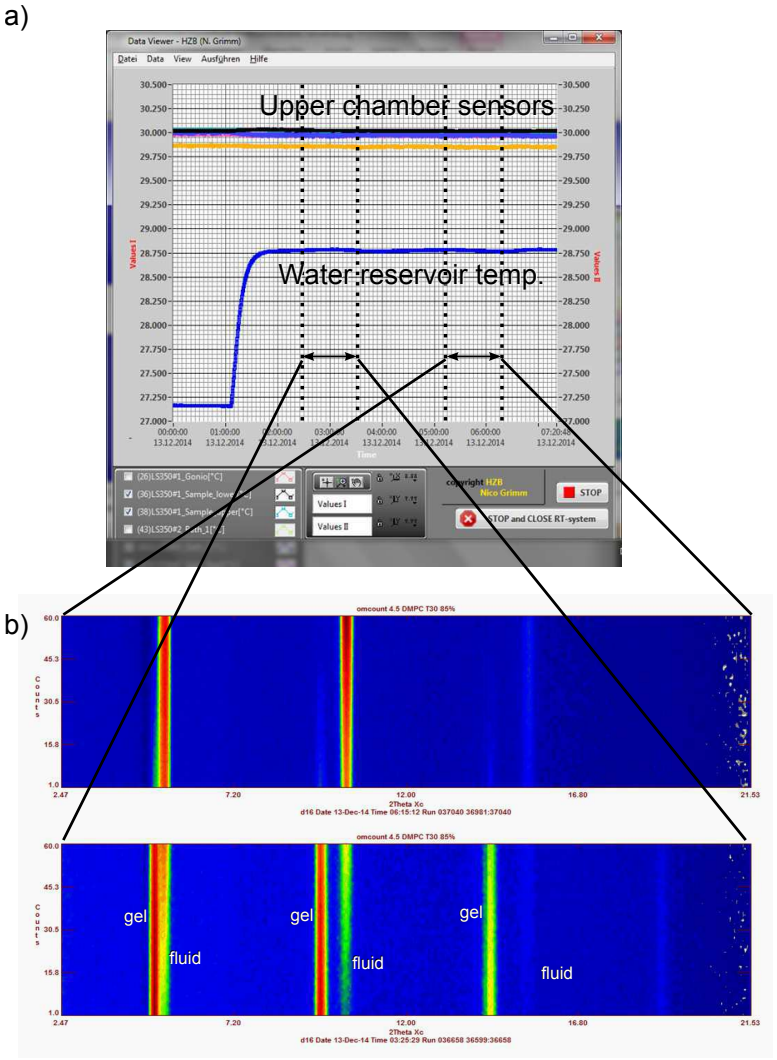

Figure 5.15: a) Labview data viewer program showing a sample held at constant 30°C and the water reservoir rising from 27.25°C to 28.75°C, relating to 85% and 93% relative humidity. b) Projection of detector image onto 2θ axis, plotted every minute for 60 minutes starting at 1 hour, 15 minutes after reservoir temperature change (bottom), and at 4 hours, 5 minutes after reservoir temperature change (top). The paired peaks are labelled gel or fluid, accordingly.

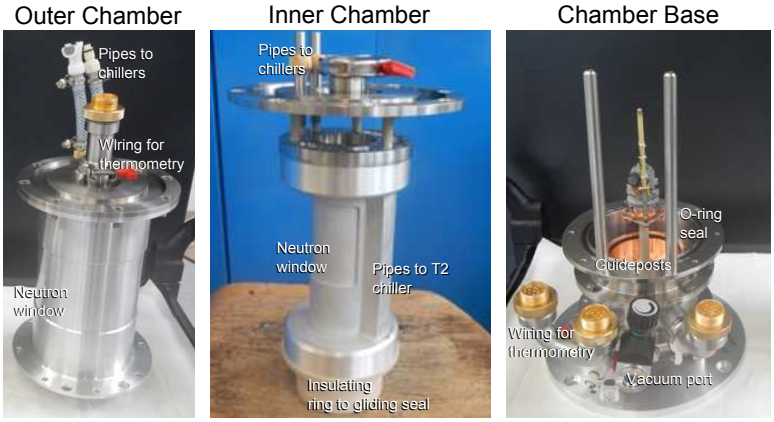

Figure 5.16: The BerILL 2.0 humidity chamber, currently in commissioning at the Institut Laue-Langevin.

reservoir temperature reaches the desired temperature within ∼10 min., but the humidity is slower to react. The desired humidity is achieved in 2-3 h, with a slower response for higher desired humidity (see Figure 5.17).

A similar series of tests was also performed with a constant humidity step (from 60% to 70% relative humidity) at constant sample temperatures of 20°C, 40°C and 50°C (see Figure 5.18). Higher sample temperatures resulted in faster response (closer to 2 h), whereas the 20°C needed ∼3 h to reach equilibrium.

To decrease the time necessary to reach equilibrium, the water reservoir temperature can be overshot. A series of tests were performed to see the effect of overshooting the temperature (see Figure 5.19). This can be useful for experiments when the sample is robust, to bring the sample to equilibrium in a short amount of time. The equilibrium humidity condition can be reached in as little as ∼1 h.

It is important to note that the response of the chamber may not be a good indication of the response of the sample. Lipid samples may react much slower than the chamber itself. For experiments with the humidity chamber, one should ensure that the sample itself has reached an equilibrium before starting a measurement.

The HZB version of the chamber (BerILL 1.0) is available for user service at the time of writing this thesis. The first users have already successfully measured graphene monolayers under varying hydration levels through humidity on the V1 diffractometer in the 30% to 90% relative humidity range.

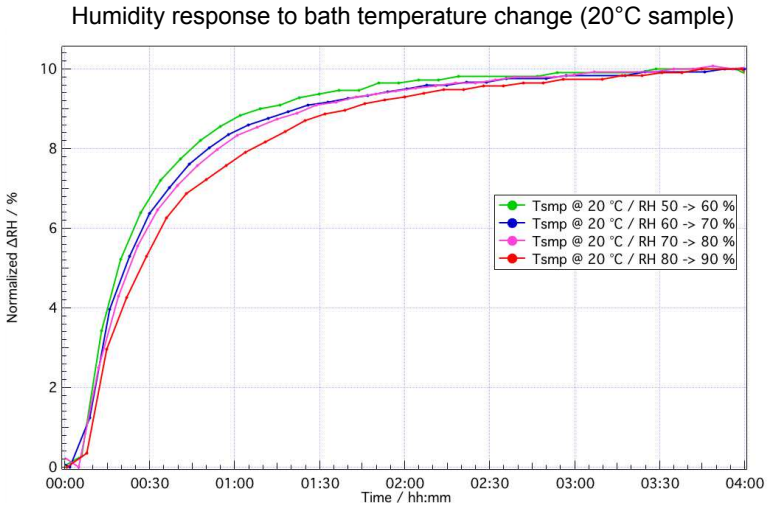

Figure 5.17: Humidity steps of 10% relative humidity, with a constant sample temperature of 20°C. It takes ∼2-3 h to reach the desired humidity equilibrium.

5.4.3 High humidity range

Both prototypes were tested again at HZB and ILL on V1 and D16, respectively. With the improvements which were made, a maximum d-spacing of only ∼52.3 Å could be achieved in a DMPC sample at 30°C (see Figure 5.20) relating to ∼99% relative humidity, even with the water reservoir and sample set to the same temperature (nominal 100% r.H.).

Three hypotheses were developed to explain the upper limit of 99% relative humidity shown in Figure 5.20.

- An unknown cold point in the chamber was preventing the vapour from reaching the sample (the difference between 99% and 100% relative humidity at 30°C is only 170 mK (Equation 5.1))
- The massive brass goniometer containing many small channels and moving parts is acting as a porous system, the water is drawn first to the goniometer before the sample
- A lack of temperature gradient between the bottom and top sections of the chamber causes the air to remain stationary, no vapour exchange between top and bottom of inner chamber

The thermometry in the system does not indicate such a drastic cold point, although due to difficulties in measurement on non-conductive materials (plastic insulation) there may be an effect present. It has been shown by other groups attempting to achieve high humidity that vertical samples are difficult to deal with, due to slight

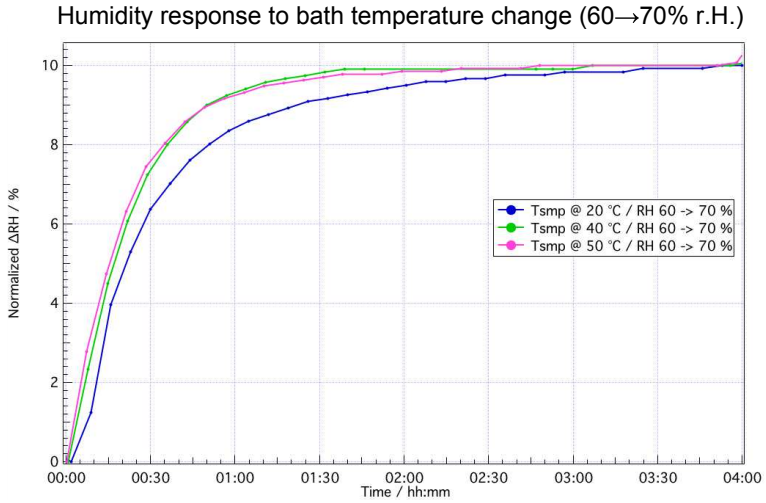

Figure 5.18: Humidity steps from 60% to 70% relative humidity at constant sample temperature of 20°C (blue), 40°C (green) and 50°C (pink).

gravitational effects. This is unavoidable, as the neutron instruments for which this humidity chamber will be used are all vertical sample geometry.

With these hypotheses in mind, a high-humidity sample holder was developed, to reach the remaining 1% humidity level and achieve 100% humidity on the sample.

5.4.4 High humidity sample holder

A high humidity sample holder was designed for achieving humidities above the 98% level. This sample holder is used in place of the standard goniometer. A Peltier element is mounted on the sample holder to provide local cooling directly on the sample's substrate. By cooling the substrate, the water vapour is drawn to the sample. The high humidity sample holder can be seen in Figure 5.21. The sample holder is made primarily of aluminum, allowing fast thermal equilibration. A post made of PEEK plastic is used for mounting, which instills thermal insulation between the sample and the reservoir.

The Peltier elements work via the thermoelectric effect, an applied voltage across a thermoelectric device that creates a temperature difference. In our sample holder, two Peltier elements are clamped between two thermally decoupled massive aluminum blocks. The aluminum block in which the sample is mounted is in contact with the cold side of the Peltiers, and the heat-exchanger is in contact with the hot side. Two thick copper wires create a bridge between the heat-exchanger and the copper block under the sample holder. This copper block is in good contact with the T2 chiller, connected with four copper wings. The high flux of the Julabo chillers is enough to compensate for the small amount of heat the Peltier creates. The heat exchanger acts to remove the heat from the proximity of the sample, otherwise the air around the sample will heat faster than the Peltier can remove heat. In this setup, the Peltier can run with

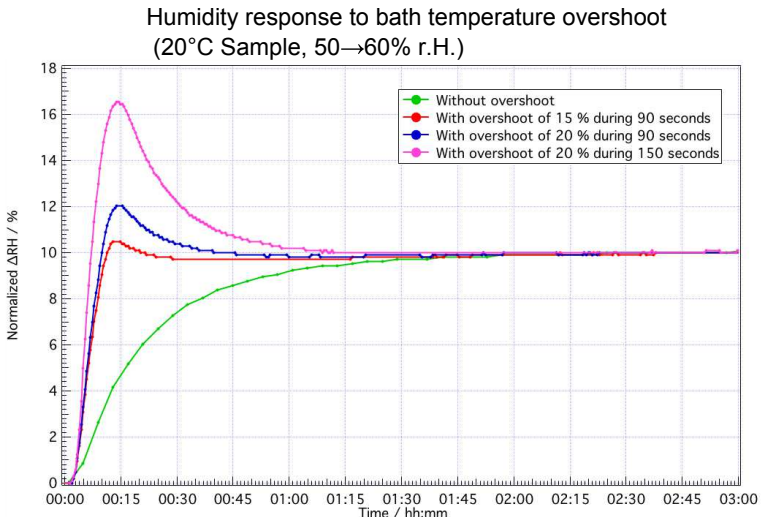

Figure 5.19: Humidity steps from 50% to 60% relative humidity with a constant sample temperature of 20°C. By overshooting the water reservoir temperature, the equilibrium rate of the chamber is decreased.

a maximum of 0.35 W (higher than this power will produce more heat than can be removed by the heat-sink bridge).

For these experiments, a DOPC bilayer sample was used instead of the DMPC used up to this point. This choice was made as DOPC begins drastic swelling at a lower humidity, allowing us to characterize the swelling more precisely (see Figure 5.2).

The DOPC bilayer swells drastically with the Peltier addition, up to 64 Å, the theoretical hydration d-spacing maximum of DOPC (see Figure 5.23). At this point in time, a peak splitting above 59 Å occurs (relating to ∼99.9% relative humidity) seems to indicate two domains in the sample, resulting in two defined d-spacings. This may arise from operating the two Peltier elements as if they were exactly identical. If the internal resistance of one Peltier is slightly lower, it would be possible that the top of the sample is cooled a few mK more than the bottom, causing this phase separation. Further tests are in progress at V1 at HZB to determine the cause of this behaviour and to test possible solutions.

5.5 Notes

- This project has received funding from the European Union's 7th Framework Programme for research, technological development and demonstration under the NMI3-II Grant number 283883.

- A manuscript containing this work is currently in preparation.

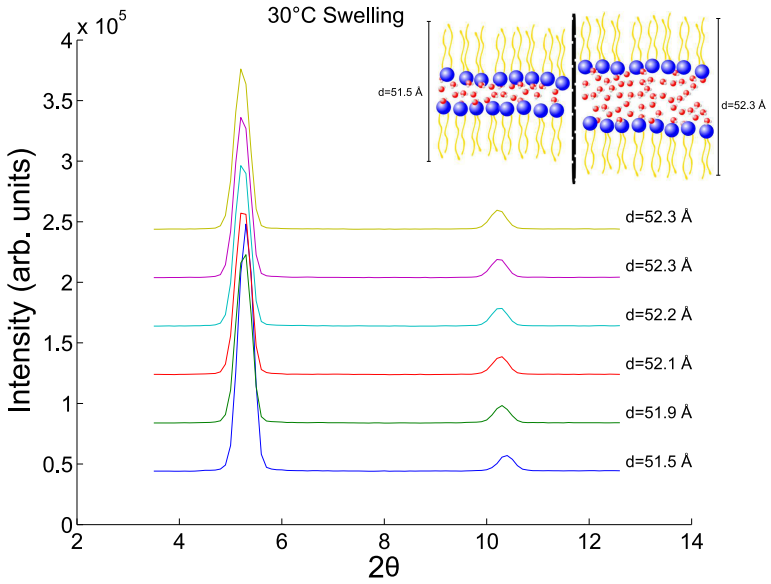

Figure 5.20: Hydration run on V1 diffractometer, HZB. DMPC sample at 30°C. The *d*-spacing of the sample is calculated through the Bragg equation (Equation 2.3), and relates to a humidity range of ∼97% to ∼99% relative humidity (see 5.2). The inset shows the swelling of the bilayer pictorially, the water layer is exaggerated for clarity.

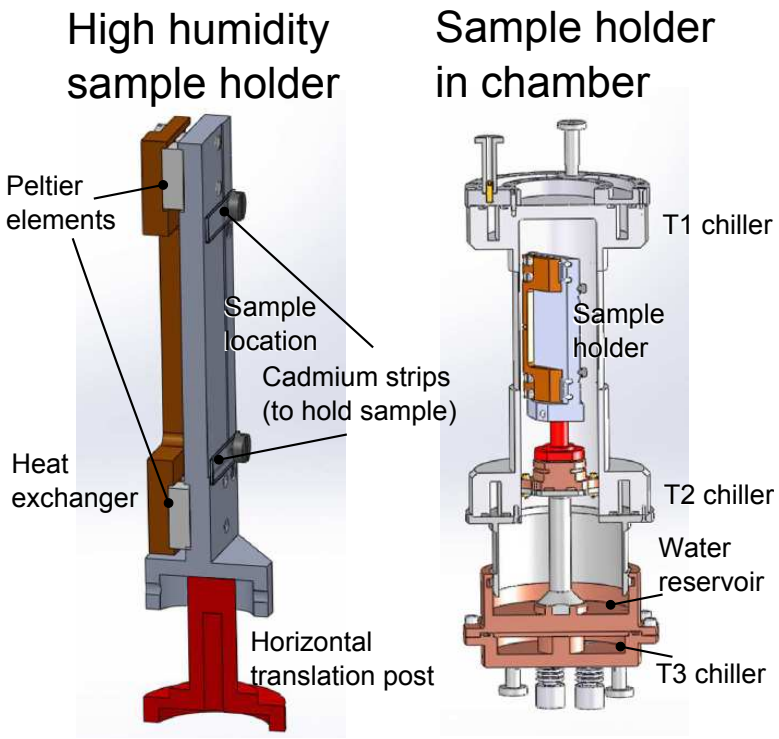

Figure 5.21: CAD of the high humidity sample holder (left) and the holder mounted inside the BerILL 2.0 chamber (right). Although it is compatible with both the HZB BerILL 1.0 and the ILL Berill 2.0 humidity chambers.

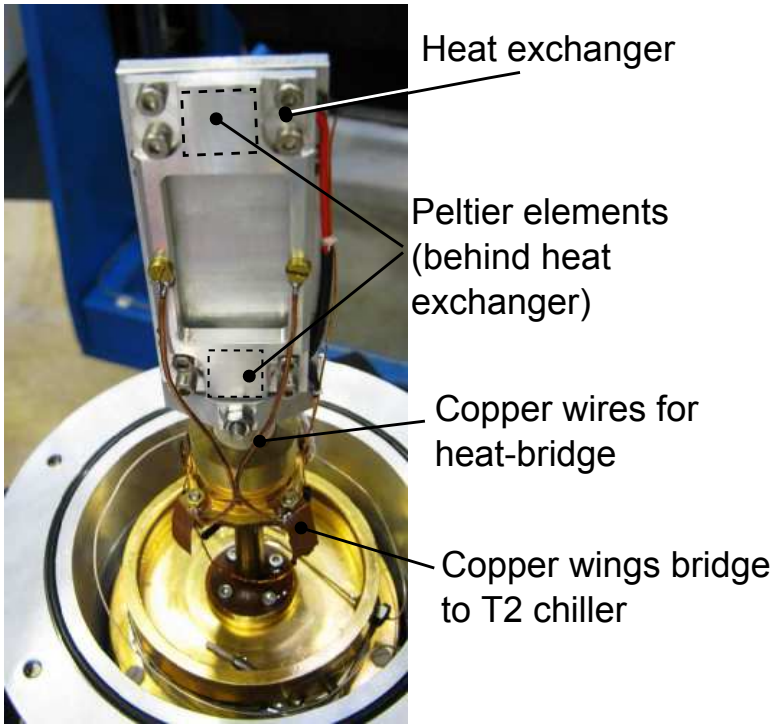

Figure 5.22: High humidity sample holder mounted onto chamber base. Peltier elements are clamped between the sample mount and heat-exchanger. Heat exchanger forms a thermal bridge to the T2 chiller through two thick copper wires and four copper wings, removing heat from the warm side of the Peltier elements.

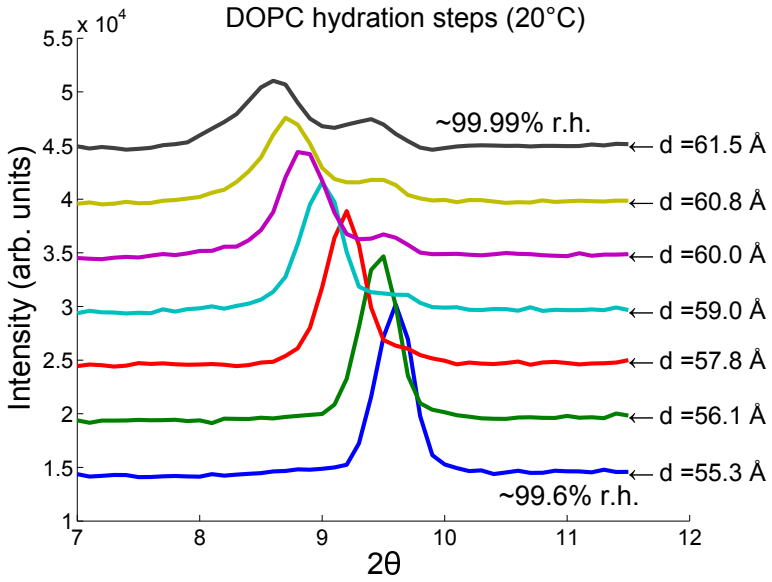

Figure 5.23: Bragg reflections from a DOPC lipid bilayer at 20°C. Calculated d-spacings of each measurement are shown, relating to 99.6% to 99.99% relative humidity. Above a d-spacing of 59 Å splitting occurs, which may indicate two domains in the sample.

6 Summary and Outlook

6.1 Summary

The experimental work described in this thesis involved both structural and dynamical measurements of model lipid membranes and the changes induced by a selection of amyloid-β peptides.

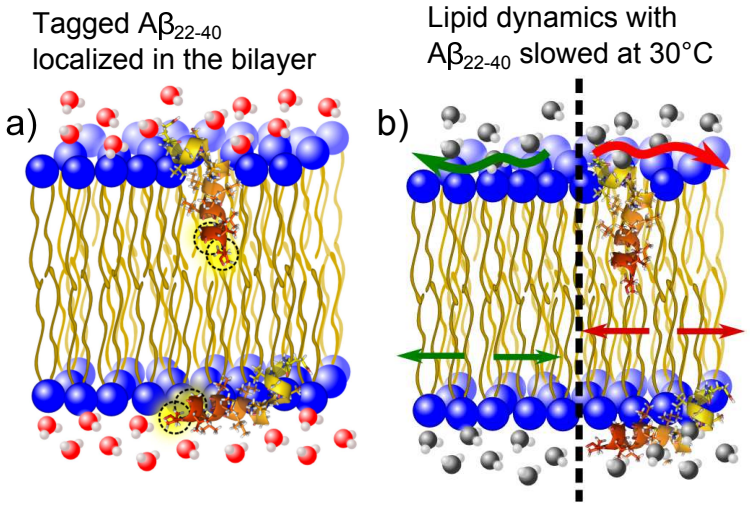

Figure 6.1: a) The position of amyloid-β_{22-40} peptide in the lipid bilayer was determined through neutron diffraction experiments with lipid bilayers containing deuterium tagged peptides. b) The dynamics of lipids over a picosecond to nanosecond time-scale and the dynamic perturbations induced by a peptide have been characterized. At 30°C, the presence of the peptide causes slowing of lipid dynamics which have assigned to the lipid centre of mass diffusion and lipid tails.

In Chapter 3, experiments were performed on anionic lipid bilayers consisting of DMPC and DMPS lipid model membranes to localize a small molar amount (1.5 mol%) of the peptide amyloid-β_{22-40}, determine what structural changes this peptide induces in the membrane and finally determine how the presence of this peptide perturbs lipid dynamics spanning time-scales from picoseconds to nanoseconds. Figure 6.1 presents graphically both of these results.

For the first time, evidence was presented which indicates the amyloid-β_{22-40}

peptide intercalates into the lipid membrane and in doing so increases the lipid bilayer *d*-spacing. With the knowledge of the peptide location in the lipid bilayer, quasi-elastic neutron scattering experiments with this particular peptide fragment using a range of instrumental resolutions (and thus a broad time-range) were performed. This was the first experimental evidence published revealing the dynamics of lipid bilayers affected by peptides over such a broad time-scale, relating to lipid dynamical processes including whole molecule diffusion, lipid chain dynamics, and localized vibrational motions. These measurements reveal that 1.5 mol% of the peptide can induce changes in the lipid dynamics over multiple time-scales, with increased diffusion coefficients in the gel-phase, and decreased diffusion coefficients reported near the phase transition. This type of perturbation of lipid bilayer dynamics has been seen in lipid bilayers containing low concentrations (∼5 mol%) of molecules including cholesterol and sodium glycocholate (a surfactant used to emulsify fats and enable absorption in the digestive system) [81]. More recently a publication from Sharma *et al.* (July 2015 [33]), in which a very low concentration (0.2 mol%) of melittin peptide was added to DMPC vesicles, presents results on lipid dynamics in the nanosecond regime which reflect very closely the findings presented in this thesis.

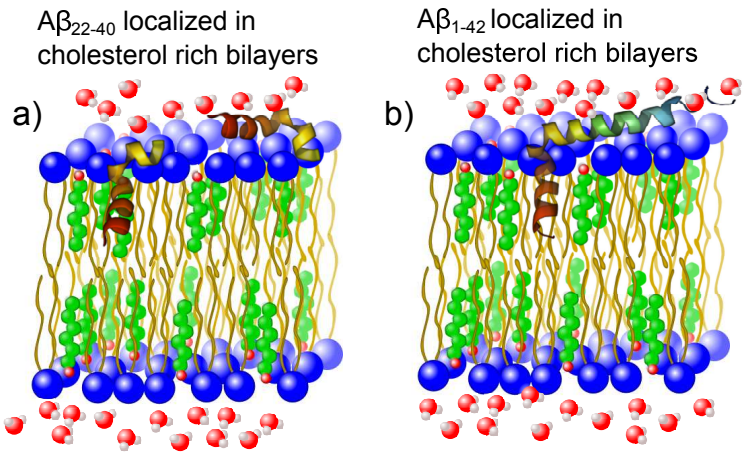

Figure 6.2: a) The locations and orientations of an amyloid-β_{22-40} peptide fragment in cholesterol rich (≥30 mol% cholesterol) bilayers were determined using X-ray diffraction experiments. A two population model, with a surface and embedded peptide best fit the experimental results. b) The locations and orientations of an amyloid-β_{1-42} peptide in cholesterol rich (≥30 mol% cholesterol) bilayers were also determined. A single peptide model was sufficient to describe the electron density differences at 40 mol% cholesterol.

In Chapter 4 an anionic membrane containing cholesterol has been measured with both the amyloid-β_{22-40} fragment (as was used in Chapter 3) and the full-length amyloid-β_{1-42}. The effect of the cholesterol on the bilayer structure with and without the peptide was tested, and the location of the peptide was modelled in membranes below and above the cholesterol saturation limit in the bilayer. Evidence was presented

which shows that both of the peptides intercalate into the bilayer, and have a substantial effect on the membrane structural parameters. This is the first systematic study of the influence of cholesterol and these amyloid-β peptides on the membrane structure.

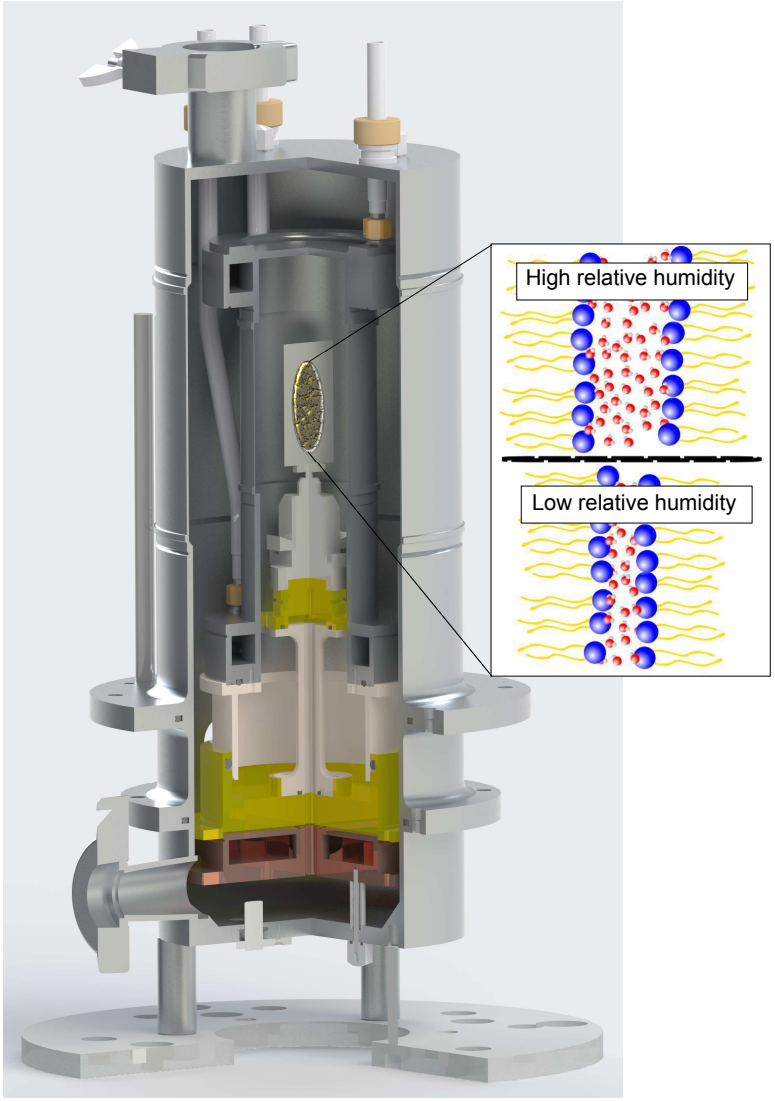

Figure 6.3: BerILL humidity chamber with supported lipid multilayer sample. The chamber allows for the humidity to be regulated to high accuracy and with fast equilibration times. In the case of a lipid membrane multilayer sample (represented by a single layer in the box), the repeat distance between low (≤90%r.H.) humidity and high (≥98%) humidity swells a dramatic 10 with water recruited to the region between lipid head-groups.

Finally, in Chapter 5, the development and commissioning of a new humidity and temperature sample environment for neutron experiments is presented. The BerILL

humidity chamber (Figure 6.3) now exists in two working prototypes located at the Helmholtz-Zentrum Berlin and the Institut Laue-Langevin, and has seen the first user service in September 2015. This chamber allows for more efficient experiments on biological samples (like the model membranes presented in this thesis) as well as other humidity/hydration sensitive materials.

6.2 Outlook

The structural measurements of peptides in cholesterol-rich model membranes presented in Chapter 4 set the stage for lipid dynamic studies of the same system. These structural results indicate that both the fragment amyloid-β_{22-40} and the full-length amyloid-β_{1-42} intercalate into the cholesterol rich membrane, and cause substantial structural changes. Dynamical studies of this system would lead to a better understanding of the relationship between the structural changes induced by the peptide and the dynamical processes which the lipids in the bilayer undergo. In the melittin-membrane system discussed previously (by Sharma *et al.* [33]) the centre-of-mass lipid diffusion was studied in a lipid bilayer, with results reflecting the amyloid-β_{22-40} results presented in this thesis, but also with cholesterol-rich bilayers (20 mol% cholesterol). In the cholesterol-rich samples, no detectable change was observed in membranes with and without the melittin peptide. It is thus an exciting and logical next step to perform quasi-elastic neutron scattering on samples containing peptides which interact with cholesterol-rich bilayers.

A step further towards physiological relevance especially with respect to Alzheimer's disease would involve determining the effect of amyloid-β peptides on natural membranes. Experiments on model membranes provide valuable first steps, and an understanding of important physical processes, but lack many of the important complexities which natural membranes contain. An ideal candidate in these experiments would be using membranes of mitochondria. The mitochondria organelle is responsible for production of adenosine triphosphate (ATP), which is required to carry out synaptic processes and to produce neurotransmitters. Mitochondria are found in high concentration near the synapses of neuronal cells, where this ATP is used in large quantities. Experiments on mitochondrial membranes would allow one to test if the effects observed in model membranes can be translated to natural systems.

Experiments on model lipid membranes in very high humidity ranges are also now possible with the use of the BerILL humidity chamber. Experimental conditions which were unstable or inaccessible previously are now within the range of experimental feasibility. As well as extreme humidity conditions, diffraction experiments with moderate humidity ranges will be more efficient, determination of phase coefficients can be performed through swelling of the bilayer, rather than opening the chamber to replace the D_2O:H_2O ratio of the water reservoir.

Bibliography

[1] S. Singer and G. Nicolson, "The fluid mosaic model of the structure of cell membranes," *Science*, vol. 175, pp. 720–731, 1972.

[2] O. Mouritsen, *Life as a matter of fat.* Springer, 2006.

[3] D. R. Silvius, *Thermotropic Phase Transitions of Pure Lipids in Model Membranes and Their Modifications by Membrane Proteins.* New York: John Wiley & Sons, Inc, 1982.

[4] B. Alberts, A. Johnson, J. Lewis, M. Raff, K. Roberst, and P. Walter, *Molecular Biology of the Cell.* New York: Garland Science, 4 ed., 2002.

[5] R. Phillips, J. Kondev, J. Theriot, and G. Hernan, *Physical Biology of the Cell.* Garland Science, 2 ed., 2009.

[6] F. R. Maxfield and I. Tabas, "Role of cholesterol and lipid organization in disease.," *Nature*, vol. 438, pp. 612–621, Dec. 2005.

[7] A. Soldano and B. A. Hassan, "Beyond pathology: APP, brain development and Alzheimer's disease.," *Curr. Opin. Neurobiol.*, vol. 27, pp. 61–67, Mar. 2014.

[8] I. Peters, U. Igbavboa, T. Schütt, S. Haidari, U. Hartig, X. Rosello, S. Böttner, E. Copanaki, T. Deller, D. Kögel, W. G. Wood, W. E. Müller, and G. P. Eckert, "The interaction of beta-amyloid protein with cellular membranes stimulates its own production.," *Biochim. Biophys. Acta*, vol. 1788, pp. 964–972, May 2009.

[9] L. Pagani and A. Eckert, "Amyloid-Beta interaction with mitochondria.," *Int. J. Alzheimers. Dis.*, vol. 2011, p. 925050, Jan. 2011.

[10] R. Swerdlow, J. Burns, and S. Khan, "The Alzheimer's disease mitochondrial cascade hypothesis," *J. Alzheimer's Dis.*, vol. 20, no. Suppl 2, pp. 265–279, 2010.

[11] D. J. Selkoe, "Soluble oligomers of the amyloid beta-protein impair synaptic plasticity and behavior.," *Behav. Brain Res.*, vol. 192, pp. 106–113, Sept. 2008.

[12] C. Haass and D. J. Selkoe, "Soluble protein oligomers in neurodegeneration: lessons from the Alzheimer's amyloid beta-peptide.," *Nat. Rev. Mol. Cell Biol.*, vol. 8, pp. 101–112, Feb. 2007.

[13] K. Simons and D. Toomre, "Lipid rafts and signal transduction.," *Nat. Rev. Mol. Cell Biol.*, vol. 1, pp. 31–39, Oct. 2000.

[14] A. Alzheimer, "Über eine eigenartige Erkangung der Hirnrinde," *Allegemeine Zeitscher Psychiatr Psych. Medizin*, vol. 64, no. 46, 1907.

[15] A. Lorenzo and B. Yankner, "Amyloid Fibril Toxicity in Alzheimer's Disease and Diabetes," *Ann. N. Y. Acad. Sci.*, vol. 617, pp. 89–95, 1996.

[16] C. McLean and R. Cherny, "Soluble pool of Aβ amyloid as a determinant of severity of neurodegeneration in Alzheimer's disease," *Ann. Neurol.*, vol. 46, no. 6, pp. 860–866, 1999.

[17] D. Selkoe, "Alzheimer's disease: genes, proteins, and therapy," *Physiol. Rev.*, vol. 81, no. 2, pp. 741–766, 2001.

[18] X. Yang, G. Y. Sun, G. P. Eckert, and J. C.-M. Lee, "Cellular Membrane Fluidity in Amyloid Precursor Protein Processing.," *Mol. Neurobiol.*, vol. 50, pp. 119–129, Feb. 2014.

[19] K. Ono, M. M. Condron, and D. B. Teplow, "Structure-neurotoxicity relationships of amyloid beta-protein oligomers.," *Proc. Natl. Acad. Sci. U. S. A.*, vol. 106, pp. 14745–14750, Sept. 2009.

[20] E. Drolle, F. Hane, B. Lee, and Z. Leonenko, "Atomic force microscopy to study molecular mechanisms of amyloid fibril formation and toxicity in Alzheimer's disease.," *Drug Metab. Rev.*, vol. 46, pp. 207–223, May 2014.

[21] K. Berthelot, C. Cullin, and S. Lecomte, "What does make an amyloid toxic: morphology, structure or interaction with membrane?," *Biochimie*, vol. 95, pp. 12–19, Jan. 2013.

[22] S. Dante, T. Hauss, and N. A. Dencher, "Beta-amyloid 25 to 35 is intercalated in anionic and zwitterionic lipid membranes to different extents.," *Biophys. J.*, vol. 83, pp. 2610–2616, Nov. 2002.

[23] S. Dante, T. Hauss, A. Brandt, and N. A. Dencher, "Membrane fusogenic activity of the Alzheimer's peptide A beta(1-42) demonstrated by small-angle neutron scattering.," *J. Mol. Biol.*, vol. 376, pp. 393–404, Feb. 2008.

[24] A. Y. Abramov, M. Ionov, E. Pavlov, and M. R. Duchen, "Membrane cholesterol content plays a key role in the neurotoxicity of β-amyloid: implications for Alzheimer's disease.," *Aging Cell*, vol. 10, pp. 595–603, Aug. 2011.

[25] H. A. Lashuel, D. Hartley, B. M. Petre, T. Walz, and P. T. J. Lansbury, "Amyloid pores from pathogenic mutations," *Nature*, vol. 418, no. July, pp. 4–5, 2002.

[26] P. Sorrentino, A. Iuliano, A. Polverino, F. Jacini, and G. Sorrentino, "The dark sides of amyloid in Alzheimer's disease pathogenesis.," *FEBS Lett.*, vol. 588, pp. 641–652, Mar. 2014.

[27] E. Flenner, J. Das, M. Rheinstädter, and I. Kosztin, "Subdiffusion and lateral diffusion coefficient of lipid atoms and molecules in phospholipid bilayers," *Phys. Rev. E*, vol. 79, p. 011907, Jan. 2009.

[28] J. Yang, C. Calero, and J. Martí, "Diffusion and spectroscopy of water and lipids in fully hydrated dimyristoylphosphatidylcholine bilayer membranes," *J. Chem. Phys*, vol. 140, p. 104901, 2014.

[29] R. Lechner, "Observation-time dependent structural information from quasielastic neutron scattering," *Phys. B Condens. Matter*, vol. 301, pp. 83–93, July 2001.

[30] S. Busch, L. C. Pardo, C. Smuda, and T. Unruh, "The picosecond dynamics of the phospholipid dimyristoylphosphatidylcholine in mono- and bilayers," *Soft Matter*, vol. 8, no. 13, p. 3576, 2012.

[31] U. Wanderlingh and G. D'Angelo, "Multi-component modeling of quasielastic neutron scattering from phospholipid membranes," *J. Chem. Phys*, vol. 140, p. 174901, 2014.

[32] V. K. Sharma, E. Mamontov, D. Anunciado, H. M. O. Neill, and V. S. Urban, "Nanoscopic Dynamics of Phospholipid in Unilamellar Vesicles : Effect of Gel to Fluid Phase Transition," *J. Phys. Chem. B.*, vol. 119, no. 12, pp. 4460–4470, 2015.

[33] V. K. Sharma, E. Mamontov, D. B. Anunciado, H. O'Neill, and V. S. Urban, "Effect of antimicrobial peptide on the dynamics of phosphocholine membrane: role of cholesterol and physical state of bilayer," *Soft Matter*, vol. 11, no. 34, pp. 6755–6767, 2015.

[34] S. Koenig, W. Pfeiffer, T. Bayerl, D. Richter, and E. Sackmann, "Molecular dynamics of lipid bilayers studied by incoherent quasi-elastic neutron scattering," *J. Phys. II*, vol. 2, pp. 1589–1615, 1992.

[35] W. Pfeiffer and T. Henkel, "Local dynamics of lipid bilayers studied by incoherent quasi-elastic neutron scattering," *Europhys. Lett.*, vol. 8, pp. 201–206, 1989.

[36] C. L. Armstrong, M. Trapp, J. Peters, T. Seydel, and M. C. Rheinstädter, "Short range ballistic motion in fluid lipid bilayers studied by quasi-elastic neutron scattering," *Soft Matter*, vol. 7, no. 18, p. 8358, 2011.

[37] C. L. Armstrong, M. D. Kaye, M. Zamponi, E. Mamontov, M. Tyagi, T. Jenkins, and M. C. Rheinstädter, "Diffusion in single supported lipid bilayers studied by quasi-elastic neutron scattering," *Soft Matter*, vol. 6, no. 23, p. 5864, 2010.

[38] R. Machán and M. Hof, "Lipid diffusion in planar membranes investigated by fluorescence correlation spectroscopy.," *Biochim. Biophys. Acta*, vol. 1798, pp. 1377–1391, July 2010.

[39] K. Weiss, A. Neef, Q. Van, and S. Kramer, "Quantifying the Diffusion of Membrane Proteins and Peptides in Black Lipid Membranes with 2-Focus Fluorescence Correlation Spectroscopy," *Biophys. J.*, vol. 105, pp. 455–462, 2013.

[40] M. Ameloot and M. Vandeven, "Fluorescence anisotropy measurements in solution: Methods and reference materials (IUPAC Technical Report)," *Pure Appl. Chem.*, vol. 85, no. 3, pp. 589–608, 2013.

[41] F. Picard, M. J. Paquet, E. J. Dufourc, and M. Auger, "Measurement of the lateral diffusion of dipalmitoylphosphatidylcholine adsorbed on silica beads in the absence and presence of melittin: a 31P two-dimensional exchange solid-state NMR study.," *Biophys. J.*, vol. 74, pp. 857–868, Feb. 1998.

[42] G. Orädd and G. Lindblom, "NMR Studies of lipid lateral diffusion in the DMPC/gramicidin D/water system: peptide aggregation and obstruction effects.," *Biophys. J.*, vol. 87, pp. 980–987, Aug. 2004.

[43] S. Busch and T. Unruh, "The slow short-time motions of phospholipid molecules with a focus on the influence of multiple scattering and fitting artefacts," *J. Phys. Condens. Matter*, vol. 23, p. 254205, June 2011.

[44] A. Buchsteiner, T. Hauss, S. Dante, and N. Dencher, "Alzheimer's disease amyloid- β peptide analogue alters the ps-dynamics of phospholipid membranes," *Biochim. Biophys. Acta*, vol. 1798, pp. 1969–1976, 2010.

[45] A. Buchsteiner, T. Hauß, and N. A. Dencher, "Influence of amyloid-β peptides with different lengths and amino acid sequences on the lateral diffusion of lipids in model membranes," *Soft Matter*, vol. 8, no. 2, p. 424, 2012.

[46] G. van Meer, D. R. Voelker, and G. W. Feigenson, "Membrane lipids: where they are and how they behave.," *Nat. Rev. Mol. Cell Biol.*, vol. 9, pp. 112–24, Feb. 2008.

[47] E. Bianconi, A. Piovesan, F. Facchin, A. Beraudi, R. Casadei, F. Frabetti, L. Vitale, M. C. Pelleri, S. Tassani, F. Piva, S. Perez-Amodio, P. Strippoli, and S. Canaider, "An estimation of the number of cells in the human body," *Ann Hum. Bio.*, vol. 40, no. 6, p. 471, 2013.

[48] Avanti, "Avanti Polar Lipids," 2015.

[49] W. Dowhan and M. Bogdanov, "Functional roles of lipids in membranes," in *Biochem. Lipids, Lipoproteins Membr.* (D. Vance and J. E. Vance, eds.), ch. 1, Elsevier Science, 4 ed., 2002.

[50] E. Fahy, S. Subramaniam, R. C. Murphy, M. Nishijima, C. R. H. Raetz, T. Shimizu, F. Spener, G. van Meer, M. J. O. Wakelam, and E. A. Dennis, "Update of the LIPID MAPS comprehensive classification system for lipids.," *J. Lipid Res.*, vol. 50, pp. S9–14, Apr. 2009.

[51] E. Fahy, S. Subramaniam, H. A. Brown, C. K. Glass, A. H. Merrill, R. C. Murphy, C. R. H. Raetz, D. W. Russell, Y. Seyama, W. Shaw, T. Shimizu, F. Spener, G. van Meer, M. S. VanNieuwenhze, S. H. White, J. L. Witztum, and E. a. Dennis, "A comprehensive classification system for lipids.," *J. Lipid Res.*, vol. 46, pp. 839–61, May 2005.

[52] R. Coleman, "Enzymes of triacylglycerol synthesis and their regulation," *Prog. Lipid Res.*, vol. 43, pp. 134–176, Mar. 2004.

[53] B. Ramstedt and J. S. Peter, "Membrane properties of sphingomyelins," *FEBS Lett.*, vol. 531, pp. 33–37, 2002.

[54] R. Lipowsky and E. Sackmann, "Structure and dynamics of membranes: I. from cells to vesicles/II. generic and specific interactions.," in *Handb. Biol. Phys.*, Elsevier, 1995.

[55] D. Vance and J. Vance, *Biochemistry of Lipids, Lipoproteins and Membranes*. Amsterdam: Elsevier B.V., 1 ed., 2008.

[56] D. Bach and E. Wachtel, "Phospholipid/cholesterol model membranes: Formation of cholesterol crystallites," *Biochim. Biophys. Acta - Biomembr.*, vol. 1610, no. 2, pp. 187–197, 2003.

[57] D. Marsh, *CRC Handbook of Lipid Bilayers*. CRC Press, 1990.

[58] G. Smith, E. Sirota, C. Safinya, and N. Clark, "Structure of the Lβ phases in a hydrated phosphatidylcholine multimembrane," *Phys. Rev. Lett.*, vol. 60, no. 9, pp. 813–816, 1988.

[59] J. Tocanne, L. Dupou-Cézanne, and A. Lopez, "Lateral diffusion of lipids in model and natural membranes," *Prog. Lipid Res.*, vol. 33, no. 3, pp. 203–237, 1994.

[60] P. Sane, E. Salonen, E. Falck, J. Repakova, F. Tuomisto, J. M. Holopainen, and I. Vattulainen, "Probing biomembranes with positrons," *J. Phys. Chem. B*, vol. 113, no. 7, pp. 1810–1812, 2009.

[61] J. F. Nagle, "Theory of lipid monolayer and bilayer phase transitions: effect of headgroup interactions.," *J. Membr. Biol.*, vol. 27, no. 3, pp. 233–250, 1976.

[62] J. S. Hub, T. Salditt, M. C. Rheinstädter, and B. L. de Groot, "Short-range order and collective dynamics of DMPC bilayers: a comparison between molecular dynamics simulations, X-ray, and neutron scattering experiments.," *Biophys. J.*, vol. 93, pp. 3156–68, Nov. 2007.

[63] N. Kucerka, Y. Liu, N. Chu, H. I. Petrache, S. Tristram-Nagle, and J. F. Nagle, "Structure of fully hydrated fluid phase DMPC and DLPC lipid bilayers using X-ray scattering from oriented multilamellar arrays and from unilamellar vesicles.," *Biophys. J.*, vol. 88, pp. 2626–37, Apr. 2005.

[64] H. Petrache, S. Tristram-Nagle, and J. Nagle, "Fluid phase structure of EPC and DMPC bilayers," *Chem. Phys. Lipids*, vol. 95, no. 1, pp. 83–94, 1998.

[65] S. Tristram-Nagle, Y. Liu, J. Legleiter, and J. F. Nagle, "Structure of gel phase DMPC determined by X-ray diffraction.," *Biophys. J.*, vol. 83, pp. 3324–3335, Dec. 2002.

[66] M. Trapp, T. Gutberlet, F. Juranyi, T. Unruh, B. Demé, M. Tehei, and J. Peters, "Hydration dependent studies of highly aligned multilayer lipid membranes by neutron scattering.," *J. Chem. Phys.*, vol. 133, p. 164505, Oct. 2010.

[67] P. F. F. Almeida, W. L. C. Vaz, and T. E. Thompson, "Lipid diffusion, free area, and molecular dynamics simulations.," *Biophys. J.*, vol. 88, pp. 4434–8, June 2005.

[68] M. Rheinstädter, J. Das, E. Flenner, B. Brüning, T. Seydel, and I. Kosztin, "Motional Coherence in Fluid Phospholipid Membranes," *Phys. Rev. Lett.*, vol. 101, p. 248106, Dec. 2008.

[69] J. Katsaras, "Adsorbed to a rigid substrate, dimyristoylphosphatidylcholine multibilayers attain full hydration in all mesophases.," *Biophys. J.*, vol. 75, pp. 2157–62, Nov. 1998.

[70] S. Dante, T. Hauss, and N. A. Dencher, "Insertion of externally administered amyloid beta peptide 25-35 and perturbation of lipid bilayers.," *Biochemistry*, vol. 42, pp. 13667–13672, Dec. 2003.

[71] G. Szabo, "Dual mechanism for the action of cholesterol on membrane permeability," *Nature*, vol. 252, pp. 47–49, 1974.

[72] S. Munro, "Lipid Rafts : Elusive or Illusive," *Cell*, vol. 115, pp. 377–388, 2003.

[73] H. Lodish, A. Berk, and S. Zipursky, *Molecular Cell Biology.* New York: W. H. Freeman, 4 ed., 2000.

[74] E. P. Carpenter, K. Beis, A. D. Cameron, and S. Iwata, "Overcoming the challenges of membrane protein crystallography.," *Curr. Opin. Struct. Biol.*, vol. 18, pp. 581–6, Oct. 2008.

[75] M. Goedert and M. G. Spillantini, "A Century of Alzheimer's Disease," *Science*, vol. 314, no. 5800, pp. 777–781, 2006.

[76] C. Holmes, D. Boche, D. Wilkinson, G. Yadegarfar, V. Hopkins, A. Bayer, R. W. Jones, R. Bullock, S. Love, J. W. Neal, E. Zotova, and J. A. R. Nicoll, "Long-term effects of Aβ 42 immunisation in Alzheimer's disease: follow-up of a randomised, placebo-controlled phase I trial," *Lancet*, vol. 372, pp. 11–14, 2008.

[77] S. Dante, T. Hauss, and N. A. Dencher, "Cholesterol inhibits the insertion of the Alzheimer's peptide Abeta(25-35) in lipid bilayers.," *Eur. Biophys. J.*, vol. 35, pp. 523–531, Aug. 2006.

[78] S. Tristram-Nagle, D. J. Kim, N. Akhunzada, N. Kučerka, C. Mathai, J. Katsaras, M. Zeidel, and J. F. Nagle, "Structure and Water permeability of Fully Hydrated DiphytanoylPC," *Chem Phys. Lipids*, vol. 163, no. 6, pp. 630–637, 2010.

[79] D. R. Silvius, *Thermotropic Phase Transitions of Pure Lipids in Model Membranes and Their Modifications by Membrane Proteins.* New York: John Wiley & Sons, Inc., 1982.

[80] S. Karmakar, V. A. Raghunathan, and S. Mayor, "Phase behaviour of dipalmitoyl phosphatidylcholine (DPPC)-cholesterol membranes," *J. Phys. Condens. Matter*, vol. 17, pp. S1177–S1182, Apr. 2005.

[81] S. Busch and T. Unruh, "The influence of additives on the nanoscopic dynamics of the phospholipid dimyristoylphosphatidylcholine.," *Biochim. Biophys. Acta*, vol. 1808, pp. 199–208, Jan. 2011.

[82] M. C. Rheinstädter, "Lipid Membrane Dynamics," in *Dyn. Soft Matter Neutron Appl.* (V. García Sakai, C. Alba-Simionesco, and S.-H. Chen, eds.), Neutron Scattering Applications and Techniques, Boston, MA: Springer US, 2012.

[83] N. Kucerka, S. Tristram-Nagle, and J. F. Nagle, "Structure of fully hydrated fluid phase lipid bilayers with monounsaturated chains.," *J. Membr. Biol.*, vol. 208, pp. 193–202, Dec. 2005.

[84] R. P. Mason, J. D. Estermyer, J. F. Kelly, and P. E. Mason, "Alzheimer's disease amyloid beta peptide 25-35 is localized in the membrane hydrocarbon core: x-ray diffraction analysis.," *Biochem. Biophys. Res. Commun.*, vol. 222, no. 1, pp. 78–82, 1996.

[85] S. Dante, T. Hauß, R. Steitz, C. Canale, and N. A. Dencher, "Nanoscale structural and mechanical effects of beta-amyloid," *BBA - Biomembr.*, vol. 1808, no. 11, pp. 2646–2655, 2011.

[86] H. Dies, L. Toppozini, and M. C. Rheinstädter, "The Interaction between Amyloid-β Peptides and Anionic Lipid Membranes Containing Cholesterol and Melatonin.," *PLoS One*, vol. 9, p. e99124, Jan. 2014.

[87] A. Koudinov and N. V. Koudinova, "Proteolysis-inducing factor regulates hepatic gene expression via the transcription factors NF-(kappa)B and STAT3.," *FASEB J.*, vol. 15, no. 3, pp. 562–564, 2001.

[88] J. Sankaran, M. Manna, L. Guo, R. Kraut, and T. Wohland, "Diffusion, transport, and cell membrane organization investigated by imaging fluorescence cross-correlation spectroscopy.," *Biophys. J.*, vol. 97, pp. 2630–2639, Nov. 2009.

[89] F. Heinemann, V. Betaneli, F. a. Thomas, and P. Schwille, "Quantifying lipid diffusion by fluorescence correlation spectroscopy: a critical treatise.," *Langmuir*, vol. 28, pp. 13395–404, Sept. 2012.

[90] R. M. Walko and E. A. Nothnagel, "Lateral diffusion of proteins and lipids in the plasma membrane of rose protoplast," *Protoplamsa*, vol. 152, pp. 46–56, 1989.

[91] G. R. Kneller, K. Baczynski, and M. Pasenkiewicz-Gierula, "Communication: consistent picture of lateral subdiffusion in lipid bilayers: molecular dynamics simulation and exact results.," *J. Chem. Phys.*, vol. 135, p. 141105, Oct. 2011.

[92] R. W. Pastor, R. M. Venable, and S. E. Feller, "Lipid Bilayers, NMR Relaxation, and Computer Simulations," *Acc. Chem. Res*, vol. 35, no. 6, pp. 438–446, 2002.

[93] M. F. Roberts, A. G. Redfield, and U. Mohanty, "Phospholipid reorientation at the lipid/water interface measured by high resolution 31P field cycling NMR spectroscopy.," *Biophys. J.*, vol. 97, pp. 132–41, July 2009.

[94] J. Perlo, C. J. Meledandri, E. Anoardo, and D. F. Brougham, "Temperature and Size-Dependence of Membrane Molecular Dynamics in Unilamellar Vesicles by Fast Field-Cycling NMR Relaxometry," *J. Phys. Chem. B*, vol. 115, pp. 3444–3451, 2011.

[95] W. Vaz, R. Clegg, and D. Hallmann, "Translational diffusion of lipids in liquid crystalline phase phosphatidylcholine multibilayers. A comparison of experiment with theory," *Biochemistry*, vol. 85, 1985.

[96] J. H. Davis, "The influence of membrane protiens on lipid dynamics," *Chem. Phys. Lipids*, vol. 40, pp. 223–258, 1986.

[97] G. Lindblom and G. Orädd, "Lipid lateral diffusion and membrane heterogeneity.," *Biochim. Biophys. Acta*, vol. 1788, pp. 234–44, Jan. 2009.

[98] J. Tabony and B. Perly, "Quasielastic neutron scattering measurements of fast local translational diffusion of lipid molecules in phospholipid bilayers.," *Biochim. Biophys. Acta*, vol. 1063, pp. 67–72, Mar. 1991.

[99] S. Koenig, E. Sackmann, D. Richter, R. Zorn, C. Carlile, and T. M. Bayerl, "Molecular dynamics of water in oriented DPPC multilayers studied by quasielastic neutron scattering and deuterium-nuclear magnetic resonance relaxation," *J. Chem. Phys.*, vol. 100, no. 4, p. 3307, 1994.

[100] E. Falck, M. Patra, M. Karttunen, M. T. Hyvönen, and I. Vattulainen, "Lessons of slicing membranes: interplay of packing, free area, and lateral diffusion in phospholipid/cholesterol bilayers.," *Biophys. J.*, vol. 87, pp. 1076–91, Aug. 2004.

[101] E. Falck, M. Patra, M. Karttunen, M. T. Hyvönen, and I. Vattulainen, "Response to comment by Almeida et al.: free area theories for lipid bilayers–predictive or not?," *Biophys. J.*, vol. 89, pp. 745–52, July 2005.

[102] N. Media, "The Nobel Prize in Physics 1901," 2014.

[103] N. Media, "The Nobel Prize in Physics 1914," 2014.

[104] N. Media, "The Nobel Prize in Physics 1915," 2014.

[105] J. Chadwick, "The Existence of a Neutron," *Proc. R. Soc. A Math. Phys. Eng. Sci.*, vol. 136, no. 830, pp. 692–708, 1932.

[106] N. Media, "The Nobel Prize in Physics 1935," 2014.

[107] N. Media, "The Nobel Prize in Physics 1994," 2014.

[108] B. Warren, *X-ray Diffraction*. Reading, Mass.: Addison-Wesley, 1 ed., 1969.

[109] G. Squires, *An Introduction to Thermal Neutron Scattering*. Cambridge: Cambridge University Press, 1978.

[110] E. P. Bertin, "Properties of X-rays," in *Princ. Pract. X-Ray Spectrom. Anal.*, ch. 2, pp. 51–85, Springer US, 2 ed., 1975.

[111] R. Pynn, *Neutron Scattering: A primer*. Los Alamos: Los Alamos Science, 1990.

[112] V. Sears, "Neutron scattering lengths and cross sections," *Neutron news*, vol. 3, no. 3, pp. 26–37, 1992.

[113] Technische Universität München, "Neutron Source," 2015.

[114] T. Imae, T. Kanaya, M. Furusaka, and N. Torikai, eds., *Neutrons In Soft Matter*. New Jersey: John Wiley & Sons, Inc, 1 ed., 2011.

[115] M. A. Barrett, "Structure and Dynamics of Model Systems: From Ferrofluids to Brain Membranes," 2012.

[116] N. Franks and W. Lieb, "The structure of lipid bilayers and the effects of general anaesthetics," *J. Mol. Biol.*, vol. 133, no. 4, pp. 469–500, 1979.

[117] C. Suryanarayana and G. Norton, *X-Ray Diffraction: A Practical Approach*. New York: Springer, 1 ed., 1998.

[118] A. Wyner and S. Shamai, "Introduction To "Communication In The Presence Of Noise"," *Proc. IEEE*, vol. 86, no. 2, 1998.

[119] A. E. Blaurock, "Structure of the nerve myelin membrane: proof of the low-resolution profile.," *J. Mol. Biol.*, vol. 56, no. 1, pp. 35–52, 1971.

[120] L. van Hove, "Correlations in space and time and Born approximation scattering in systems of interacting particles," *Phys. Rev.*, vol. 95, no. 1, 1954.

[121] S. König, T. Bayerl, and G. Coddens, "Hydration dependence of chain dynamics and local diffusion in L-alpha-dipalmitoylphosphtidylcholine multilayers studied by incoherent quasi-elastic neutron," *Biophys. J.*, vol. 68, no. May, pp. 1871–1880, 1995.

[122] S. Jao, K. Ma, J. Talafous, R. Orlando, and M. Zagorski, "Trifluoroacetic acid pretreatment reproducibly disaggregates the amyloid β-peptide," *Amyloid Int. J. Exp Clin. Invest*, vol. 4, pp. 240–252, 1997.

[123] J. Katsaras, S. Tristram-Nagle, Y. Liu, R. Headrick, E. Fontes, P. Mason, and J. Nagle, "Clarification of the ripple phase of lecithin bilayers using fully hydrated, aligned samples," *Phys. Rev. E.*, vol. 61, no. 5, pp. 5668–5677, 2000.

[124] J. Bradshaw, M. Darkes, and T. Harroun, "Oblique membrane insertion of viral fusion peptide probed by neutron diffraction," *Biochemistry*, vol. 39, no. 22, pp. 0–4, 2000.

[125] T. N. Engelbrecht, A. Schroeter, T. Haußß, B. Demé, H. A. Scheidt, D. Huster, and R. H. H. Neubert, "The impact of ceramides NP and AP on the nanostructure of stratum corneum lipid bilayer. Part I: neutron diffraction and 2H NMR studies on multilamellar models based on ceramides with symmetric alkyl chain length distribution," *Soft Matter*, vol. 8, no. 24, p. 6599, 2012.

[126] L. Schrödinger, "The {PyMOL} Molecular Graphics System, Version˜1.3r1," 2010.

[127] J. Wuttke, "Improved sample holder for multidetector neutron spectrometers," *Phys. B Condens. Matter*, vol. 266, no. 1-2, pp. 112–114, 1999.

[128] R. Zorn, "On the evaluation of neutron scattering elastic scan data," *Nucl. Instruments Methods Phys. Res. Sect. A Accel. Spectrometers, Detect. Assoc. Equip.*, vol. 603, pp. 439–445, May 2009.

[129] D. Richard, M. Ferrand, and K. G.J., "LAMP," *J. Neutron Res. 4*, pp. 33–39, 1996.

[130] R. Azuah, L. Kneller, Y. Qiu, P. Tregenna-Piggott, C. Brown, J. Copley, and R. Dimeo, "DAVE: A comprehensive software suite for the reduction, visualization, and analysis of low energy neutron spectroscopic data," *Res. Natl. Inst. Stan. Technol.*, vol. 114, pp. 341–358, 2009.

[131] S. Busch, C. Smuda, L. C. Pardo, and T. Unruh, "Molecular mechanism of long-range diffusion in phospholipid membranes studied by quasielastic neutron scattering.," *J. Am. Chem. Soc.*, vol. 132, pp. 3232–3233, Mar. 2010.

[132] M. Doxastakis, V. G. Sakai, S. Ohtake, J. K. Maranas, and J. J. de Pablo, "A molecular view of melting in anhydrous phospholipidic membranes.," *Biophys. J.*, vol. 92, pp. 147–161, Jan. 2007.

[133] M. . Bee, *Quasielastic Neutron Scattering*. Bristol: Hilger, Adam, 1988.

[134] R. Bracewell, *The Fourier Transform and Its Applications*. New York: McGraw-Hill, 3 ed., 1999.

[135] B. Welch, "The Generalization of Student's Problem when Several Different Population Variances are Involved," *Biometrika*, vol. 34, no. 1, pp. 28–35, 1947.

[136] G. D. Ruxton, "The unequal variance t-test is an underused alternative to Student's t-test and the Mann-Whitney U test," *Behav. Ecol.*, vol. 17, no. 4, pp. 688–690, 2006.

[137] T. J. McIntosh, "The effect of cholesterol on the structure of phosphatidylcholine bilayers.," *Biochim. Biophys. Acta*, vol. 513, no. 1, pp. 43–58, 1978.

[138] J. Czub and M. Baginski, "Comparative Molecular Dynamics Study of Lipid Membranes Containing Cholesterol and Ergosterol," *Biophys. J.*, vol. 90, no. 7, pp. 2368–2382, 2006.

[139] J. Y. Lehtonen, J. M. Holopainen, and P. K. Kinnunen, "Evidence for the formation of microdomains in liquid crystalline large unilamellar vesicles caused by hydrophobic mismatch of the constituent phospholipids.," *Biophys. J.*, vol. 70, no. 4, pp. 1753–1760, 1996.

[140] P. F. F. Almeida, "Thermodynamics of lipid interactions in complex bilayers.," *Biochim. Biophys. Acta*, vol. 1788, pp. 72–85, Jan. 2009.

[141] M. Bokvist, F. Lindström, A. Watts, and G. Gröbner, "Two Types of Alzheimer's β-Amyloid (1-40) Peptide Membrane Interactions: Aggregation Preventing Transmembrane Anchoring Versus Accelerated Surface Fibril Formation," *J. Mol. Biol.*, vol. 335, pp. 1039–1049, Jan. 2004.

[142] S. M. Butterfield and H. A. Lashuel, "Amyloidogenic protein-membrane interactions: mechanistic insight from model systems.," *Angew. Chem. Int. Ed. Engl.*, vol. 49, pp. 5628–5654, Aug. 2010.

[143] D. L. Sparks, J. C. Hunsaker, S. Scheff, R. Kryscio, J. Henson, and W. Markesbery, "Cortical Senile Plaques in Coronary Artery Disease , Aging and Alzheimer ' s Disease," *Neurobiol. Aging*, vol. 11, pp. 601–607, 1990.

[144] W. G. Wood, F. Schroeder, U. Igbavboa, N. A. Avdulov, and S. V. Chochina, "Brain membrane cholesterol domains, aging and amyloid beta-peptides," *Neurobiol. Aging*, vol. 23, no. 5, pp. 685–694, 2002.

[145] T. Hartmann, "Cholesterol, Abeta and Alzheimer's disease," *TINS*, vol. 24, no. 11, pp. 45–48, 2001.

[146] A. Eckert, U. Keil, S. Kressmann, K. Schindowski, S. Leutner, S. Leutz, and W. E. Müller, "Effects of EGb 761 Ginkgo biloba extract on mitochondrial function and oxidative stress.," *Pharmacopsychiatry*, vol. 36 Suppl 1, pp. S15–S23, 2003.

[147] I. Casserly and E. Topol, "Convergence of atherosclerosis and Alzheimer's disease: Inflammation, cholesterol, and misfolded proteins," *Lancet*, vol. 363, no. 9415, pp. 1139–1146, 2004.

[148] L. A. Shobab, G. Y. R. Hsiung, and H. H. Feldman, "Cholesterol in Alzheimer's disease," *Lancet Neurol.*, vol. 4, no. 12, pp. 841–852, 2005.

[149] M. Simons, P. Keller, J. Dichgans, and J. B. Schultz, "Vitamin D and Alzheimer's Disease : Is There a Link ?," *Neurology*, vol. 57, pp. 1089–1093, 2010.

[150] L. Puglielli, R. E. Tanzi, and D. M. Kovacs, "Alzheimer's disease : the cholesterol connection," *Nat. Neurosci.*, vol. 6, no. 4, pp. 345–351, 2003.

[151] A. C. Fonseca, R. Resende, C. R. Oliveira, and C. M. F. Pereira, "Cholesterol and statins in Alzheimer's disease: Current controversies," *Exp. Neurol.*, vol. 223, no. 2, pp. 282–293, 2010.

[152] K. Fassbender, C. Masters, and K. Beyreuther, "Alzheimer's disease: Molecular concepts and therapeutic targets," *Naturwissenschaften*, vol. 88, no. 6, pp. 261–267, 2001.

[153] R. P. Mason, W. J. Shoemaker, L. Shajenko, T. E. Chambers, and L. G. Herbette, "Evidence for changes in the Alzheimer's disease brain cortical membrane structure mediated by cholesterol," *Neurobiol. Aging*, vol. 13, no. 3, pp. 413–419, 1992.

[154] T. T. Mills, G. E. S. Toombes, S. Tristram-Nagle, D.-M. Smilgies, G. W. Feigenson, and J. F. Nagle, "Order parameters and areas in fluid-phase oriented lipid membranes using wide angle X-ray scattering.," *Biophys. J.*, vol. 95, no. 2, pp. 669–681, 2008.

[155] M. Barrett, S. Zheng, L. Toppozini, R. J. Alsop, H. Dies, A. Wang, N. Jago, M. Moore, and M. C. Rheinstädter, "Solubility of cholesterol in lipid membranes and the formation of immiscible cholesterol plaques at high cholesterol concentrations," *Soft Matter*, vol. 9, no. 39, p. 9342, 2013.

[156] F. J.-M. de Meyer, A. Benjamini, J. M. Rodgers, Y. Misteli, and B. Smit, "Molecular simulation of the DMPC-cholesterol phase diagram.," *J. Phys. Chem. B*, vol. 114, pp. 10451–61, Aug. 2010.

[157] R. Alsop, C. Armstrong, and A. Maqbool, "Cholesterol expels ibuprofen from the hydrophobic membrane core and stabilizes lamellar phases in lipid membranes containing ibuprofen," *Soft Matter*, vol. 11, no. 24, pp. 4756 – 4767, 2015.

[158] O. Crescenzi, S. Tomaselli, R. Guerrini, S. Salvadori, A. M. D'Ursi, P. A. Temussi, and D. Picone, "Solution structure of the Alzheimer amyloid β-peptide (1-42) in an apolar microenvironment," *Eur. J. Biochem.*, vol. 269, pp. 5642–5648, Nov. 2002.

[159] H. W. Huang, "Action of Antimicrobial Pepties: Two State Model," *Biochemistry*, vol. 39, no. 29, pp. 25–30, 2000.

[160] D. M. Engelman, Y. Chen, C.-N. Chin, a. R. Curran, A. M. Dixon, A. D. Dupuy, A. S. Lee, U. Lehnert, E. E. Matthews, Y. K. Reshetnyak, A. Senes, and J.-L. Popot, "Membrane protein folding: beyond the two stage model.," *FEBS Lett.*, vol. 555, no. 1, pp. 122–125, 2003.

[161] M. Heyden, J. A. Freites, M. B. Ulmschneider, S. H. White, and D. J. Tobias, "Assembly and stability of α-helical membrane proteins," *Soft Matter*, vol. 8, no. 30, p. 7742, 2012.

[162] J. P. Ulmschneider, J. C. Smith, S. H. White, and M. B. Ulmschneider, "In silico partitioning and transmembrane insertion of hydrophobic peptides under equilibrium conditions," *J. Am. Chem. Soc.*, vol. 133, no. 39, pp. 15487–15495, 2011.

[163] K. Simons and E. Ikonen, "Functional rafts in cell membranes," *Nature*, vol. 387, pp. 569–572, 1997.

[164] D. M. Engelman, "Membranes are more mosaic than fluid," *Nature*, vol. 438, no. 7068, pp. 578–580, 2005.

[165] C. Eggeling, C. Ringemann, R. Medda, G. Schwarzmann, K. Sandhoff, S. Polyakova, V. N. Belov, B. Hein, C. von Middendorff, A. Schönle, and S. W. Hell, "Direct observation of the nanoscale dynamics of membrane lipids in a living cell.," *Nature*, vol. 457, no. 7233, pp. 1159–62, 2009.

[166] D. Lingwood and K. Simons, "Lipid rafts as a membrane-organizing principle.," *Science*, vol. 327, no. 5961, pp. 46–50, 2010.

[167] S. Seghezza, A. Diaspro, C. Canale, and S. Dante, "Cholesterol Drives Aβ (1-42) Interaction with Lipid Rafts in Model Membranes," *Langmuir*, vol. 30, 2014.

[168] C. Haass, C. Kaether, G. Thinakaran, and S. Sisodia, "Trafficking and proteolytic processing of APP," *Cold Spring Harb. Perspect. Med.*, vol. 2, no. 5, pp. 1–26, 2012.

[169] F. Olsson, S. Schmidt, V. Althoff, L. M. Munter, S. Jin, S. Rosqvist, U. Lendahl, G. Multhaup, and J. Lundkvist, "Characterization of intermediate steps in amyloid beta (Aβ) production under near-native conditions," *J. Biol. Chem.*, vol. 289, no. 3, pp. 1540–1550, 2014.

[170] K. Akabori and J. F. Nagle, "Structure of the DMPC lipid bilayer ripple phase," *Soft Matter*, vol. 11, no. 5, pp. 918–926, 2015.

[171] S. Aeffner, T. Reusch, B. Weinhausen, and T. Salditt, "Membrane fusion intermediates and the effect of cholesterol: an in-house X-ray scattering study.," *Eur. Phys. J. E. Soft Matter*, vol. 30, pp. 205–14, Oct. 2009.

[172] B. Kent, T. Hunt, T. a. Darwish, T. Hauß, C. J. Garvey, and G. Bryant, "Localization of trehalose in partially hydrated DOPC bilayers: insights into cryoprotective mechanisms.," *J. R. Soc. Interface*, vol. 11, no. 95, p. 20140069, 2014.

[173] Y. Ma, S. K. Ghosh, S. Bera, Z. Jiang, S. Tristram-nagle, L. B. Lurio, and S. K. Sinha, "Accurate calibration and control of relative humidity close to 100% by X-raying a DOPC multiplayer," *Phys. Chem. Chem. Phys.*, vol. 17, pp. 3570–3576, 2015.

[174] M. A. Kiselev, N. Y. Ryabova, A. M. Balagurov, S. Dante, T. Hauss, J. Zbytovska, S. Wartewig, and R. H. H. Neubert, "New insights into the structure and hydration of a stratum corneum lipid model membrane by neutron diffraction.," *Eur. Biophys. J.*, vol. 34, no. 8, pp. 1030–40, 2005.

[175] T. A. Harroun, K. Balai-Mood, T. Hauß, T. Otomo, and J. P. Bradshaw, "Neutron diffraction with an excess-water cell.," *J. Biol. Phys.*, vol. 31, no. 2, pp. 207–218, 2005.

[176] N. Y. Ryabova, M. A. Kiselev, S. Dante, T. Hauss, and A. M. Balagurov, "Investigation of stratum corneum lipid model membranes with free fatty acid composition by neutron diffraction.," *Eur. Biophys. J.*, vol. 39, no. 8, pp. 1167–1176, 2010.

[177] N. Y. Ryabova, S. G. Sheverev, and T. Hauß, "Neutron diffraction studies of oral stratum corneum model lipid membranes.," *Eur. Biophys. J.*, vol. 42, no. 8, pp. 621–9, 2013.

[178] H. Palsdottir and C. Hunte, "Lipids in membrane protein structures," *Biochim. Biophys. Acta - Biomembr.*, vol. 1666, no. 1-2, pp. 2–18, 2004.

[179] T. A. Harroun, H. Fritzsche, M. J. Watson, K. G. Yager, O. M. Tanchak, C. J. Barrett, and J. Katsaras, "Variable temperature, relative humidity (0%-100%), and liquid neutron reflectometry sample cell suitable for polymeric and biomimetic materials," *Rev. Sci. Instrum.*, vol. 76, no. 6, p. 065101, 2005.

[180] F. E. M. O'Brien, "The Control of Humidity by Saturated Salt Solutions," *J. Sci. Instrum.*, vol. 25, no. 3, pp. 73–, 1948.

[181] A. Wexler and S. Hasegawa, "Relative humidity-temperature relationships of some saturated salt solutions in the temperature range 0C to 50C," *J. Res. Natl. Bur. Stand. (1934).*, vol. 53, no. 1, pp. 19–26, 1954.

[182] L. Greenspan, "Humidity fixed points of binary saturated aqueous solutions," *J. Res. Natl. Bur. Stand. Sect. A Phys. Chem.*, vol. 81A, no. 1, p. 89, 1977.

[183] Omega, "Equilibrium Relative Humidity Saturated Salt Solutions," tech. rep., Omega Measurement and Control, 2015.

[184] A. Radulescu, N. Szekly, and M.-S. Appavou, "KWS-2," 2015.

[185] E. Schneck, F. Rehfeldt, R. Oliveira, C. Gege, B. Demé, and M. Tanaka, "Modulation of intermembrane interaction and bending rigidity of biomembrane models via carbohydrates investigated by specular and off-specular neutron scattering," *Phys. Rev. E*, vol. 78, pp. 1–9, Dec. 2008.

[186] C. Antoine, "Tensions des vapeurs; nouvelle relation entre les tensions et les températures," *Comptes Rendus des Séances l'Académie des Sci.*, vol. 107, pp. 681–684, 1888.

[187] A. Bridgeman and E. Aldrich, "Vapor pressure tables for water.," *J. Heat Transfer*, vol. 86, no. 2, pp. 279–286, 1964.

[188] D. S. S. Corp., "SolidWorks," 1995.

[189] "COMSOL Multiphysics 4.2," 2011.

[190] E. Edge, "Thermal Properties of Metals, Conductivity, Thermal Expansion, Specific Heat," 2015.

[191] C. A. Harper, ed., *Modern Plastics Handbook*. McGraw-Hill, 1 ed., 1999.

[192] C. Elliott, V. Vijayakumar, W. Zink, and R. Hansen, "National Instruments LabVIEW: A Programming Environment for Laboratory Automation and Measurement," *JALA - J. Assoc. Lab. Autom.*, vol. 12, no. 1, pp. 17–24, 2007.

[193] N. Grimm, "BerILL Labview Interface," 2014.

[194] LakeShore Cryotronics, "Model 350 Cryogenic Temperature Controller."

[195] Julabo, "Presto A30 Product DataSheet," tech. rep., Julabo, 2012.

List of Figures

List of Tables

Acknowledgements

I thank my advisor Prof. Matthias Ballauff for his advice and support, especially with regards to the dynamical measurements and presenting our results in an accessible way.

I thank the instrument scientists and technical staff of the various institutes who have been very supportive during the experiments and data analysis, including Tilo Seydel, Jacques Ollivier, Bruno Demé, Wiebke Lohstroh and Robert Georgii.

I would like to thank all of the engineers, technicians and scientists involved in the humidity chamber project, including Carlos Teixeira, Julien Gonthier, Simon Baudoin, Adrian Perkins, Eric Bourgeat-Lami, Eddy Lelièvre-Berna, Nico Grimm and Jörg Dathe.

I would also like to thank Richard Alsop, Clare Armstrong, Laura Toppozini and Maikel Rheinstädter for the helpful discussions and for hosting me at McMaster University during the X-ray diffraction experiments.

I would like to thank Ben Kent, Marcus Trapp and Prof. Norbert Dencher for their helpful discussions regarding data treatment and interpretation.

I also thank my supervisors Klaus Kiefer, Dirk Wallacher and Thomas Hauß for sharing their experience, providing guidance and giving support throughout my PhD work.

Last but not least, I would like to thank my family and friends in Canada and Germany for their support and love during the last three years, especially Anna Mersov and my parents Albert and MaryAnn Barrett.

Selbstständigkeitserklärung

Ich erkläre, dass ich die vorliegende Arbeit selbstständig und nur unter Verwendung der angegebenen Literatur und Hilfsmittel angefertigt habe.

Berlin, den 18.11.2015 Matthew Barrett